(NASA-CR-176231) A FUNDAMENTAL STUDY OF THE STICKING OF INSECT RESIDUES TO AIRCRAFT WINGS Annual Technical Report (Virginia Polytechnic Inst. and State Univ.) 191 p HC A09/MF A01 CSCL 01C G3/05

N86-10033

Unclas 15536

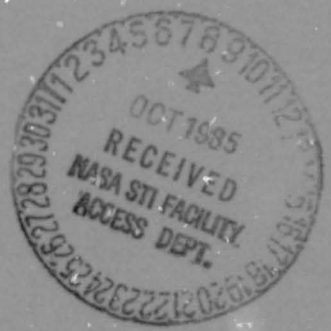

Virginia Polytechnic Institute and State University

Blacksburg, Virginia 24061

ANNUAL TECHNICAL REPORT

A FUNDAMENTAL STUDY OF THE STICKING OF INSECT RESIDUES TO AIRCRAFT WINGS

BY

N. S. Eiss, jr., J. P. Wightman,

D. R. Gilliam and E. J. Siochi

PREPARED FOR

NATIONAL AERONAUTICS AND SPACE ADMINISTRATION

NASA-LANGLEY RESEARCH CENTER

SUBSONIC-TRANSONIC AERODYNAMICS DIVISION

HAMPTON, VA 23665

D. M. Somers
W. D. Harvey

GRANT # NAG-1-300

FROM

CHEMISTRY DEPARTMENT AND MECHANICAL ENGINEERING DEPARTMENT

VIRGINIA POLYTECHNIC INSTITUTE AND STATE UNIVERSITY

BLACKSBURG, VA 24061

APRIL 1985

ABSTRACT

A FUNDAMENTAL STUDY OF THE STICKING OF INSECT RESIDUES TO AIRCRAFT WINGS

The aircraft industry has long been concerned with the increase of drag on airplanes due to fouling of the wings by insects. The present research studied the effects of surface energy and surface roughness on the phenomenon of insect sticking. Aluminum plates of different roughnesses were coated with thin films of polymers with varying surface energies. The coated plates were attached to a custon jig and mounted on top of an automobile for insect collection. Contact angle measurements, x-ray photoelectron spectroscopy and specular reflectance infrared spectroscopy were used to characterize the surfaces before and after the insect impact experiments. Scanning electron microscopy showed the topography of insect residues on the exposed plates. Moments were calculated in order to find a correlation between the parameters studied and the amount of bugs collected on the plates. An effect of surface energy on the sticking of insect residues was demonstrated.

TABLE OF CONTENTS

ABSTRACT ii

Chapter

page

I. INTRODUCTION 1

II. LITERATURE REVIEW 2

Insect Contamination 2
Surface Energy 4
Contact Angles 8
Spreading Pressure 10
Zisman 12
Models 16
Good and Girifalco 16
Fowkes 19
Rhee 23
Tamai, Makuuchi and Suzuki 23
Owens and Wendt 24
Kaelble 26
Wu 26
W. Good 29
Dann 30
X-ray Photoelectron Spectroscopy 33
Infrared Spectroscopy 43
Dispersive Infrared Spectroscopy 43
Fourier Transform Infrared Spectroscopy . . . 45
Specular Reflectance FT-IR 48

III. EXPERIMENTAL 52

Road Test 52
Phase I 52
Phase II 52
Roughness 52
Polymer Films 54
Sample Mount 57
Critical Surface Tension 60
Liquid Surface Tension Measurements 60
Contact Angle Measurements 67
Polar and Dispersion Components 69

Surface Characterization Before and After Insect Impact Experiments 70
Surface Energy 70
ESCA 70
Specular Reflection FT-IR 71
Scanning Electron Microscopy 71
Correlation of Surface Energy and Surface Roughness to Insect Contamination 71
Phase I 71
Bug Counts 71
Phase II 73
Bug Counts 73
Area Moments 73
Height Moments 75
Bug Identification 75

IV. RESULTS AND DISCUSSION 76

Surface Roughness 76
Surface Tension 84
Polar and Dispersion Components of Liquids . 88
Solid Surface Energy Determination 100
ESCA Take-off Angle Study 108
Surface Heterogeneity 110
The Meaning of Critical Surface Tension . . 111
Surface Roughness 123
Surface Characterization Before and After Insect Impact Experiments 125
Contact Angle Measurements 125
Phase I 125
Phase II 127
ESCA 129
Phase I 129
Phase II 131
Specular Reflectance FT-IR 134
Phase I 134
Phase II 134
Scanning Electron Microscopy 148
Correlation of Surface Energy and Surface Roughness to Insect Contamination . . . 148
Bug Counts 148
Phase I 148
Phase II 153
Area Moment Results 153
Height Moments Results 159
Bug Identity 163

V. SUMMARY 172

REFERENCES 174

LIST OF TABLES

Table

page

1. Phase I Trip Conditions 53
2. Blasting Conditions 55
3. Phase II Test Conditions 63
4. Comparison of Talysurf Results Before and After Polymer Coating 82
5. Surface Tensions of Aqueous Ethanol Solutions . . . 85
6. Surface Tensions of the Zisman Series 87
7. Contact Angles of Aqueous Ethanol Solutions on Paraffin 89
8. Contact Angles of Zisman Series on Paraffin 90
9. Polar and Dispersion Components of Aqueous Ethanol Solutions 91
10. Polar and Dispersion Components of the Zisman Series 92
11. Advancing Contact Angles of Aqueous Ethanol Solutions on Polymers 101
12. Advancing Contact Angles of Zisman Series on Polymers 102
13. Critical Surface Tensions 105
14. ESCA Take-off Angle Dependence Study Results . . . 109
15. Values of γ_s^d for Aqueous Ethanol Solutions Calculated using GGFY Equation 112
16. Values of γ_s^d for Zisman Series Calculated using GGFY Equation 113
17. Average Values of γ_s^d for Polymers from the Aqueous Ethanol Solutions 115

18. Average Values of γ_s^d for Polymers from the the Zisman Series 116

19. Average Values of I_{si}^p for Polymers from the Ethanol Solutions 117

20. Average Values of I_{sl}^p for Polymers from the Zisman Series 118

21. Values of γ_s^d and γ_s^h from Owens and Wendt Method . 122

22. Water Contact Angles on Rough Samples 124

23. Phase I Water Contact Angles Before and After Insect Impact Experiments 126

24. Phase II Water Contact Angles Before and After Insect Impact Experiments 128

25. Phase I ESCA Elemental Ratios Before and After Insect Impact Experiments 130

26. Phase I ESCA Binding Energies Before and After Insect Impact Experiments 132

27. Phase II ESCA Elemental Ratios Before and After Insect Impact Experiments 133

28. Phase II ESCA Binding Energies Before and After Insect Impact Experiments 135

29. Phase I Nyebar FT-IR Spectra Peak Assignment . . . 137

30. Phase I Polysulfone FT-IR Spectra Peak Assignment 139

31. Phase II Nyebar FT-IR Spectra Peak Assignment . . 142

32. Teflon FT-IR Spectra Peak Assignment 146

33. PMMA FT-IR Spectra Peak Assignment 147

34. Phase I Bug Counts 152

35. Phase I Bug Densities 154

36. Phase II Bug Counts 155

37. Phase I Bug Identity 167

38. Phase II Bug Identity 169

LIST OF FIGURES

Figure

page

1. Schematic diagram of spreading wetting. 6
2. Schematic diagram of adhesion wetting. 7
3. Schematic diagram of contact angle. 9
4. Wettability spectrum. 15
5. Fowkes model of a liquid/liquid interface. 20
6. Energy level diagrams of shake-up and shake-off phenomena. 35
7. Energy level diagrams of core hole decay modes. . . 36
8. Schematic diagram of ESCA instrumentation. 38
9. Effect of take-off angle on electron escape depths. 41
10. Effect of kinetic energy on escape depth. 42
11. Optical arrangement of a dispersive ir spectrometer. 44
12. Optical arrangement of an FT-IR spectrometer. . . . 46
13. Specular reflectance attachment. 49
14. Structures of polymers used. 56
15. Casting technique 58
16. Configuration of sample mount 59
17. Sample mount set-up 61
18. Phase II test site 62
19. Capillary rise set-up 64
20. Modified Wilhelmy balance set-up 65
21. Rame Hart goniometer 68
22. Specular reflectance attachment 72

23. Stagnation line 74

24. Talysurf traces of four roughened aluminum substrates. 77

25. SEM photomicrographs of 0.2 μm R_a and 0.5 μm R_a substrates. 78

26. SEM photomicrographs of 0.9 μm R_a and 1.3 μm R_a substrates. 79

27. SEM photomicrographs of Polysulfone coated and uncoated 1.3 μm substrates. 80

28. SEM photomicrographs of teflon coated substrates. . 83

29. Comparison of surface tension values by capillary rise and Wilhelmy plate method. 86

30. Polar and dispersion components of aqueous ethanol solutions surface tensions. 94

31. Polar and dispersion components of Zisman series surface tensions. 95

32. Legin plot of contact angle of aqueous ethanol solutions on paraffin. 97

33. Plot of contact angles of aqueous ethanol solutions on paraffin for this study. 98

34. Plot of surface tension polar component versus alcohol concentration. 99

35. Zisman plot of aqueous ethanol solutions. 103

36. Zisman plot of Zisman series. 104

37. (a) Nyebar and (b) PMMA molecular models. 107

38. Phase I Nyebar FT-IR spectra before and after road exposure. 136

39. Phase I polysulfone FT-IR spectra before and after road exposure. 138

40. Phase II Nyebar FT-IR spectra before and after road exposure. 141

41. Phase II polysulfone FT-IR spectra before and after road exposure. 143

42. Phase II Teflon FT-IR spectra before and after road exposure. 144

43. Phase II PMMA FT-IR spectra before and after road exposure. 145

44. SEM photomicrographs of bug excrescence on Nyebar and PSF. 149

45. SEM photomicrographs of bug fluid adhesive. . . . 150

46. SEM photomicrographs of insect residues on rough surfaces. 151

47. Phase II bug count versus surface energy. 156

48. Phase II bug count versus surface roughness. . . . 157

49. Area moment display. 158

50. Area moments versus surface energy. 160

51. Area moments versus surface roughness. 161

52. Height moment versus surface energy. 162

53. Height moment versus surface roughness. 164

54. Height moment versus contact angle. 165

55. Bug count versus mount position. 166

56. Examples of insects collected in insect impact experiments. 171

Chapter I

INTRODUCTION

Over the years, the aircraft industry has been involved in programs designed to increase fuel efficiency. One way of achieving this is by means of better wing design to reduce drag. A popular method that is in experimental use is called laminar flow control. It has been found that the efficiency of laminar flow control is diminished by insect fouling on the wings' leading edges. Although several methods have been used to solve the problem, there has been no systematic study of the effect of surface energy and surface roughness on the adhesion of insect residues to aircraft wings. The objective of this study was therefore to investigate the effect of both surface energy and surface roughness on insect fouling on polymer coated metal substrates.

Chapter II

LITERATURE REVIEW

2.1 INSECT CONTAMINATION

Interest in efficient aircraft design has always been high since fuel efficiency is a goal of commercial airlines. The key factor in attaining this goal is a wing design that will reduce drag (1). The method that has generated considerable interest is laminar flow control. Here drag reduction is achieved by extending the region of laminar flow through a suction mechanism at the leading edge of the aircraft wing (1-3). To achieve suction, the leading edge is perforated with millions of holes measuring 65 μm in diameter by means of an electron beam (4,5). Although laminar flow control is a technology which was developed in the thirties, interest in it was not revived until the seventies when the stringent material criteria could be attained with the advent of smooth composites and milled aluminum (4,6). Although construction of such a wing is more expensive by about $1.9 million than that of a turbulent flow one, the fuel savings can be up to $4 million per aircraft after the first six months (4).

A serious problem that has to be solved for maximum efficiency is the prevention of the build-up of insect

residues on the leading edge (7). It was found that about 55% of these residues were collected during the ground run and the rest of the residues on climbout and landing (8). The insect residues result in a surface roughness which is enough to disrupt laminar flow thus causing drag. This is most critical along the leading edge where heights between 40 and 230 μm have been documented as causing problems (9-11).

Several methods have been used in an attempt to solve the problem. In one method, the wing was covered with paper which was jettisoned after high altitude was reached. This method worked but was inconvenient (12). Liquid discharges to wash off residues have also been tried without much success (3,4,8). Superslick teflon films, as well as hydrophobic films were also tested unsuccessfully (11). A promising method is the use of elastic films that can absorb the kinetic energy of the impact. This elasticity allows the insect to bounce off (6). The technique needs to be pursued further. The most successful method thus far is the use of a continuous water spray. However, the effect in plane performance due to the added weight of the spray system has not yet been evaluated (12).

Insect collection experiments showed that the most numerous population at low altitude belonged to the order

Diptera. These insects were most abundant in May, June and September. Maximum collection was obtained when the humidity was below 59%, wind velocity was between 6-12 mph and the temperature was above 64° F (13). Theories have also been developed to predict the effects of insect contamination on drag(8, 14).

2.2 SURFACE ENERGY

Eliminating the fouling of aircraft wings by insect residues is essentially a problem of adhesion prevention. An understanding of the sticking process is thus required.

Adhesion can be studied in terms of wettability. Two types of wetting that are relevant in this study are spreading wetting and adhesion wetting. In spreading wetting, a liquid in contact with a solid spreads, resulting in an increase of the solid/liquid and the liquid/gas interfacial areas and a decrease in the gas/solid interfacial area (15). This is expressed by the equation for spreading coefficient:

$$S = \gamma_{sv} - \gamma_{lv} - \gamma_{sl} = -\Delta G_s/A \qquad [2\text{-}1]$$

where S is the spreading coefficient, γ_{sv} is the surface energy of the solid in equilibrium with the liquid vapor, γ_{lv} is the liquid surface tension, γ_{sl} is the solid/liquid interfacial tension, ΔG_s is the change in surface free

energy on wetting area A. When S is greater than or equal to zero or $\gamma_{lv} < \gamma_{sv} - \gamma_{sl}$, then spontaneous spreading occurs (16). If S < 0, the liquid forms a lens on the solid surface. Its shape is determined by a minimization of the surface free energy i.e. the term $\gamma_{sv}A_{sv} + \gamma_{sl}A_{sl} + \gamma_{lv}A_{lv}$ where A refers to interfacial area, is at a minimum. The situation is depicted in Figure 1 (15). The differential change in free energy due to spreading (17) is given by

$$dG = \gamma_{sl}dA + \gamma_{lv}dA\cos\theta - \gamma_{sv}dA \qquad [2\text{-}2]$$

At equilibrium, when dG/dA = 0,

$$\gamma_{sl} + \gamma_{lv}\cos\theta - \gamma_{sv} = 0 \qquad [2\text{-}3]$$

Adhesion wetting occurs when a liquid comes into contact with a solid, forming a solid/liquid interface which results from the loss of solid and liquid areas. This is shown in Figure 2 (18) and can be described by the equation:

$$\Delta G_{sl} = \gamma_{sl} - \gamma_{sv} - \gamma_{lv} = -W_a \qquad [2\text{-}4]$$

where W_a, the work of adhesion, gives a measure of the free energy of interaction between the liquid and the solid. When there is no interaction, then $W_a = 0$ and

$$\gamma_{sl} = \gamma_{lv} + \gamma_{sv} \qquad [2\text{-}5]$$

When there is interaction, then W_a is given by equation 2-4. The term W_a is thus the work required to separate the liquid from the solid, which is equal to the reversible change in free energy of the system (19). In cases where the two phases are the same, $\gamma_{sl} = 0$ and

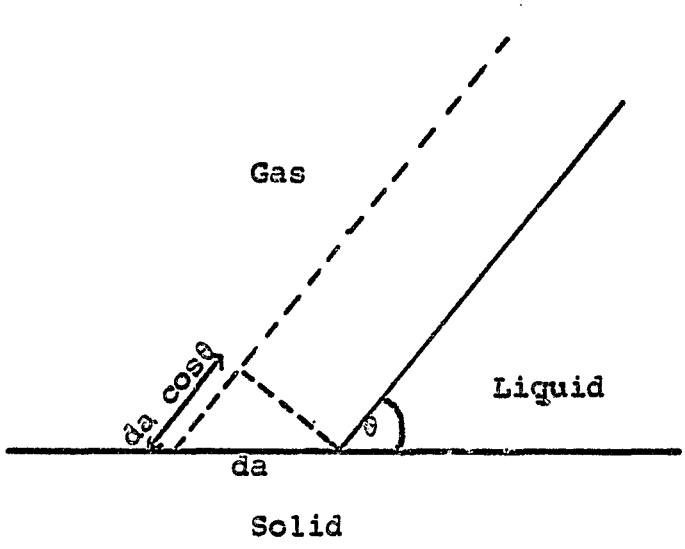

Figure 1: Schematic diagram of spreading wetting.

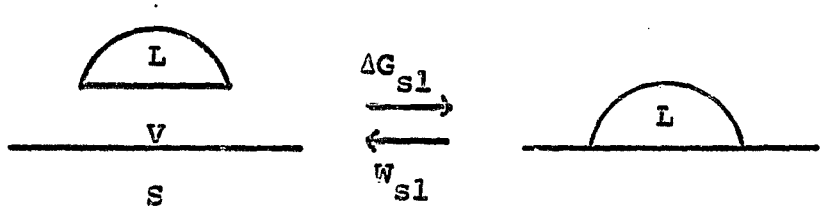

Figure 2: Schematic diagram of adhesion wetting.

$$W_a = 2\gamma_{lv} = W_c \qquad [2\text{-}6]$$

where W_c is the work of cohesion and is a measure of the intermolecular forces holding the phases together (20).

2.2.1 Contact Angles

The wettability of solids can be determined conveniently by measuring the contact angles of various liquids. The contact angle (θ) is defined as the tangent line of contact between the solid and the liquid as measured through the liquid. This is shown in Figure 3 (21).

In his original paper, Young (22) stated that the contact angle results from a balance of the forces acting on the liquid. P_l is the liquid adhesive force, P_s is the cohesion force of the solid and P_{sl} is the solid/liquid interaction contribution. In thermodynamic terms, these are the corresponding surface tensions. The equation which describes the equilibrium contact angle on the solid is said to be given by Dupre (23) and is called the Young-Dupre equation:

$$\gamma_{sv} - \gamma_{sl} = \gamma_{lv}\cos\theta \qquad [2\text{-}7]$$

The force exerted by the liquid is in the direction of the surface plane. The component of the liquid surface tension which is normal to the surface does not contribute to spreading and thus does not appear in the equation (20).

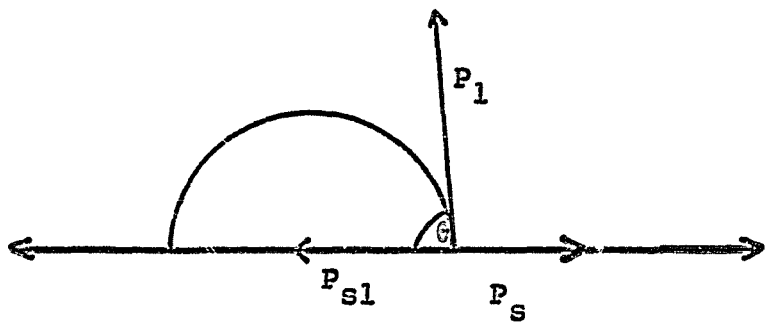

Figure 3: Schematic diagram of contact angle.

The expression is a result of the minimization of the free energy in the solid/liquid system (24), implying that the determining factor for the value of $\gamma_{lv}\cos\theta$ is the net reversible work of replacing the film covered surface with the solid/liquid interface (25). Combining equations [2-4] and [2-7] yields an expression relating W_a and θ.

$$W_a = \gamma_{lv}(1 + \cos\theta) \qquad [2\text{-}8]$$

Aside from providing an indication of the work of adhesion, the contact angle also gives an idea of the cohesion of the liquid to itself. When adhesion is less than cohesion, a finite contact angle is observed. The smaller the contact angle, the greater is the adhesion between the solid and the liquid (26). If the liquid spreads on the solid so that $\theta = 0$ and $\cos\theta = 1$, then equation [2-6] results, implying that the interaction between the solid and the liquid is greater than that between the liquid molecules.

2.2.2 Spreading Pressure

When a liquid drop is in contact with a solid surface, the base solid will adsorb liquid vapor until the effective vapor pressure of the adsorbed film is equal to that of the vapor and the film covered solid (23). The contact angle remains constant only if equilibrium has been established between the vapor and the solid (27). At this point, the

surface energy of the bare solid (γ_s), would have been reduced by the vapor adsorption so that

$$\gamma_{sv} = \gamma_s - \pi_{sv} \qquad [2\text{-}9]$$

and as Harkins suggested, equation [2-8] should be corrected to read

$$W_a = \gamma_{lv}(1 + \cos\theta) + \pi_{sv} \qquad [2\text{-}10]$$

where π_{sv} is the spreading pressure and is the amount by which the liquid vapor reduces the bare solid surface energy.

The spreading pressure can be determined by using the Gibbs adsorption isotherm

$$\pi_{sv} = RT\int_0^{P^0} \Gamma d\ln P \qquad [2\text{-}11]$$

where P^0 is the saturated vapor pressure of the liquid and Γ is the amount of vapor adsorbed. Values of spreading pressures per unit area of solid are hard to come by since the values are usually obtained by adsorption of gas molecules onto powdered samples whose characteristics may differ widely from the smooth solids used in contact angle measurements (28). Ellipsometry has been used to measure spreading pressure of liquids on smooth solids since the thickness of the liquid film may be related to π (29). A statistical mechanics treatment of π can also be used by considering the energy and entropy involved in the transfer of a molecule from the bulk to the adsorbed monolayer:

$$\pi = \frac{kT}{\sigma}\left[\frac{x_a}{1 - x_a}\right] \qquad [2\text{-}12]$$

where σ is the surface area of a molecule in a close packed monolayer, k is Boltzmann's constant, T is temperature and x_a is the mole fraction of occupied surface sites (30).

2.2.3 Zisman

Since contact angles have been linked to surface wettability by Young, a number of researchers have used this variable to characterize surfaces. One of the major contributors to this area was Zisman, whose work has provided a broad database of critical surface tension values that has been widely cited over the past two decades.

In studies of solid surfaces, Zisman and co-workers determined contact angles of various series of liquids with decreasing surface tensions (19,31,32). One series commonly known as the Zisman series consists of water, glycerol, formamide, methylene iodide and 1-bromonaphthalene. The varied properties (molecular volume, effective cross-sectional area, dipole moments, polarizability and surface tension) of these liquids allow the determination of solid surface energies, as well as a study of the solid surface composition and structure (33). Zisman plotted contact angle results as $\cos\theta$ versus γ_{lv}. It was found that the points lie in a line described by the equation:

$$\cos\theta = a - b\gamma_{lv} \qquad [2\text{-}13]$$

Even for the non-homologous liquid series above, the data often lie in a narrow rectilinear band about the line. Upon extrapolation to $\cos\theta = 1$, one obtains γ_c, the critical surface tension, which is the surface tension of the liquid that just wets the solid. Since only liquids with γ_{lv} lower than γ_c can wet the solid, γ_c is an indication of the solid's wettability (33,34).

There are exceptions to straight line Zisman plots. In some cases, particularly in liquids with γ_{lv} greater than 50 dynes/cm, the graphs exhibit a slight curvature. This was suggested as being the result of weak hydrogen bonding between the liquid and the solid molecules and occurs often with higher surface tension liquids having a greater tendency for association with the solid (32).

Although pure liquids are generally used for γ_c determinations, aqueous alcohol solutions have also been utilized. There is however a controversy associated with this since the values of γ_c obtained are usually lower than those obtained using pure liquids and differ according to what alcohol has been used. These results have been explained as being due to preferential adsorption of alcohol molecules on the solid/liquid and solid/vapor interfaces, thus disguising the true surface energy of the solid

substrate (35,36). Some evidence of a phase transition has also been cited as resulting from preferential adsorption at the interface (37).

By comparing γ_c values of a homologous or an analogous series of solids such as polyethylene and its chlorinated and fluorinated counterparts, Zisman derived a relationship between γ_c and surface constitution. It was concluded that surface wettability is determined by the nature and packing of surface atoms. The bigger the surface groups, the fewer the number of interaction sites per unit area exists and the lower the critical surface tension (19,20,33). A summary of the effect of surface constitution on critical surface tension is given in the wettability spectrum (31) shown in Figure 4.

The theory of closest packing advanced by Zisman was contested by Hoernsmeyer (38), who claims that the higher concentration of interaction sites should result in greater interaction and a smaller contact angle. He proposed that the solid/liquid potential energy of interaction per unit area accounts for the observed contact angle behavior of solid/liquid systems. Thus the major difference in wettability of fluorocarbons and hydrocarbons was attributed by Hoernsmeyer to packing density and not to intermolecular interaction energy.

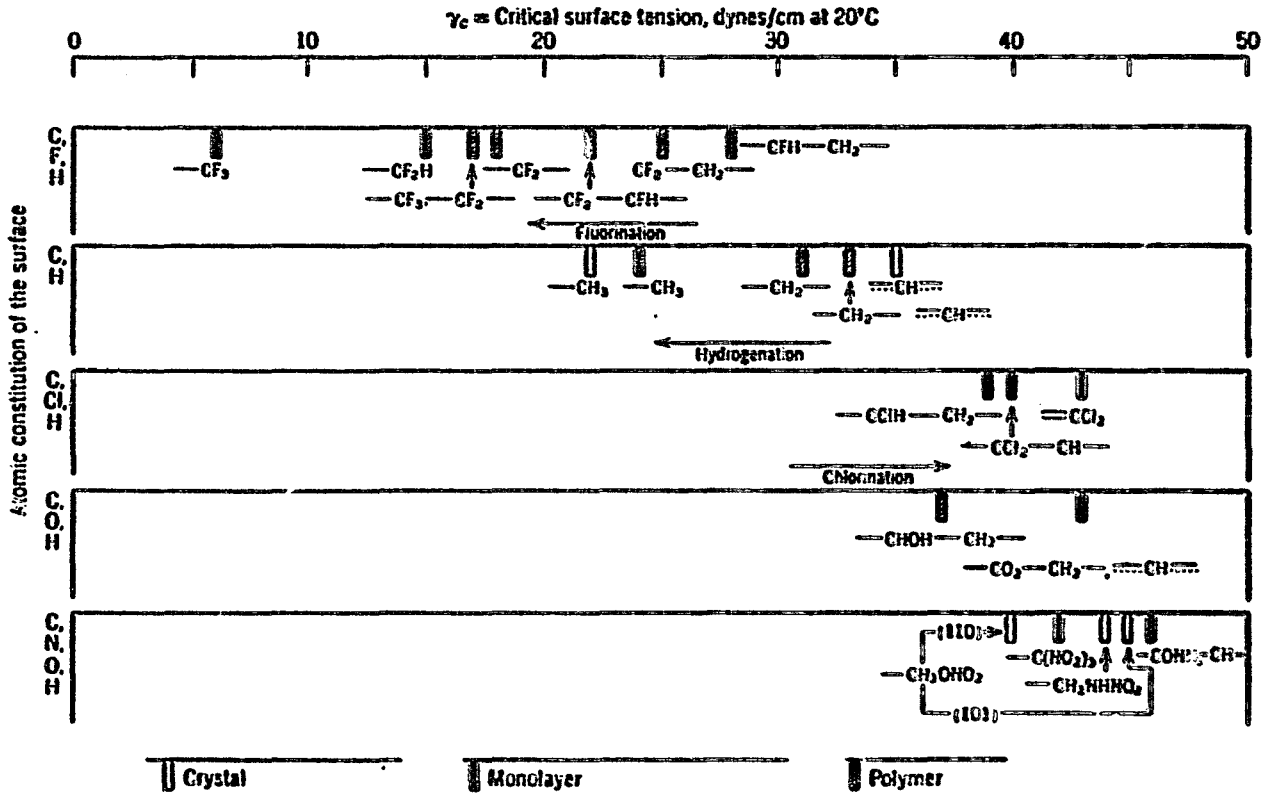

Figure 4: Wettability spectrum

ORIGINAL PAGE IS
OF POOR QUALITY

2.2.4 Models

In the Young - Dupre equation, the right side consists of easily measurable terms. Several theories have evolved in an effort to come up with a means of determining the difference, $\gamma_{sv} - \gamma_{sl}$, independently. One of the most popular models is that proposed by Good and Girifalco.

2.2.4.1 Good and Girifalco

Good and Girifalco (39,40) assumed equal sized molecules and that only nearest neighbors can interact. The free energy required to bring a bulk liquid molecule to the surface is given by:

$$2\gamma_1 V^{2/3} = (n_1 + 2n_2)\varepsilon_{11} - (n_1 + n_2)\varepsilon_{11} = n_2\varepsilon_{11} \qquad [2\text{-}14]$$

where

1. V is the molecular volume.
2. $V^{2/3}$ gives the molecular area.
3. n_1 is the number of molecules in the plane of a given molecule.
4. n_2 is the number of molecules in planes above and below as nearest neighbors.
5. ε_{11} is the surface free energy of each molecule in the liquid.

The corresponding equation for the solid is given by:

$$2\gamma_s V^{2/3} = n_2 \epsilon_{ss} \qquad [2\text{-}15]$$

These equations yield an expression for W_a:

$$2W_a V^{2/3} = (n_1 + n_2)\epsilon^{\circ}_{11} + n_2\epsilon^{\circ}_{s1} + (n_1 + n_2)\epsilon^{\circ}_{ss} + n_2\epsilon^{\circ}_{s1} - (n_1 + n_2)\epsilon^{\circ}_{11} - (n_1 + n_2)\epsilon^{\circ}_{ss} = 2n_2\epsilon^{\circ}_{s1} \qquad [2\text{-}16]$$

If

$$\epsilon_{s1} = \sqrt{\epsilon_{ss}\epsilon_{11}} \qquad [2\text{-}17]$$

as is allowed for regular interfaces where the Lennard-Jones potential is obeyed by the pairs of molecules (40), is combined with equations [2-13] and [2-14], then

$$\gamma_{s1} = \gamma_s + \gamma_1 - W_{s1} = \gamma_s + \gamma_1 - 2\Phi_{12}\sqrt{\gamma_s\gamma_1} \qquad [2\text{-}18]$$

where

$$\Phi_{12} = \frac{(V_1V_2)^{1/3}}{(V_1^{1/3} + V_2^{1/3})^2} \qquad [2\text{-}19]$$

Φ_{12} corrects for the disparities in molecular volume of the solid and the liquid and is characteristic of a particular system. It is a function of polarizability, dipole moment, and ionization potential. When polymers are involved, only the properties of the dominant groups are considered (34,39,41). For example, CF_2 group characteristics are used for teflon and CO_2C properties are utilized for esters. If the intermolecular forces of two molecules are very different, $\Phi_{12} << 1$. This interaction parameter will subsequently be referred to as Φ.

If equation [2-18] is combined with the Young - Dupre equation and π is neglected, an equation for γ_s is obtained (41):

$$\gamma_s = \frac{\gamma_1(1 + \cos\theta)^2}{4\Phi_{12}^2} \qquad [2\text{-}20]$$

Good relates the theory to Zisman's empirical observations by saying that the alternative expression of Zisman,

$$\cos\theta = b(\gamma_{lv} - \gamma_c) + 1 \qquad [2\text{-}21]$$

corresponds to the first two terms in a Taylor series expansion of

$$\cos\theta \approx -1 + 2\Phi\sqrt{\gamma_s}/\gamma_{lv} \qquad [2\text{-}22a]$$

$$= 1 - \frac{\gamma_{lv} - \Phi^2\gamma_s}{\Phi^2\gamma_s} + \frac{3\left[\gamma_{lv} - \Phi^2\gamma_s\right]}{4\quad\Phi^2\gamma_s} \qquad [2\text{-}22b]$$

If Φ is a constant as is the case for a homologous liquid series, when $\theta = 0$ and $\gamma_{lv}=\gamma_1$, then

$$\Phi_c^2\gamma_s = \gamma_c \qquad [2\text{-}23]$$

where Φ_c is the limiting value of Φ. If equation [2-23] is substituted into equation [2-22b], then the series converges for $\gamma_{lv} < 2\gamma_c$, so that one can plot $\gamma_{lv}(1 + \cos\theta)^2/4\Phi^2$ or $\gamma_{lv}(1 + \cos\theta)^2/4$ versus γ_{lv} to obtain a horizontal straight line whose slope is the negative inverse of the critical surface tension (41).

The theory has several limitations. The solid surface energy obtained is real only if the following conditions hold (34):

1. The liquid used does not attack the surface.
2. The contact angle has to be the equilibrium one.
3. The spreading pressure must be negligible.
4. Orientation entropy errors are not important.
5. The potential functions are known.
6. Only nearest neighbor interactions exist.
7. Concentration gradient effects are negligible.
8. The solid is homogeneous.
9. There is no strong hydrogen bonding present.

2.2.4.2 Fowkes

Another model often used to determine γ_{sl} and γ_s is an extension of Fowkes' model for liquids which is shown in Figure 5. Fowkes' premise is that molecules at the surface do not have the same intermolecular distances as those in the bulk since forces acting on them are different. The forces acting on the surface molecules result in a surface tension. It is assumed that the predominant force across the interface is the dispersion force which is a result of the fluctuating dipoles from induced dipoles of nearest neighbors (42-45). The only significant interactions across

ORIGINAL PAGE IS
OF POOR QUALITY

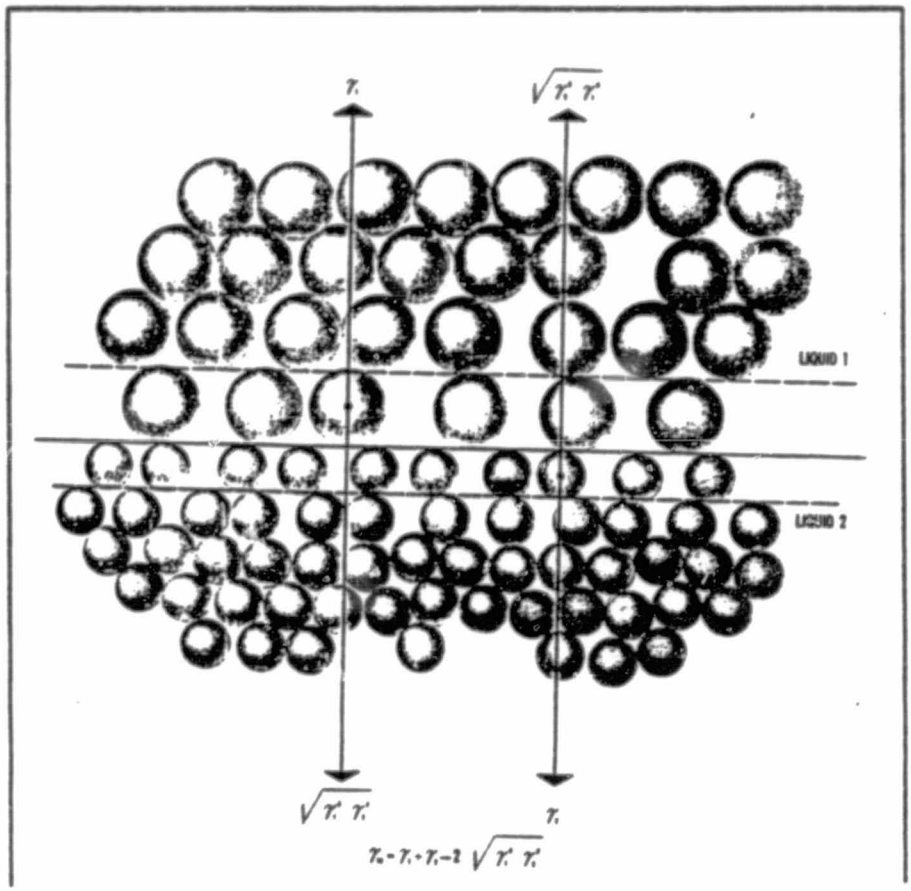

Figure 5: Fowkes model of a liquid/liquid interface.

interfaces are the ones that are similar. Since all materials have dispersion forces, this is the only one considered in

$$\gamma_{12} = \gamma_1 + \gamma_2 - 2\sqrt{\gamma_1^d \gamma_2^d} \qquad [2\text{-}24]$$

where

1. γ_{12} is the interfacial tension between the two liquids.
2. γ_1 is surface tension of liquid 1.
3. γ_2 is surface tension of liquid 2.
4. γ^d is dispersion component of the liquid surface tension.

More recently though, Fowkes has proposed that in addition to dispersion forces, acid - base interactions play a major role at interfaces (46). It was also shown that surface tensions are closely related to the potential energy of intermolecular interactions by deriving an interfacial tension equation from potential energy considerations (47). Furthermore, he postulated that aside from the dipole moment component, all other forces are additive since they can interact simultaneously (43,44). For instance, the surface tension of water can be broken down into the dispersion γ^d and hydrogen bonding γ^h components such that

$$\gamma_w = \gamma^d + \gamma^h \qquad [2\text{-}25]$$

If equation [2-25] is combined with the Young - Dupre

equation, and the spreading pressure is neglected, the following relationship results (43,44):

$$\cos\theta = 2\sqrt{\gamma_l^d \gamma_s^d}/\gamma_l - 1 \qquad [2\text{-}26]$$

This equation can be used to determine the dispersion component of the solid from contact angle measurements. Furthermore, if the solid surface energy is made up of other components as well, the sum of these components may also be determined (34,47,48).

A plot of $\cos\theta$ versus $\sqrt{\gamma_l^d}/\gamma_l$ would yield a straight line whose origin is at -1 and which has a slope equal to $2\sqrt{\gamma_s^d}$. Thus, the equation may be used to predict the contact angle of any other hydrocarbon whose surface tension is known (42). One can also plot $\cos\theta$ versus $1/\sqrt{\gamma_{lv}}$. The intersection at $\cos\theta = 1$ should be γ_s^d, which is analogous to Zisman's critical surface tension. A correlation between Fowkes' theory and Zisman's critical surface tension may be drawn if γ_c is actually γ_c^d (35,43).

Fowkes' model is basically an extension of the Good and Girifalco model except that it deals with more specific forces. Fowkes for example, does not include the Φ term, although this may be justified by the fact that for most molecules, the effective group radii do not vary significantly so that $\Phi \approx 1$ (44,47).

2.2.4.3 Rhee

A third model is derived by Rhee (49) from equation [2-20]. This equation combined with that of Young - Dupre yields an expression for γ_{sl}:
which indicates that γ_{sl} follows a parabolic behavior. If the parabolic minimum is assumed to be zero, then

$$b\gamma_{sv} - 1/4(b\gamma_c + 1)^2 = 0 \qquad [2\text{-}27]$$

and

$$\gamma_{sv} = \gamma_s - \pi = 1/4b(b\gamma_c + 1)^2 \qquad [2\text{-}28]$$

If the minimum occurs at $\cos\theta = 1$, then

$$\gamma_c = 1/b = \gamma_{sv} \qquad [2\text{-}29]$$

These results are consistent with Fowkes'.

All the theories discussed above assume that only dispersion interactions are present. Realistically however, the situation is more complex since true surfaces have components such as polar contributions which could be quite significant. In recognition of this, several theories on interfacial tension that include non-dispersion interactions have been proposed.

2.2.4.4 Tamai, Makuuchi and Suzuki

Tamai et al. extended Fowkes theory simply by adding a non-dispersion term so that:

$$\gamma_{12} = \gamma_1 + \gamma_2 - 2\sqrt{\gamma_1^d \gamma_2^d} - I_{12} \qquad [2\text{-}30]$$

where I_{12} is due to non-dispersion forces. By combining equation [2-30] with the Young - Dupre equation, a relationship between contact angles and interfacial forces is obtained (50):

$$\cos\theta = \frac{1 + 2\sqrt{\gamma_s^d \gamma_1^d} - \pi_s + I_{sl}^p}{\gamma_1 - \pi_1} \qquad [2\text{-}31]$$

If the spreading pressures are negligible, equation [2-31] can be rearranged to solve for I_{sl}^p:

$$I_{sl}^p = (\cos\theta + 1)\gamma_1 - 2\sqrt{\gamma_s^d \gamma_1^d} \qquad [2\text{-}32]$$

so that the non-polar contribution is merely the difference between the work of adhesion and the dispersion force interactions at the interface.

2.2.4.5 Owens and Wendt

Another popular extension of Fowkes' theory is that by Owens and Wendt (51). In this case, another term was added to equation [2-23] to include hydrogen bonding interactions

$$\gamma_{sl} = \gamma_{sv} + \gamma_{lv} - 2\sqrt{\gamma_s^d \gamma_l^d} - 2\sqrt{\gamma_s^h \gamma_l^h} \qquad [2\text{-}33]$$

which can be rewritten as

$$\cos\theta + 1 = 2\sqrt{\gamma_s^d \gamma_l^d}/\gamma_{lv} + 2\sqrt{\gamma_s^h \gamma_l^h}/\gamma_{lv} \qquad [2\text{-}34]$$

If the Young - Dupre equation can be written as

$$\gamma_{lv}\cos\theta = \gamma_c = \gamma_{sv} - \gamma_{sl} - \pi_e \qquad [2\text{-}35]$$

rearrangement of equation [2-34] and combination with [2-35] yields

$$\gamma_s - \gamma_c = (\sqrt{\gamma_s^d} - \sqrt{\gamma_l^d})^2 + (\sqrt{\gamma_s^h} - \sqrt{\gamma_l^h})^2 \qquad [2\text{-}36]$$

As a consequence, the theory implies that if a non-polar liquid is used so that the hydrogen bonding component of the liquid surface tension is zero, then the dispersion component of the liquid surface tension is equal to that of the solid which is equal to the critical surface tension. Zisman's γ_c is thus a measure of the dispersion component of the solid surface energy. The second case is when a polar liquid is used on a non-polar solid, $\gamma_l^h \neq 0$ but $\gamma_s^h \approx 0$. If these quantities were substituted into equation [2-36], one would note that polar liquids would yield critical surface tensions lower than the true solid surface energy. The last case is when a non-polar liquid is used on a polar solid, in which case $\gamma_l^h = 0$ but $\gamma_s^h \neq 0$. The same result is obtained as in the second case (51).

Application of the theory involves using contact angles of two different liquids on a solid, whereupon γ_s^d and γ_s^h can be determined by solving simultaneous equations.

2.2.4.6 Kaelble

A third theory was advanced by Kaelble (18,36). He showed that the interaction parameter of Good and Girifalco Φ, could be expressed as

$$\Phi = \sqrt{d_s d_l} + \sqrt{p_s p_l} \qquad [2\text{-}37]$$

where d is the proportion of the surface energy due to dispersion forces and p is that due to polar interactions. S refers to the solid and 1 to the liquid. Furthermore, Kaelble proposed that

$$d_s + p_s = 1 \qquad [2\text{-}38a]$$

$$d_l + p_l = 1 \qquad [2\text{-}38b]$$

If this were true, then if only dispersion forces exist, equation [2-23] results. Like Owens and Wendt's equation, determination of contact angles of two liquids on a solid allows access to polar and dispersion components by means of the following equations

$$\gamma_1 (1 + \cos\theta_1) = 2\sqrt{\gamma_1^d \gamma_s^d} + 2\sqrt{\gamma_1^p \gamma_s^p} \qquad [2\text{-}39a]$$

$$\gamma_2 (1 + \cos\theta_2) = 2\sqrt{\gamma_2^d \gamma_s^d} + 2\sqrt{\gamma_2^p \gamma_s^p} \qquad [2\text{-}39b]$$

Good cautions that if γ_s^p obtained in this manner is less than 5% of the total surface energy, then the surface is to be considered non-polar(41).

2.2.4.7 Wu

All the above theories invoke the geometric mean in the derivation of the interfacial tension. A strong proponent of the use of the harmonic mean is Wu (52,53), who claims that it is more accurate in cases where an organic liquid/polymer interface is being studied. Starting from a combination of the Young - Dupre and the Good - Girifalco equations [2-20] and defining the critical surface tension as

$$\gamma_c = \lim_{\theta \to 0} \gamma_l \qquad [2\text{-}40]$$

then

$$\gamma_c = \Phi^2\gamma_s - \pi_e + (\pi_e^2/4\Phi^2\gamma_s) + \ldots \qquad [2\text{-}41a]$$

which can be terminated to yield

$$\gamma_{c,\phi} = \Phi^2\gamma_s - \pi_e \qquad [2\text{-}41b]$$

where $\gamma_{c,\phi}$ is γ_c and stresses that γ_c is a function of the interaction parameter. To obtain a relationship with $\cos\theta$, equation [2-41b] is substituted into equation [2-20] to yield

$$\cos\theta = 2\sqrt{\gamma_{c,\phi}/\gamma_{lv}} - 1 \qquad [2\text{-}42]$$

This can be rearranged to give an expression of $\gamma_{c,\phi}$. It allows a determination of γ_c with just one liquid. A series of liquids will however yield a plot of $\gamma_{c,\phi}$ versus γ_{lv} with a maximum at $\phi = 1$ which indicates that the polarities of the two surfaces are the same. This $\gamma_{c,\phi max}$ is then equal to γ_s.

To demonstrate the difference between the geometric mean methods and that of the harmonic mean, Wu's approach will be shown here (53). Starting with

$$\gamma_{12} = \gamma_1 + \gamma_2 - W_{12} \qquad [2\text{-}43]$$

where W_{12} is made up of the polar and non-polar components. W_c, the work of cohesion, can also be broken down into its different components. W_a is then expressed in terms of W_c in a harmonic mean equation

$$W^d_{a12} = \frac{2W^d_{c1}W^d_{c2}}{W^d_{c1} + W^d_{c2}} = \frac{4\gamma^d_1\gamma^d_2}{\gamma^d_1 + \gamma^d_2} \qquad [2\text{-}44a]$$

The corresponding equation for the polar term is

$$W_{a12} = \frac{4\gamma^p_1\gamma^p_2}{\gamma^p_1 + \gamma^p_2} \qquad [2\text{-}44b]$$

Substitution into equation [2-43] yields:

$$\gamma_{12} = \gamma_1 + \gamma_2 - \frac{4\gamma^d_1\gamma^d_2}{\gamma^d_1 + \gamma^d_2} - \frac{4\gamma^p_1\gamma^p_2}{\gamma^p_1 + \gamma^p_2} \qquad [2\text{-}45]$$

A comparison of values obtained by the harmonic mean method and the geometric mean method with experimental values does show that for interfacial tensions between polymers, the harmonic mean method yields results closer to the measured interfacial tension (53).

2.2.4.8 W. Good

An attempt has been made by W. Good (48) to correlate an extended Fowkes' theory to Zisman's critical surface tension by using the following equation:

$$\cos\theta = \frac{2\sqrt{\gamma_1^d \gamma_s^d}}{\gamma_1} + \frac{\Gamma_p(\gamma_1^p, \gamma_s^p)}{\gamma_1} - 1 \qquad [2\text{-}46]$$

The basic assumptions are that the total surface tension is composed of the polar and dispersion contributions and that

$$\Gamma_p(\gamma_1^p, \gamma_s^p) = \Gamma_1(\gamma_1^p)\Gamma_s(\gamma_s^p) \qquad [2\text{-}47]$$

which insures that when the polar component of either or both the liquid and the solid is zero, then there is no polar interaction. Spreading pressure is also assumed to be negligible. When $\Gamma_s(\gamma_s^p) = 0$ but $\Gamma_1(\gamma_1^p) \neq 0$, equation [2-46] becomes

$$\cos\theta = 2\sqrt{\gamma_1^d \gamma_s}/\gamma_1 - 1 \qquad [2\text{-}48]$$

To relate this to γ_c, the boundary condition applied is that $\cos\theta = 1$ which yields

$$\gamma_c = \sqrt{\gamma_1^d \gamma_s} \qquad [2\text{-}49a]$$

$$\gamma_c/\gamma_s = \sqrt{\gamma_1^d/\gamma_s} \qquad [2\text{-}49b]$$

If $\gamma_1^p = 0$, then $\gamma_1 = \gamma_c = \gamma_1^d = \gamma_s$. If $\gamma_1^p = 0$, $\gamma_1 = \gamma_c = \gamma_1^p + \gamma_1^d$ or

$$\gamma_c = \sqrt{(\gamma_c - \gamma_1^p)\gamma_s} \qquad [2\text{-}50]$$

the solution of which is

$$\gamma_c = 1/2\gamma_s[1 + \sqrt{1 - 4\gamma_1^p/\gamma_s}] \qquad [2\text{-}51]$$

making it complex when $\gamma_1^p/\gamma_s > 1/4$, thus implying that regardless of what liquid is used, the lowest γ_c is equal to $1/2\gamma_s$ (48).

Treating the Good-Girifalco equation in the same manner, the following relationship is obtained

$$\gamma_c = \phi^2\gamma_s \qquad [2\text{-}52]$$

Through correspondence between equations [2-20] and [2-48], an expression for ϕ is obtained

$$\phi = \sqrt{\gamma_1^d/\gamma_1} \qquad [2\text{-}53]$$

Substitution of equation [2-52] into [2-49a] yields

$$\phi = \sqrt{\gamma_c/\gamma_s} \qquad [2\text{-}54]$$

2.2.4.9 Dann

In an effort to pull together all the above theories, Dann (54,55) took contact angle measurements of various liquid series on several polymers. The Good-Girifalco-Fowkes-Young equation was used in a predictive capacity to estimate the γ_c of a solid with one liquid series from that of another series. This was done by plotting $\sqrt{\gamma_1^d}/\gamma_1 = 1/\sqrt{\gamma_s^d}$ versus γ_c (54). The value of γ^p

was calculated by assuming that total surface tension is the sum of its components. It was also found that inspite of the fact that Good, Girifalco and Fowkes assumed only dispersion forces in their theories, the equations are actually valid for systems where the polar component of the liquid surface tension is less than or equal to 9 dynes per cm. Further it was shown that Zisman plots yielded curves instead of straight lines. If polar liquids were used to determine γ_c of non-polar solids, values of γ_c were lower than those obtained by using non-polar liquids. If both solid and liquid have polar components that interact, γ_c would be higher(54). Non-dispersion interactions can be detected in a plot of cosθ versus $\sqrt{\gamma_l^d}/\gamma_l$ for polar and non-polar liquids. If γ_s^d obtained by drawing a straight line through the origin and the experimental points are higher for polar liquids, then polar interactions are present. In extending the Tamai, Makuuchi, Suzuki theory, Dann found that I_p is related to the spreading coefficient such that if

$$S_{obs} = (\cos\theta - 1)\gamma_l \qquad [2\text{-}55]$$

and

$$S_{calc} = 2\sqrt{\gamma_l^d \gamma_s^d} - 2\gamma_l \qquad [2\text{-}56]$$

$$S_{obs} - S_{calc} = (\cos\theta - 1)\gamma_l - 2\sqrt{\gamma_l^d \gamma_s^d} + 2\gamma_l \qquad [2\text{-}57a]$$

or

$$S_{obs} - S_{calc} = (\cos\theta + 1)\gamma_l - 2\sqrt{\gamma_l^d \gamma_s^d} \qquad [2\text{-}57b]$$

which is equal to I_p so that

$$I_p = S_{obs} - S_{calc} \qquad [2\text{-}58]$$

I_p is thus dependent on γ_l^p and γ_s^p.

All the above theories assumed a homogeneous, smooth solid surface. Physically rough and chemically heterogeneous surfaces are more common. These surfaces add a complexity to the already complicated issue of contact angles. This area has been aptly treated by Johnson and Dettre (20,56,57) and Cox (58).

Adamson once questioned the thermodynamic status of the contact angle since he claimed that none of the proposed theories apply universally (25). This view could now be discounted by people who have derived the Young equation from basic thermodynamics (24,59,60).

Although the Good-Girifalco-Fowkes-Young equation is the most popular one in use, it is not realistic to assume that all systems are totally dominated by dispersion interactions. Theories that include polar components abound in the literature. However, there is still a need to understand the contributions of the non-dispersion components.

2.3 X-RAY PHOTOELECTRON SPECTROSCOPY

The polymer films used as coatings to minimize insect fouling interact with the environment through the polymer surface. This being so, an understanding of the role of the surface in the insect residue adhesion may be achieved through a knowledge of the nature of the film surfaces. The pertinent questions that need to be answered include (61):

1. What elements are present?
2. What are the concentrations of these elements?
3. In what forms do they exist on the polymer surface?
4. What are the percentages of the different forms?

X-ray photoelectron spectroscopy (XPS) or electron spectroscopy for chemical analysis (ESCA) is a powerful tool developed by Professor Kai Siegbahn, that is capable of providing answers to all of the questions posed above.

The ESCA experiment involves impinging the solid sample surface with an x-ray beam of known incident energy. The beam ionizes electrons within the solid whose binding energies are less than the incident x-ray energy. Electrons are in quantized levels, and thus have a kinetic energy distribution composed of discrete bands, that is a function of the shell from which electrons were ejected (62). The whole process may be described by the Einstein relation (63,64):

$$h\upsilon = E_b + E_k \qquad [2\text{-}59]$$

where $h\upsilon$ is the incident x-ray beam energy, E_b is the binding energy of the photoejected electron and E_k is the kinetic energy of the photoejected electron.

The removal of one photoelectron from the core level may result in the rearrangements of valence electrons as a response to the charge induced by the process. These events are shown schematically in Figure 6 (65). Shake-up accompanies photoionization when an electron is excited and moves from an occupied to an unoccupied energy level. On the other hand, the ionization of a valence electron is called a shake-off phenomenon. These processes may be observed in some ESCA experiments.

There are two other processes that occur to achieve relaxation in the system. These are shown in Figure 7. In x-ray fluorescence, the core hole is filled by an electron in an energy level of lower binding energy and the energy released is a photon in the x-ray frequency region. The alternative mode of decay for the hole is the Auger process where an electron of a lower binding energy fills the hole. The excess energy is dissipated by the ionization of an outer electron which has a kinetic energy of

$$E = \varepsilon_b - \varepsilon_a + \varepsilon_c \qquad [2\text{-}60]$$

where the subscripts indicate the energy levels. The result of this relaxation process is a doubly charged system.

Figure 6: Energy level diagrams of shake-up and shake-off phenomena.

ORIGINAL PAGE IS
OF POOR QUALITY

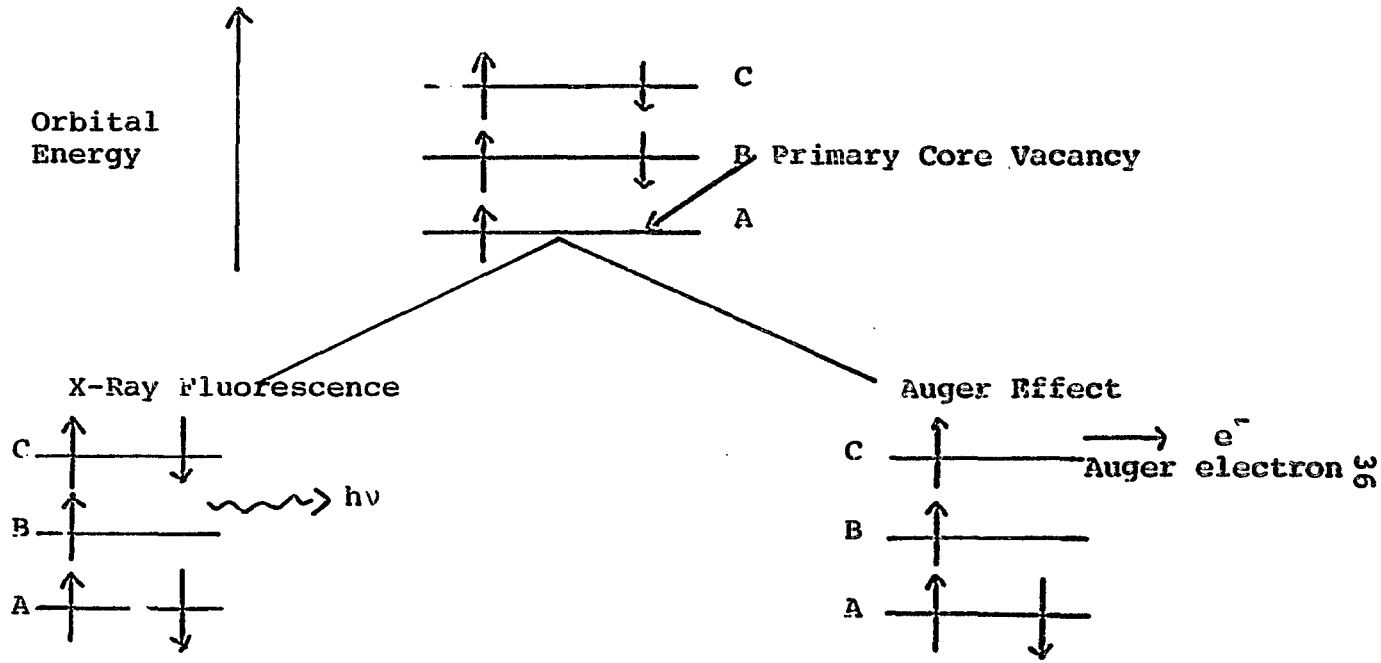

Figure 7: Energy level diagrams of core hole decay modes.

A schematic diagram of the instrumentation required for the ESCA experiment is given in Figure 8 (62). The x-ray source is usually either a magnesium target which has an energy of 1253.7 ev ($K_{\alpha 1,2}$) and a line width of 0.7 ev or an aluminum target of energy 1486.6 ev ($K_{\alpha 1,2}$) and line width 1.0 ev. These are called soft x-ray sources since they have relatively low energies. The sample region or ionization chamber is usually separated from the x-ray source by a metal window to make sure that electrons used to generate the x-rays do not enter the analyzer. The analyzer measures the energy distribution of electrons emitted from the sample. The detector is usually an electron multiplier that counts minute electron currents. These signals are amplified to generate a spectrum. A high vacuum pumping system is crucial because electrons have short mean free paths in the gaseous state, before they are inelastically scattered by collision with bound electrons. The vacuum environment thus allows detection of the electrons by the analyzer (62). More detailed treatments of instrumentation are given by Barrie (66) and Riviere (67).

ESCA provides a hierarchy of surface information (68,69). On the core level, the binding energy of an electron is characteristic of the energy level of a given element. This gives a handle on the elements present at the surface. A

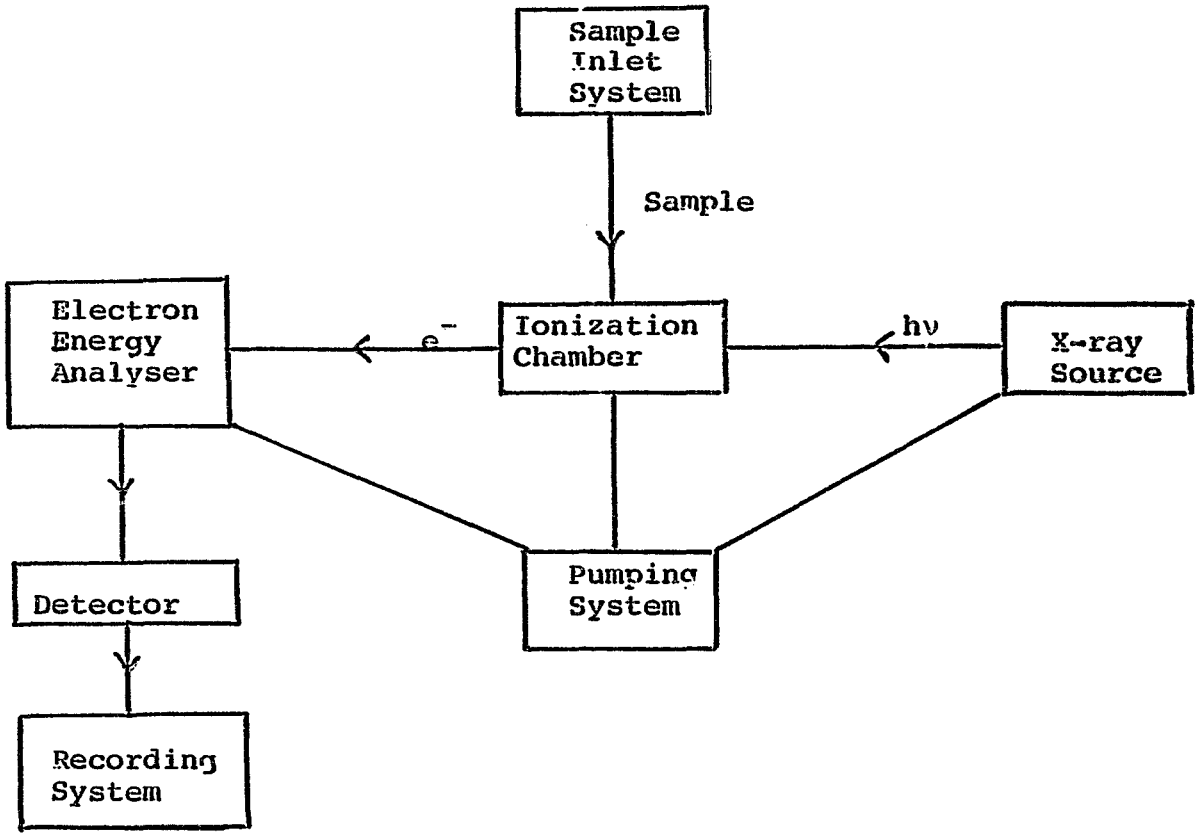

Figure 8: Schematic diagram of ESCA instrumentation.

depth profile can be obtained by studying core levels with different escape depth dependencies. Binding energy shifts may be correlated with electron distributions and allow a deduction of structure and bonding (70,71), as well as of oxidation states (72) of the species. Quantification of all these data is possible (73-76). Sensitivity factors required for this quantification have been determined (77,78). At the valence level, ESCA can provide information of the valence energy levels of insulators (79). One can also study the differential changes in cross section with the photoionization energy. This gives some information on orbital symmetry. Multiplet splittings give insight into paramagnetic systems and are a function of spin states and unpaired electron distributions (68).

Aside from all the information obtainable with the use of this technique, ESCA has many other advantages (80):

1. Any type of sample (gas, liquid, solid) may be examined (65).
2. Only modest sample sizes are required. For solids, samples ranging from 10 - 100 mm may be used.
3. The beam diameter is usually 3 - 10 mm, although one manufacturer markets an instrument with a beam diameter of 150μm, which allows better spatial resolution (81).

4. 95% of the time, samples are not destroyed by the x-irradiation (61). There are some exceptions to this however, as polymer degradation over time has been observed (82, 83).
5. The sampling depth ranges from 40 - 200 nm. The surface sensitivity may be enhanced by varying the electron take off angle as shown in Figure 9 (61). The escape depth of electrons is also dependent on the kinetic energy as shown in Figure 10. Very low and very high energy electrons have large escape depths, therefore surface sensitivity is achieved by measuring electrons in the range between 100 - 1000 eV with escape depths of 100 - 200 nm. (61). By varying the take-off angles, surface homogeneity can be checked (84).
6. Detection limits could go as low as 10^{-3} atomic fraction (81), which is about 1% of a monolayer or 10^{13} atoms per cm^2 (85).
7. All elements in the periodic table, except hydrogen and helium can be detected.
8. Signal to noise ratio is generally between 100 - 1000. Background subtraction techniques may be used to enhance signals (86).

ORIGINAL PAGE IS
OF POOR QUALITY

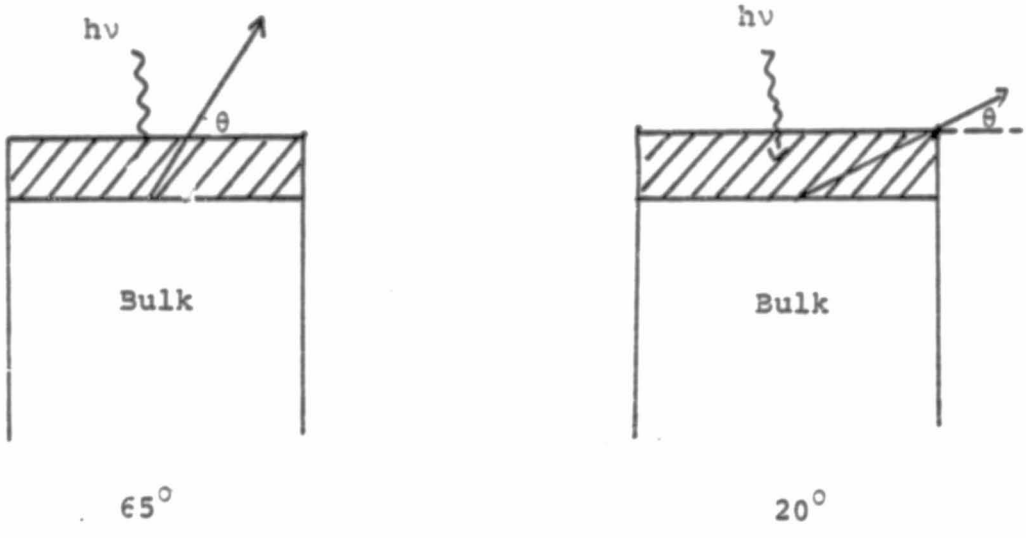

Relative Intensities

Figure 9: Effect of take-off angle on electron escape depths.

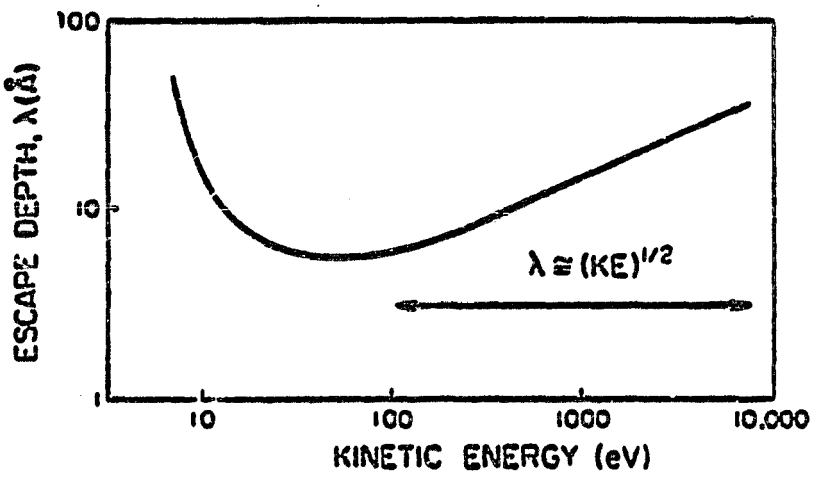

Figure 10: Effect of kinetic energy on escape depth.

All these advantages make ESCA a powerful tool in industry (87,88). In polymer science, it has been used to study copolymer systems (89), polymer synthesis by plasma techniques (90), membranes used in reverse osmosis (91) and the effects of polymer processing on surface properties (92) among other things. It has also been employed in the study of biomaterials and adhesion (93).

2.4 INFRARED SPECTROSCOPY

2.4.1 Dispersive Infrared Spectroscopy

Infrared (IR) spectroscopy is a standard tool in chemistry that has found wide application over the years. It is based on the absorbance of radiation in the infrared region brought about by molecular vibrations of functional groups in a sample (94). The schematic diagram of a typical infrared experiment is shown in Figure 11 (95). The example is that of a dual beam spectrometer. The light from the source is split into two beams. One beam passes through the sample and the other is a reference. A rotating mirror chops the light so that the one from the sample and the reference alternately pulse through a slit to the monochromator, before being dispersed by a grating. The resulting beam at the exit slit of the monochromator is

ORIGINAL PAGE IS
OF POOR QUALITY

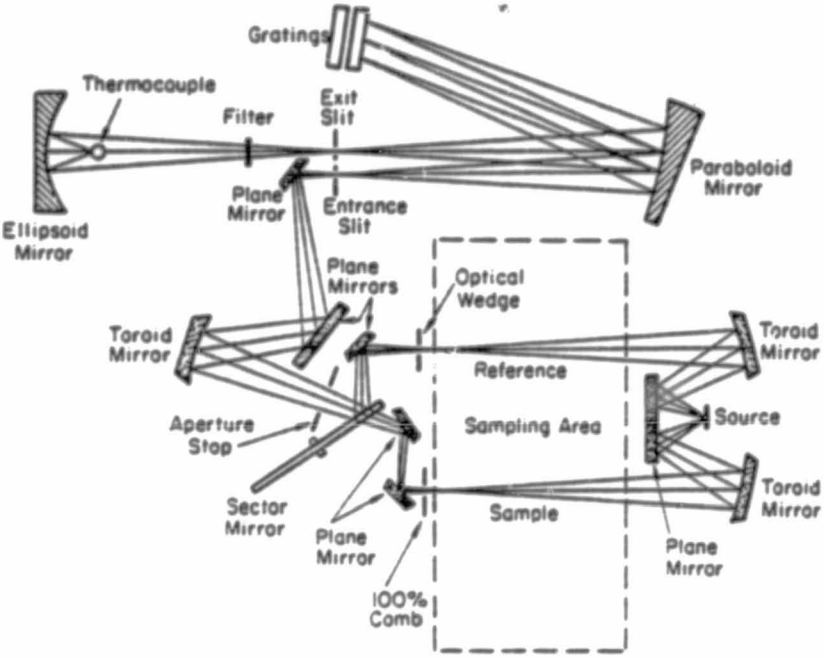

Fig

Figure 11: Optical arrangement of a dispersive ir spectrometer.

filtered and focused onto a thermocouple detector. The alternating signal is amplified and fed to a servo motor that moves a reference beam attenuator to equalize the intensity of the reference. The extent of movement of the reference beam attenuator is proportional to the sample absorbance (95). Dispersive infrared has several disadvantages (96):

1. It has many moving parts.
2. There is no internal frequency reference.
3. The stray light in the system may result in errors in intensity readings.
4. A large part of the total IR energy is wasted.
5. It takes a long time to acquire spectra, thus prohibiting its use as a monitor of rapid physical and chemical changes in the specimen.

2.4.2 Fourier Transform Infrared Spectroscopy

The disadvantages of dispersive infrared spectroscopy opened the door for Fourier Transform Infrared (FT-IR) Spectroscopy, which has a long and interesting history (97-100). A schematic diagram of an FT-IR spectrometer is shown in Figure 12. The source and detector optical path resemble that of dispersive IR. However, the components in between are different. The heart of the FT-IR is a

ORIGINAL PAGE IS
OF POOR QUALITY

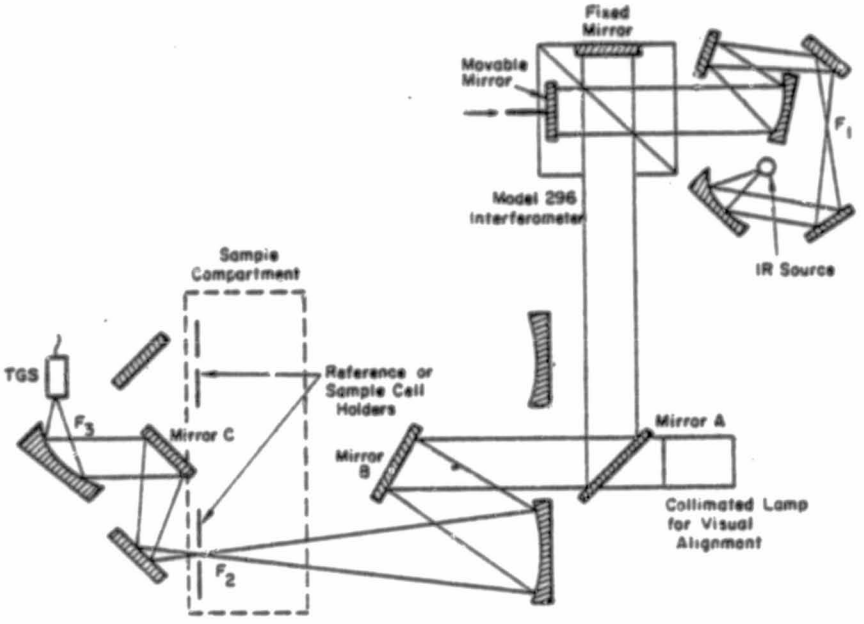

Figure 12: Optical arrangement of an FT-IR spectrometer.

Michelson interferometer that takes the place of the dispersive elements and slits in the conventional IR spectrometer. The light from the source goes to a beam splitter which reflects part of it to a movable mirror and the remainder of it to a fixed mirror. The two components interfere constructively or destructively depending on the difference in optical path and the wavelength of the light. The light intensity at the detector is modulated at audio frequencies governed by the velocity of the movable mirror and the reciprocal of the light wavelength. Because of this, stray light within the interferometer that is unmodulated will not affect the signal at the detector (96). FT-IR is becoming very popular due to its many advantages over dispersive IR (94,101,102) namely,

1. It has higher sensitivity and precision.
2. It can acquire a spectrum in the same period of time it takes dispersive IR to look at one spectral element -- multiplex advantage.
3. It has throughput advantage due to less waste in light energy from the source compared to dispersive IR.
4. FT-IR frequency is internally calibrated by a laser and thus eliminates drifts by frequency exhibited in conventional IR. This capability allows coaddition or subtraction of spectra for comparison (103).

5. FT-IR has a higher signal to noise ratio.

One drawback of FT-IR is that it is not very surface sensitive. Depths of 10 nm in many solid samples have been examined (102).

The advantages of FT-IR have been exploited by many to study effects of surface pretreatments (104), to look at amino acids (105), tacticity, branching and crystallinity in polymers (96) and intermolecular interactions in polymers (101).

2.4.3 Specular Reflectance FT-IR

FT-IR can be used to enhance results obtained using specular reflectance IR. Reflectance IR is used to measure absorbance of film coatings on reflective metal substrates. It can easily be done by adding a simple attachment to FT-IR as shown in Figure 13 (102). The incident beam is led through the polarizer by a plane mirror, M_1. The beam hits the sample surface on an adjustable stage whose position can be varied according to the grazing angle desired. The reflected beam is focused on a concave mirror M_3 after collimation by mirror M_2. It goes back on the optical path by plane mirror M_4.

The light reflected from the metal surface generates a standing wave which has a nonzero electric field at the

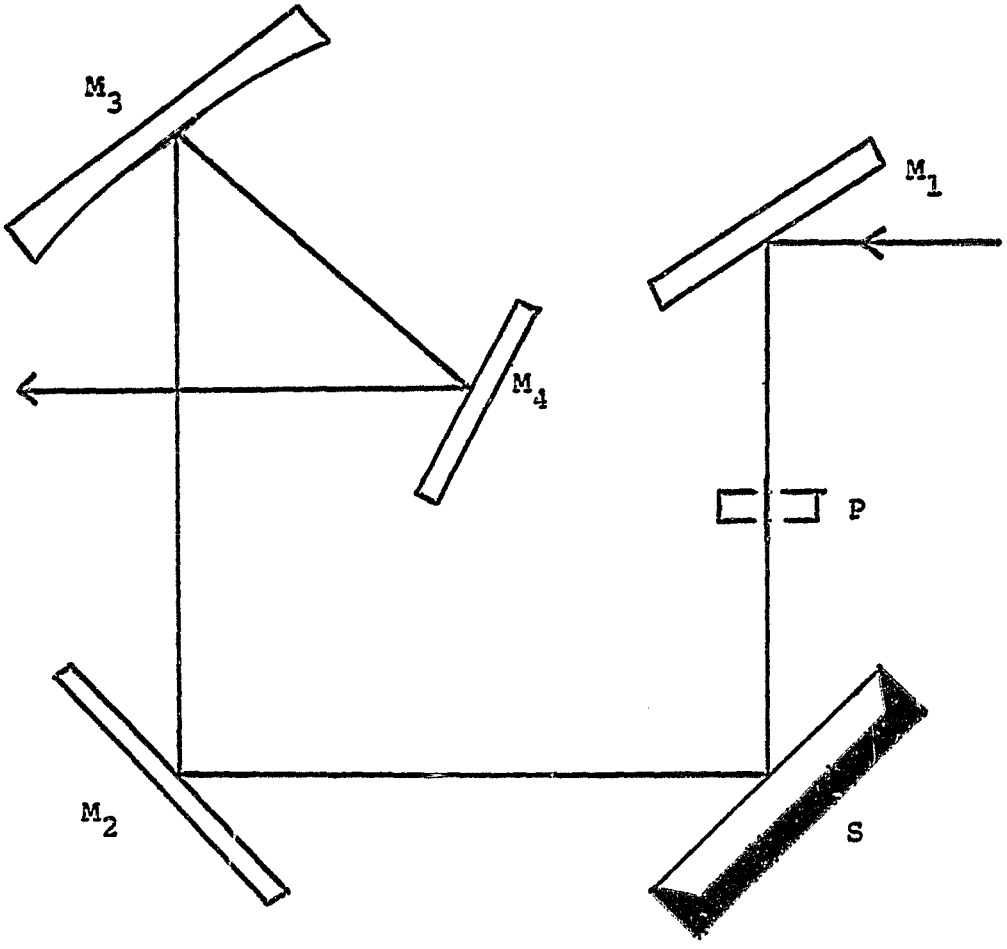

Figure 13: Specular reflectance attachment.

surface. Only the incident radiation electric field which is polarized parallel to the plane of incidence gives rise to a significant surface field. This can interact with the chemical groups at or near the surface resulting in a power loss at the absorbing frequency. IR absorption spectra are then generated (107,108). This behavior can be described by the classical laws of reflection (109) where reflectance is a function of refractive index, extinction coefficient and the angle of incidence (110). Although single reflection experiments usually give good results, multiple reflections may yield higher sensitivity up to the optimum number of reflections characteristic of each metal (108). Sensitivity of the method can be extended to look at about 1 nm films on metals (102).

Caution should be practised in the comparison of transmittance and specular reflectance IR spectra. Peaks may not match since they tend to shift in the reflectance mode. These differences are determined by the strength and shape of the band, the angle of incidence, the film thickness and optical constants of the substrate (111).

Specular reflectance FT-IR has been used to determine the structure of organofunctional silanes adsorbed on metals (112), orientation of fatty acids (113), orientation of polymer fibers (114), structure of epoxy films on metals

(115), chemisorption of organics on oxidized aluminum (116), chemisorption of ethylene on evaporated silver and platinum (117), study Langmuir-Blodgett monolayers (118), plasma sprayed chromium oxide deposits (119) and the creep of thin silicone films (83). However, the technique has been used most extensively in the study of the adsorption of carbon monoxide on various metal surfaces (95).

Chapter III

EXPERIMENTAL

The experimental techniques and procedures used in this study are described in the sections below.

3.1 ROAD TEST

Insect residues were collected in the summer of 1983 (Phase I) and again in the summer of 1984 (Phase II).

3.1.1 Phase I

In a preliminary attempt to collect bug residues, Ferrotype plates (chrome plated steel) measuring 15 cm x 24 cm were mounted on top of automobiles for six to twelve hour trips. For each trip, a polymer coated and an uncoated plate were mounted side by side, with the uncoated plate serving as the control for that trip. Test conditions for the different trips are given in Table 1.

3.1.2 Phase II

3.1.2.1 Roughness

To study the effect of surface roughness on insect adhesion, a series of aluminum strips of known roughness were prepared. Alu[illegible]7075-T6 sheets were cut into 20cm x

TABLE 1

Phase I Trip Conditions

POLYMER	DATE	TRIP DETAILS
Polysulfone	?2July 83	Blacksburg to Naxera, Virginia
		Leave 5:30 pm
		Arrive 12:00 mn
		JPW car
		No rain
Nyebar	10Sept 83	Blacksburg to Bethany Beach,
		Delaware through Eastern
		Shore Peninsula
		Leave 5:30 pm
		Arrive 5:30 am
		HFW car
		No rain, cool, damp

2.5cm strips. This particular aluminum alloy was chosen due to its low elastic modulus which would allow easy bending and straightening out without permanent deformation. These strips were then blasted with very fine G10 glass beads under conditions given in Table 2 to achieve the desired roughnesses. The surface roughening was done by Mr. David Gilliam of the Mechanical Engineering Department at Virginia Tech. The smoothest surface, 0.2μm R_a, was used as received. The roughnesses were determined by Mr. David Gilliam using a Talysurf A profilometer.

3.1.2.2 Polymer Films

To study the role of surface energy on insect adhesion, four polymers having a wide range of critical surface tension were used. The structures of these polymers are shown in Figure 14.

Nyebar™ (will simply be called Nyebar subsequently) is a fluoropolymer obtained from the William Nye Co. at a concentration of 2% in freon. Teflon is an aqueous dispersion, Teflon 30B, from Dupont Paints and Coatings Division. Polysulfone (PSF) is UDEL P 1700 from Union Carbide. Polymethylmethacrylate (PMMA) is Elvasite 2041 from Dupont. Except for teflon, the other polymers were cast in the following manner. Nyebar was used as received.

TABLE 2

Blasting Conditions

Roughness (μm)	Air Pressure (psig)	Nozzle Distance (cm)	Exposure Time (s)
0.2	--	--	--
0.5	60	20	5
0.9	60	20	10
1.3	60	20	18 - 20

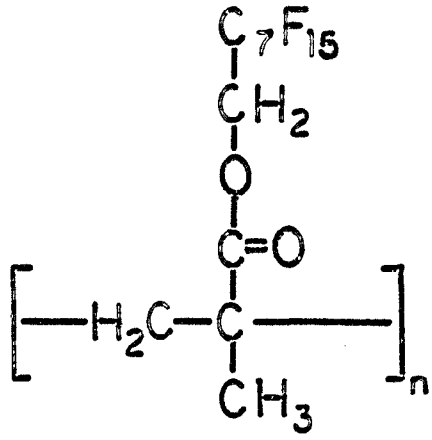

Nyebar

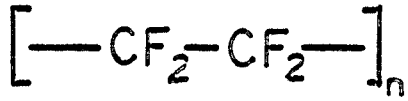

Teflon

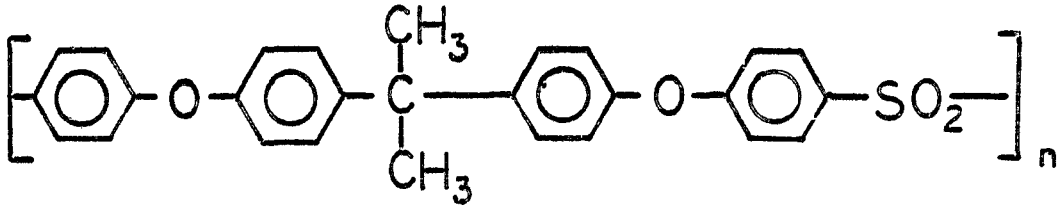

Polysulfone

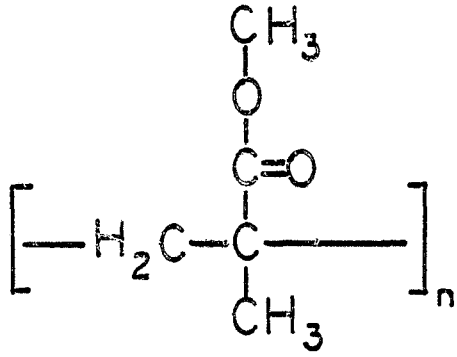

Polymethylmethacrylate

Figure 14: Structures of polymers used.

Solutions (1.5% w/v) of PSF and PMMA in chloroform were made up. A few drops of the solution were placed on the edge of the plate as shown in Figure 15. This liquid was drawn across the plate by a doctor's blade or a nylon blade leaving a very thin film on the substrate.

Teflon films were made by sintering. The aluminum strips were dipped in the aqueous dispersion of teflon. The excess was allowed to drain off in order to get as thin a film as possible. The coated plates were then placed in an air oven at 100°C for two to three minutes to allow water to evaporate, then transferred to the oven at 290°C for about ten minutes to allow the surfactant to desorb. Finally the plates were transferred to oven at 370°C for about twenty five minutes for the sintering process.

3.1.2.3 Sample Mount

The roughened and coated strips were mounted on a jig as shown in Figure 16. The semicircular shape was chosen in order to simulate the geometry of an aircraft wing. For each collection that was made, 36 samples were tested. Of these, four were the uncoated samples of four roughnesses, the 32 others were composed of duplicates of the four roughnesses coated with the four polymers. The strips were mounted in a random fashion. The sample jig was

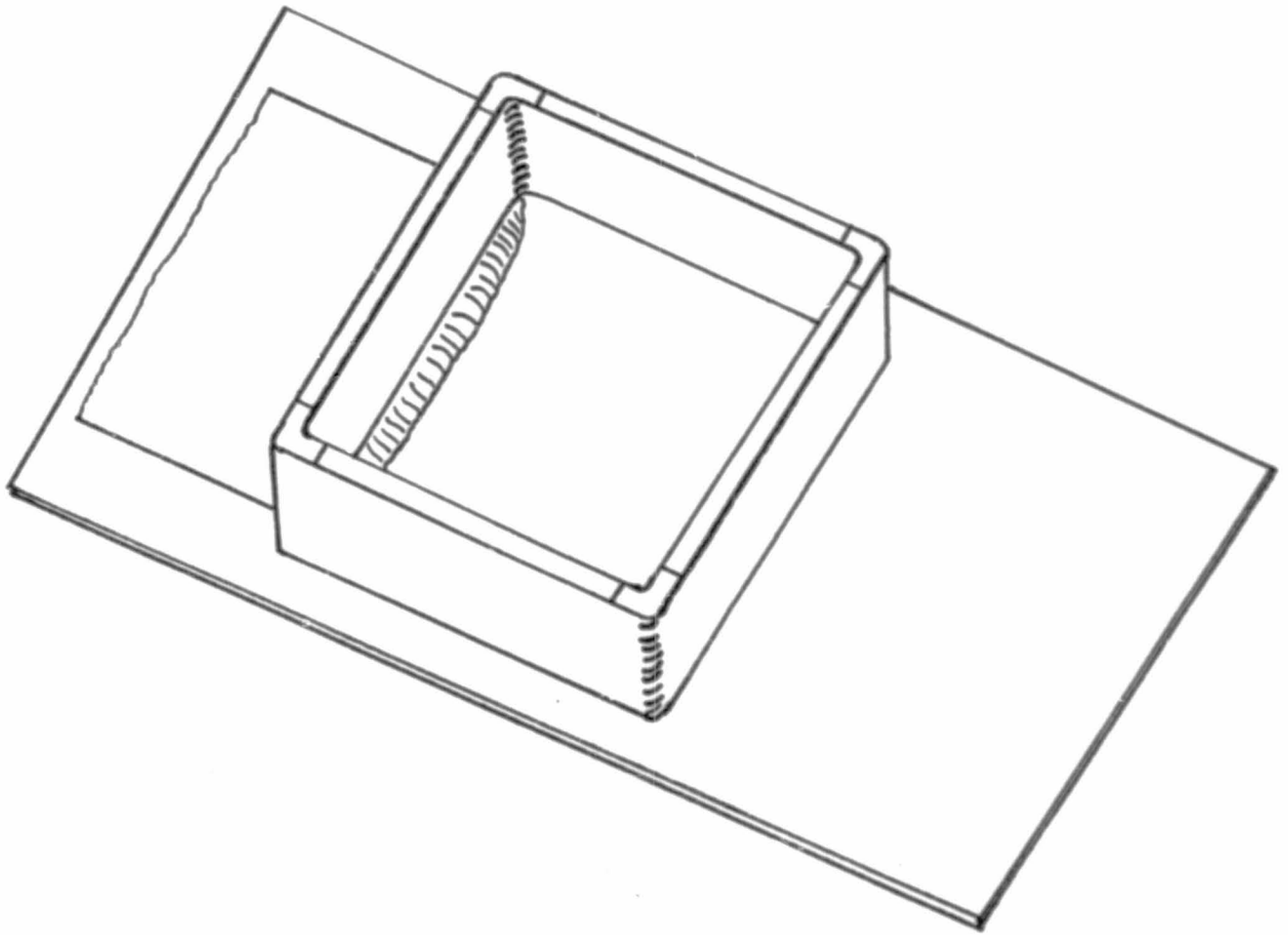

Figure 15: Casting technique

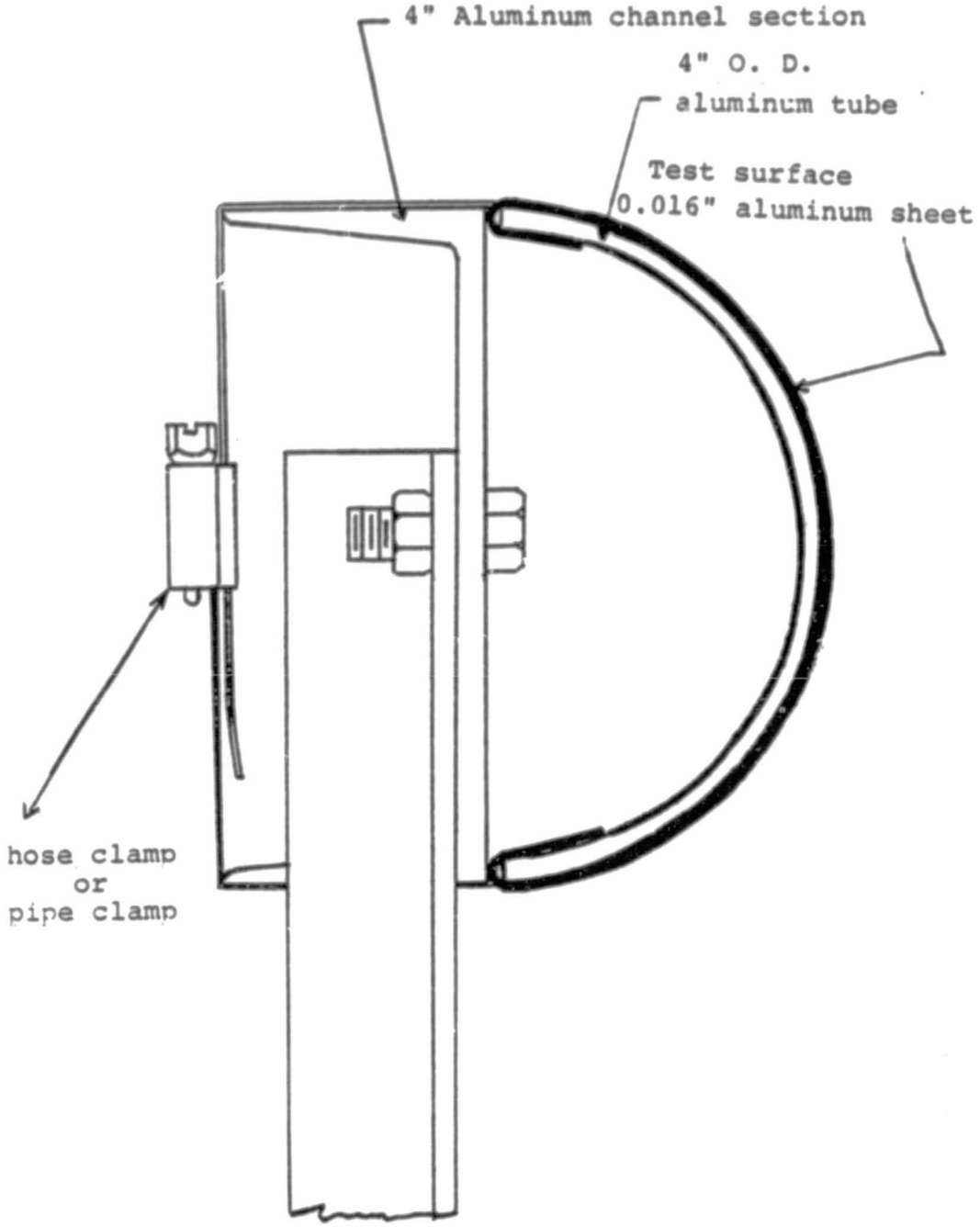

Figure 16: Configuration of sample mount.

subsequently mounted on the car as shown in Figure 17. It stands about two feet above the roof of the car in order to eliminate the effect of turbulent airflow just above the car, on the insect collection experiment. The tests were run in a five mile loop in Gloucester County, Virginia as shown in see Figure 18. The test conditions are given in Table 3.

3.2 CRITICAL SURFACE TENSION

3.2.1 Liquid Surface Tension Measurements

The suface tensions of an ethanol/water series ($V_{absolute\ ethanol}$/ $V_{distilled\ deionized\ water}$: 10/90, 30/70, 50/50, 60/40, 70/30, 80/20, 90/10) were initially determined by the capillary rise method as described by Daniels (120). The experimental set-up is shown in Figure 19.

A modified Wilhelmy plate was subsequently used since the accuracy of the results obtained with the capillary rise method was lacking. The experimental set-up is shown in Figure 20. The method is based on the measurement of the force that a liquid exerts on the perimeter of a platinum foil in the downward direction. The thickness of the foil was 2.54×10^{-3} cm and the width was 1.27 cm. The surface tension γ is given by the equation

ORIGINAL PAGE IS
OF POOR QUALITY

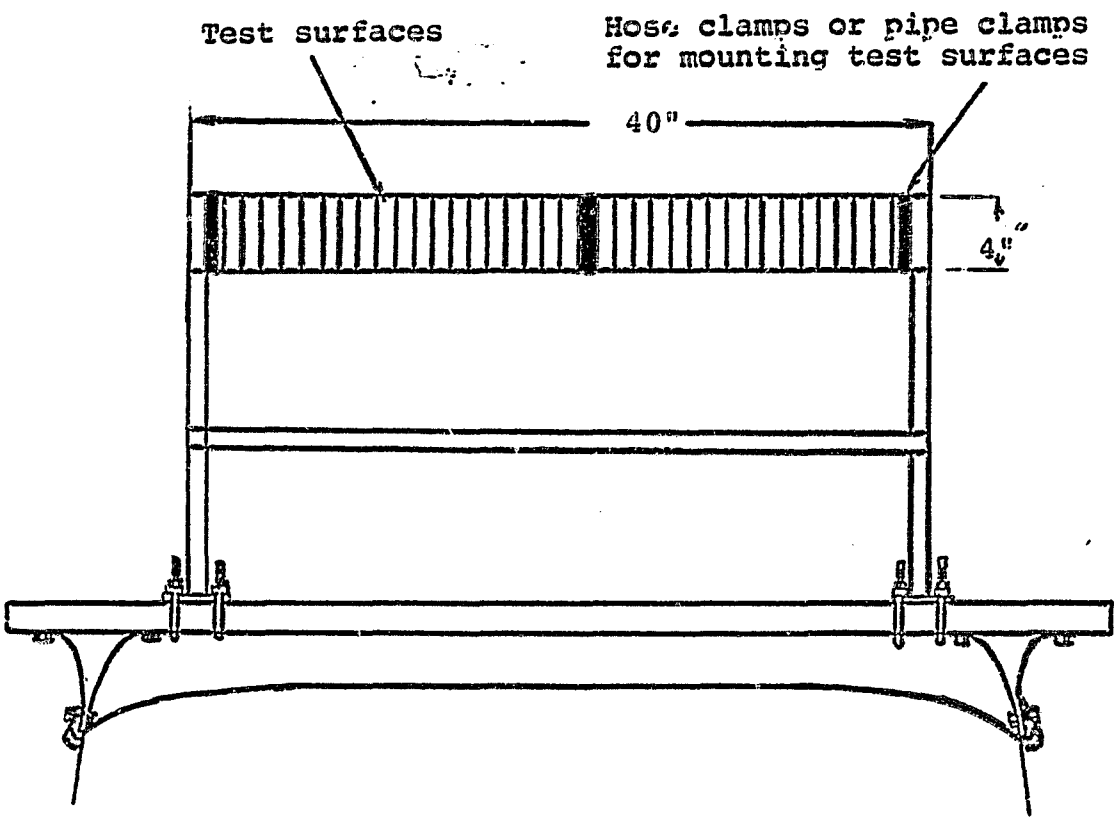

Figure 17: Sample mount set-up.

ORIGINAL PAGE IS
OF POOR QUALITY

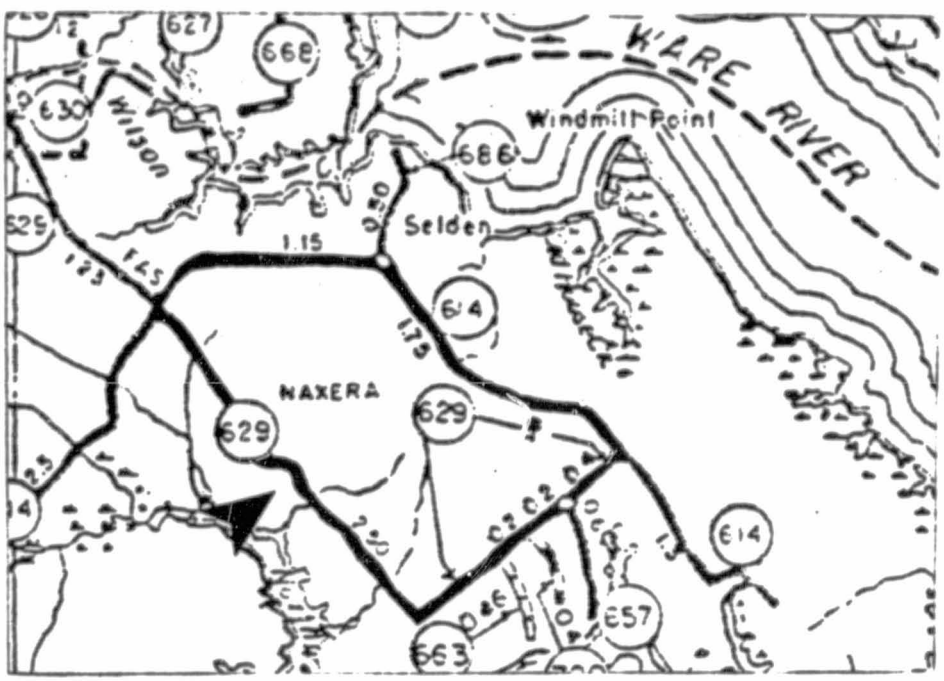

Figure 18: Phase II test site.

TABLE 3

Phase II Test Conditions

Number	Date	Time	Number of times†	Temp.*	R. H.**	Wind	Baro.+	Gen.++
1	31Jul 84	8:30PM	3	76	87	calm	30.18s	p. cl.
2	31Jul 84	9:30PM	5	76	87	calm	30.18s	p. cl.
3	01Aug 84	8:00PM	5	78	88	SW-8	30.17s	p. cl.
4	02Aug 84	8:45PM	3	82	74	S-8	30.15f	p. cl.

† Number of times around the five-mile loop test area

* Temperature in degrees Fahrenheit

** Relative humidity

+ Barometer pressure

++ General weather conditions

ORIGINAL PAGE IS
OF POOR QUALITY

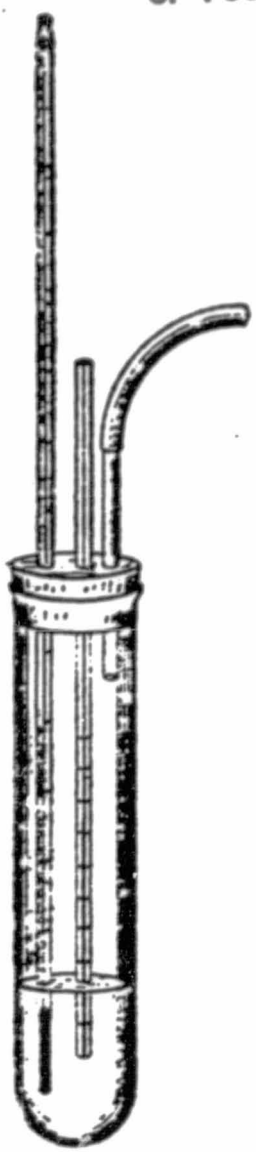

Figure 19: Capillary rise set-up.

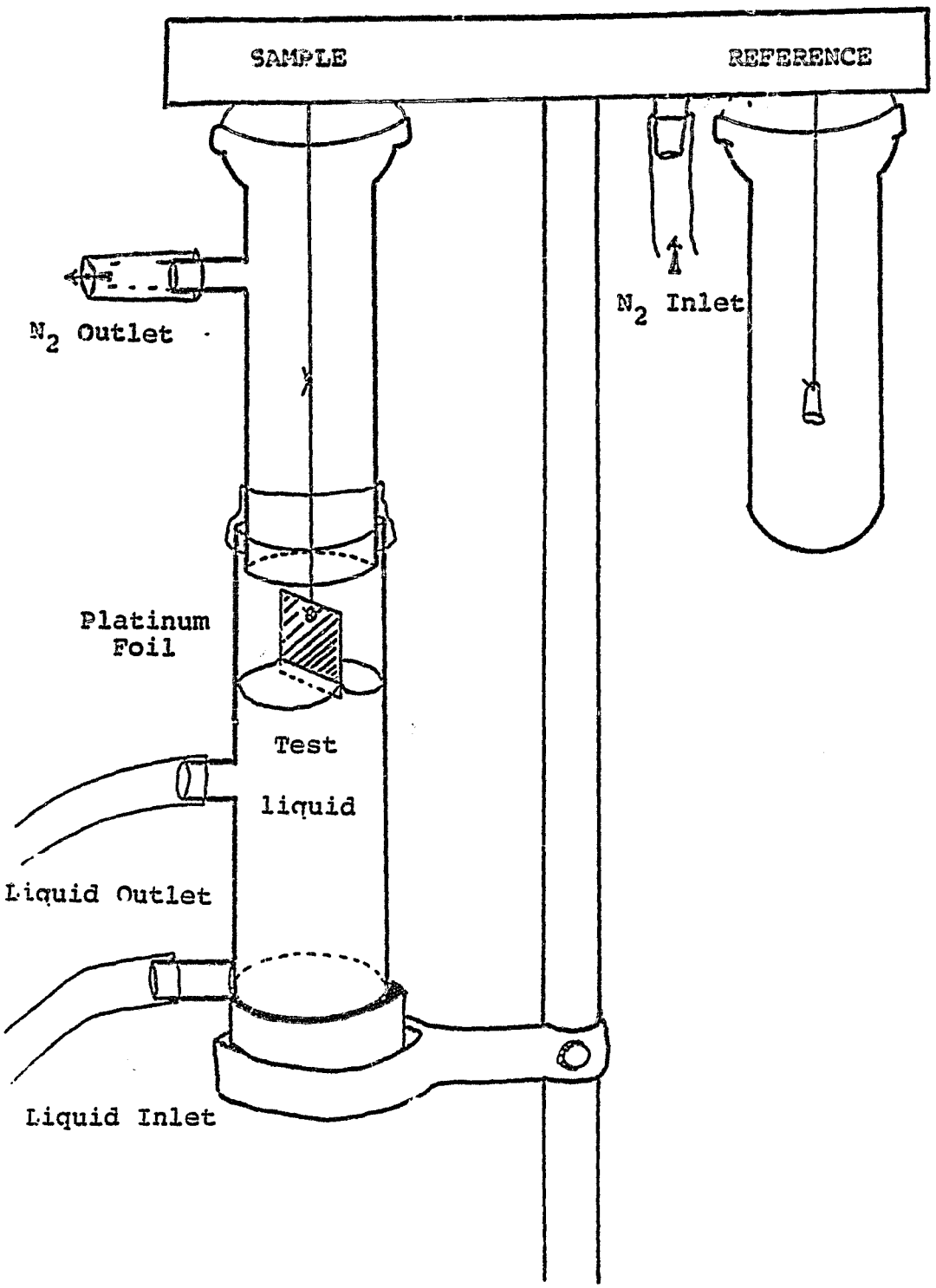

Figure 20: Modified Wilhelmy balance set-up.

$$\gamma = \frac{g(\Delta W + \rho l t w)}{t + w} \qquad [3\text{-}1]$$

where g is the acceleration due to gravity (980 cm/s^2) and ΔW is the difference in weight (in gms.) of the platinum with and without the liquid pulling on it. The term $\rho l t w$ is a buoyancy correction factor, where ρ is the liquid density (in g/cm^2), l is the height (in cm) to which the foil is immersed in the liquid, t is the thickness of the foil (in cm) and w is its width (in cm). If the foil is immersed to zero height, the buoyancy correction factor drops out, leaving ΔW as the only term that needs to be measured (121,122).

Three to five runs were made for each liquid. After each run, the platinum foil was cleaned by flaming with a Bunsen burner, quenched while red-hot in concentrated nitric acid, rinsed with distilled water, then dried with nitrogen.

The same procedure was followed to measure the surface tension of the Zisman liquid series: water, glycerol, formamide, methylene iodide, 1-bromonaphthalene and the alkane series: hexadecane, decane, octane and hexane. All of these liquids were obtained in the purest available form (mostly 99.9%) from Aldrich Chemical Co.

3.2.2 Contact Angle Measurements

Only smooth samples of 0.2μm arithmetic mean roughness (R_a) were used for contact angle measurements to determine critical surface tensions. The samples were prepared in the same manner as in the road tests, cut into 3.8 cm x 2.5 cm samples and stored in the dessicator over Drierite until ready for use.

Prior to contact angle measurement, the Nyebar, PSF and PMMA samples were washed with a soapy Alconox™ solution, rinsed with deionized, distilled water and dried with nitrogen. Teflon was washed with acetone and dried with nitrogen. Water contact angles were also measured on uncoated ferrotype plates and uncoated aluminum strips. The metal samples were cleaned in the same manner as the three polymer films.

Contact angles were measured in a Rame-Hart 100-00 contact angle goniometer shown in Figure 21. The sample and two reservoirs of the liquid of interest were put inside the environmental chamber which was then sealed with Parafilm™. A microsyringe was used to deliver the drops. To obtain the advancing contact angle, a 2μl drop of the liquid was deposited on the polymer substrate. The needle of the syringe was immersed in the liquid drop. If the drop was asymmetric about the needle, the advancing angle was read on

ORIGINAL PAGE IS
OF POOR QUALITY

Figure 21: Rame Hart goniometer.

the side farthest from the needle (123). The procedure was repeated until a constant angle was reached (124). The reading was taken as soon as possible after each additional increment to insure that minimal evaporation occurred and the true advancing angle was obtained (125). To determine the receding angle, the liquid was withdrawn in 2µl increments and the angle read until all the liquid was recovered.

3.2.3 Polar and Dispersion Components

Polar and dispersion components of the liquid surface tensions were determined by measurement of advancing angles on paraffin wax. Gulf wax was melted in a petri dish. The metal substrates were immersed in the liquid wax. The plates were allowed to cool and then stored until use. To obtain a sample for contact angle measurement, the plates were cut out and the hardened wax was smoothed by passing a hot razor blade over the surface just before the measurements were taken.

3.3 SURFACE CHARACTERIZATION BEFORE AND AFTER INSECT IMPACT EXPERIMENTS

3.3.1 Surface Energy

To determine if the road exposure severely altered the surface energy of the polymer fi[illegible], relatively clean areas on randomly picked samples were chosen. Water advancing angles were measured as described above, for comparison with the unexposed plates.

3.3.2 ESCA

The ESCA spectra of freshly cast polymer films were obtained on 0.95 cm disks punched from plates coated with the film of interest. For samples exposed to the road, two sets of samples were chosen. One set consisted of 0.2μm R_a series of polymers and controls. The second set consisted of 1.3μm R_a samples. 0.95 cm diameter disks were punched from areas free of insect residues. ESCA spectra were obtained using a Kratos XSAM 800 x-ray photoelectron spectrometer with a Mg K_α x-ray source.

Take-off angle dependence studies were also undertaken on the unexposed samples of polymers. The take-off angle was varied from 10^0 to 30^0 to 90^0.

3.3.3 Specular Reflection FT-IR

Infrared spectra of freshly cast polymer films were obtained on 5 cm x 2.3 cm samples of coated aluminum or ferrotype plates. The experiment was performed only on the smooth samples. The experiments were run in a Nicolet MX-1 FT-IR spectrometer with a specular reflectance attachment shown in Figure 22 at a grazing angle of 70°.

3.3.4 Scanning Electron Microscopy

Disks were punched from different areas of the same specimens chosen for ESCA analysis. These areas contained some form of bug debris. The samples were sputter coated with gold by an SPI sputter coater for 35 seconds and at 35 mA. SEM photomicrographs were taken with a JEOL 35C scanning electron microscope.

3.4 CORRELATION OF SURFACE ENERGY AND SURFACE ROUGHNESS TO INSECT CONTAMINATION

3.4.1 Phase I

3.4.1.1 Bug Counts

Bug density on the plates was determined by random sampling. A grid with squares measuring 1.3 cm x 1.3 cm was laid over the plate. The squares were assigned numbers according to row and column. A random number table (126) was then used to determine which squares should be chosen

ORIGINAL PAGE IS
OF POOR QUALITY

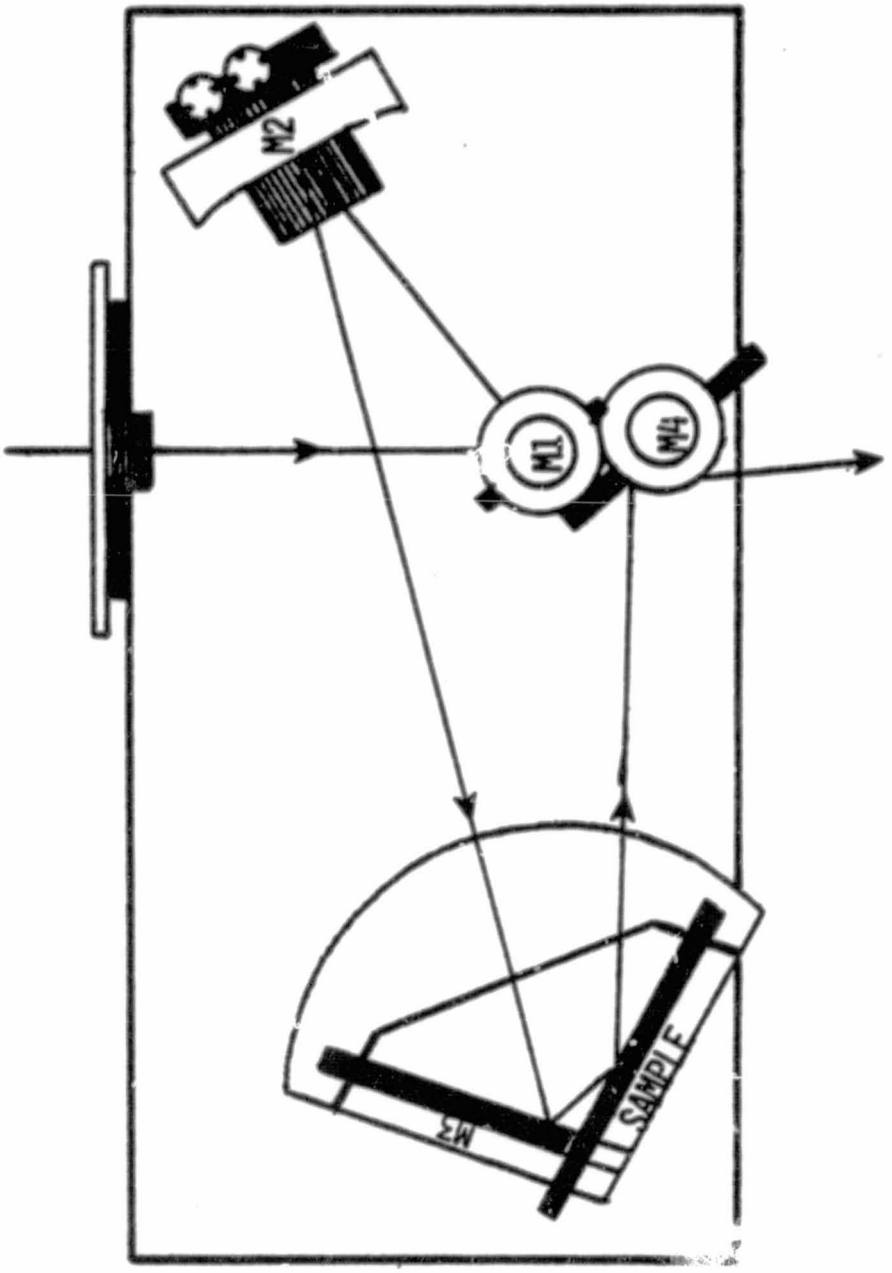

Figure 22: Specular reflectance attachment.

for counting. Ten boxes were chosen and the bug debris counted under a microscope. The debris were classified as(i) bug parts, (ii) bug splats, (iii) whole bugs and (iv) whole bugs and splats. The densities were obtained by dividing the number of bugs by the total area (16.9 cm^2) of the ten boxes.

3.4.2 Phase II

3.4.2.1 Bug Counts

The debris on all the samples were counted with the naked eye. The same classification was used as in Phase I.

3.4.2.2 Area Moments

To obtain a means of measurement with some sort of weighting factor, moments were calculated. The length of a bug was measured to the closest mm with a straight rule. The distance away from the stagnation line was then measured, also to the nearest mm. The stagnation line is shown in Figure 23. The point at which the wings of the insects are split open was taken as the zero point. The area moment is then calculated as

$$\text{Area Moment} = \frac{\text{size (mm) x distance (mm)}}{\text{total number of bugs}} \qquad [3\text{-}2]$$

ORIGINAL PAGE
COLOR PHOTOGRAPH

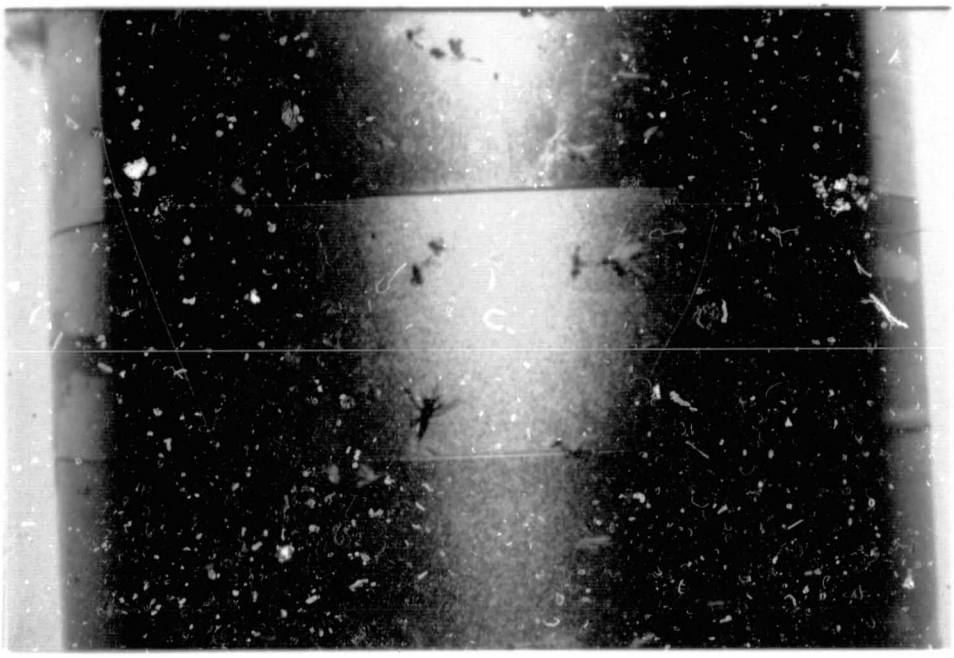

Figure 23: Stagnation line.

3.4.2.3 Height Moments

The heights of the residues were measured under a Wild-Heerbrugg M-420 microscope by Mr. David Gilliam. A sample was first examined by the naked eye for any signs of bug impact. These spots were then examined microscopically to confirm that they were bug residues. To measure the height, the microscope was set at a magnification of 32x and first focused on the surface of the plate. The reading on the focusing dial was taken. The microscope was then focused on the uppermost portion of the residue and the focusing dial reading taken again. The difference between these two numbers was the height of the residue. The detection limit of the microscope was 2.5μm. The distance from the stagnation point was measured as in the area moments. Height moments were calculated as

$$\text{Height Moment} = \frac{\text{height (mm) x distance (mm)}}{\text{total number of impacts}} \qquad [3\text{-}3]$$

3.5 BUG IDENTIFICATION

The insects were identified by Dr. John Eaton of the Entomology Department at Virginia Tech, according to class, order and family.

Chapter V

RESULTS AND DISCUSSION

4.1 SURFACE ROUGHNESS

The Talysurf traces of the four roughened aluminum surfaces are shown in Figure 24. The numbers were obtained by locating the mean horizontal line such that the peak areas above and below the line are equal. The absolute values of all the y coordinates were then totalled and divided by the sum of points to give the arithmethic mean roughness (R_a). Values of R_a ranged from 0.2μm to 1.3 μm.

SEM photomicrographs of the four roughened surfaces are shown in Figures 25 and 26. Note that for the 0.2μm R_a surface, there is no distinguishing feature. The 0.5μm R_a surface is composed of a balance of smooth aluminum and patches of craters created by glass bead blasting. The 0.9μm R_a surface is dominated by craters, with a few patches of smooth aluminum. Finally, the 1.3μm R_a surface is totally composed of craters.

SEM photomicrographs of an uncoated and a polysulfone coated 1.3μm R_a surface are shown in Figure 27. The fact that features characteristic of the roughened substrate are seen in the coated sample suggests that the thin polymer film does not mask the substrate roughness. The

ORIGINAL PAGE IS
OF POOR QUALITY.

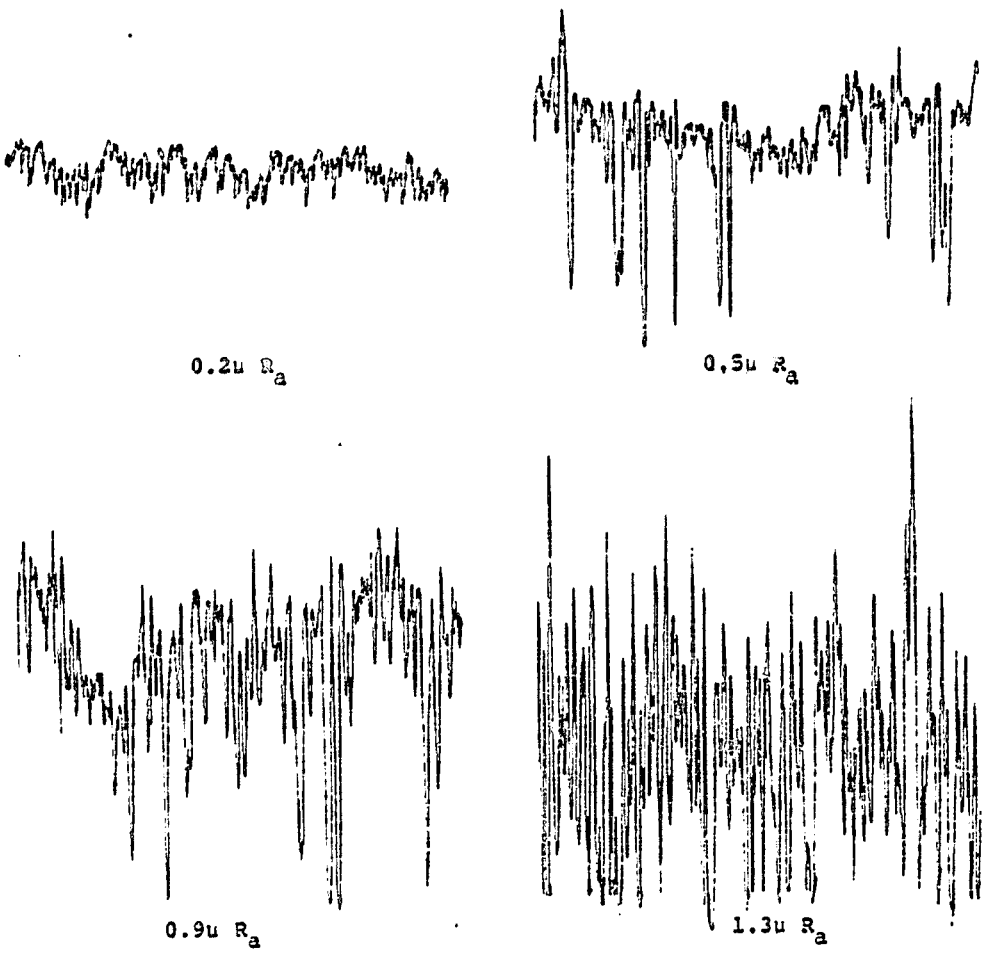

Figure 24: Talysurf traces of four roughened aluminum substrates.

ORIGINAL PAGE IS
OF POOR QUALITY

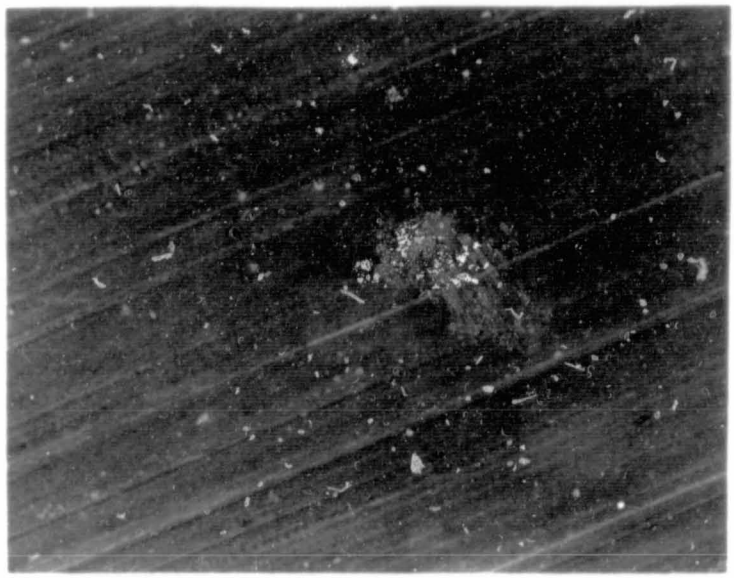

0.2 μm 200x

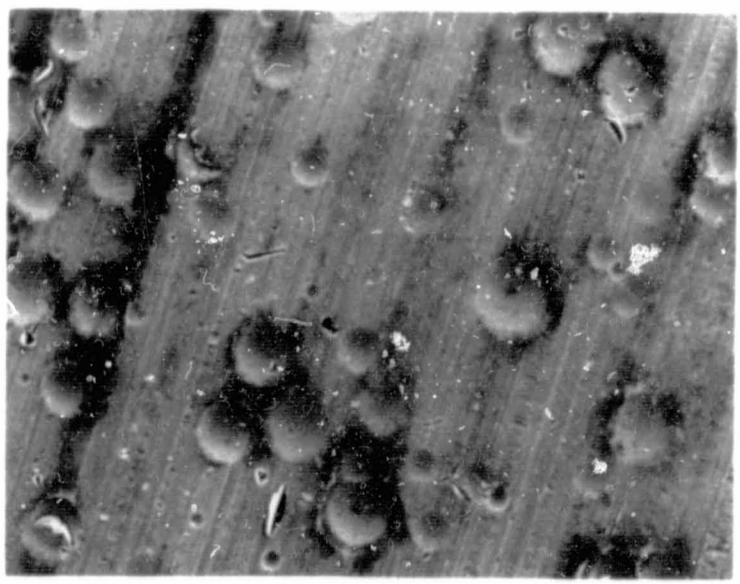

0.5 μm 200x

Figure 25: SEM photomicrographs of 0.2 μm R_a and 0.5 μm R_a substrates

ORIGINAL PAGE IS
OF POOR QUALITY

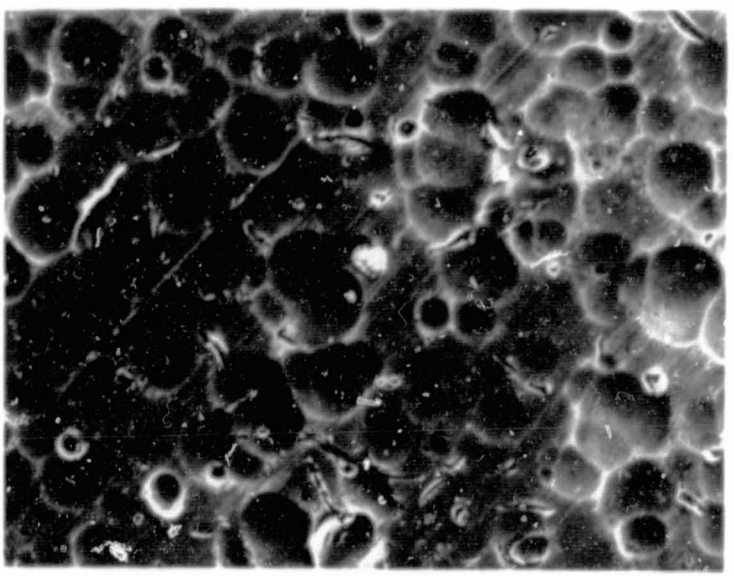

0.9 μm 200x

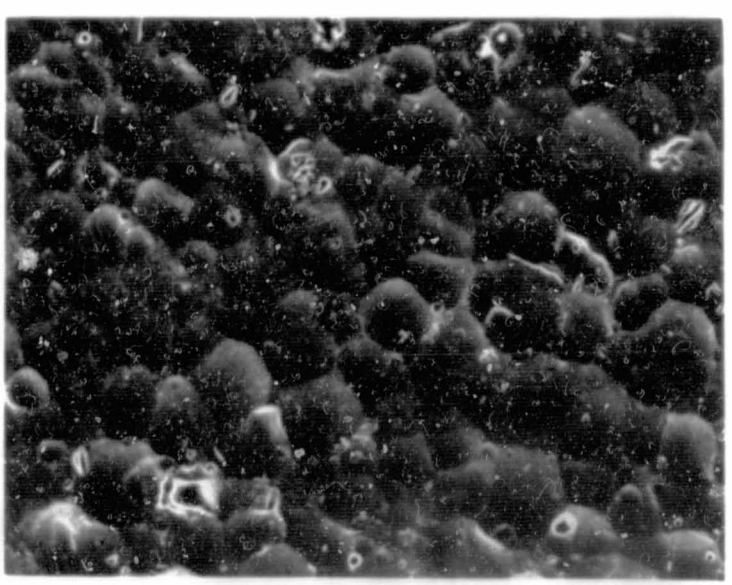

1.3 μm 200x

Figure 26: SEM photomicrographs of 0.9 μm R_a and 1.3 μm R_a substrates

ORIGINAL PAGE IS
OF POOR QUALITY

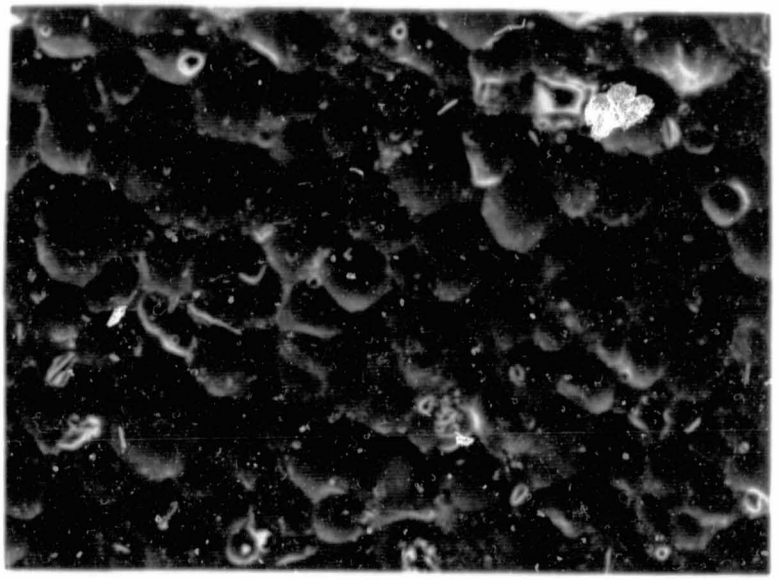

Uncoated 1.3μm substrate 200x

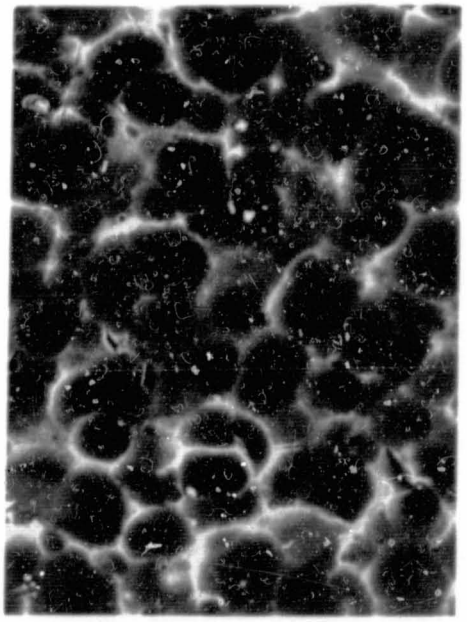

PSF coated 200x

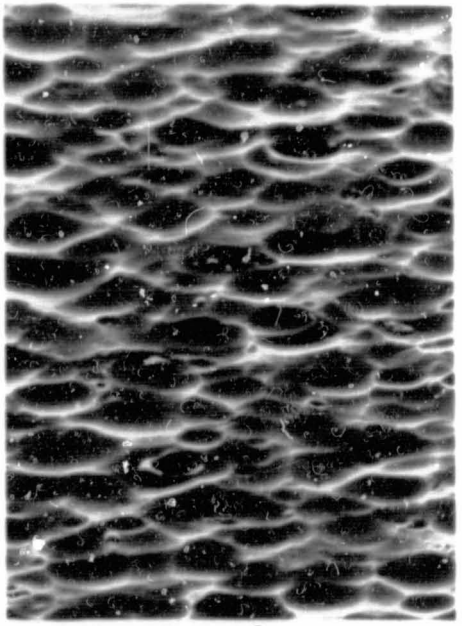

Tilted 60° 200x

Figure 27: SEM photomicrographs of Polysulfone coated and uncoated 1.3 μm substrates

photomicrograph taken with the sample tilted 60° towards the scintillator shows more clearly that no significant masking of the substrate roughness due to polymer coating occurred. The limited masking is also borne out by Talysurf measurements on Nyebar, PSF and PMMA coated surfaces as shown in Table 4. Except for PMMA 0.5μm R_a, the roughnesses, which show the range of roughnesses measured on each surface, exhibit no significant masking for the three polymers that were solvent cast.

The teflon coated samples show different results. The values listed in Table 4 indicate significant masking at the higher roughnesses such that in effect, there are only two roughnesses instead of four. The reason for this is seen in the SEM photomicrographs in Figure 28. The sintering of the thicker teflon coating resulted in a dimpled film of uncontrolled roughness that totally masked the initial roughness created on the aluminum substrate. In fact, the aluminum substrate is not even visible in any of the photomicrographs. The fact that the teflon film is considerably thicker than the other films appears to have a pronounced effect on the sticking of insect residues as described below.

TABLE 4

Comparison of Talysurf Results Before and After Polymer Coating

Sample	Roughness (μm)			
Control	0.2	0.50 - 0.65	0.85 - 1.1	1.2 - 1.4
Nyebar	0.2	0.45 - 0.70	0.90 - 1.0	1.1 - 1.2
Control	0.2	0.45 - 0.60	0.80 - 1.0	1.2 - 1.3
Teflon	0.18	0.38	0.31	0.40
Control	0.2	0.45 - 0.60	0.90 - 1.0	1.3 - 1.5
Polysulfone	0.18	0.37 - 0.50	0.80 - 0.90	1.2
Control	0.2	0.40 - 0.60	0.90 - 1.0	1.3 - 1.5
Polymethylmethacrylate	0.17	0.25 - 0.30	0.97	1.1

ORIGINAL PAGE IS
OF POOR QUALITY

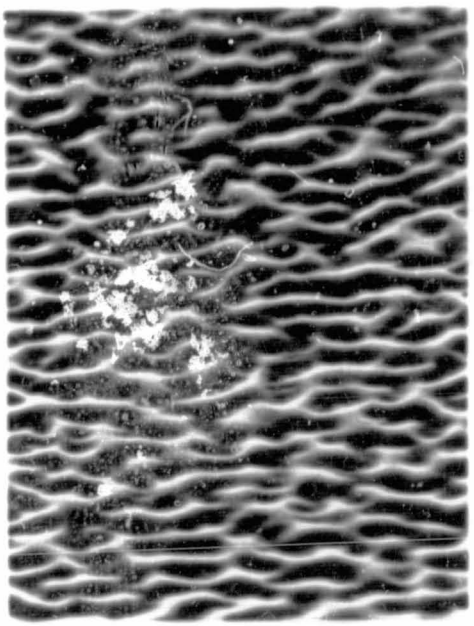

0.2 μm 2000x

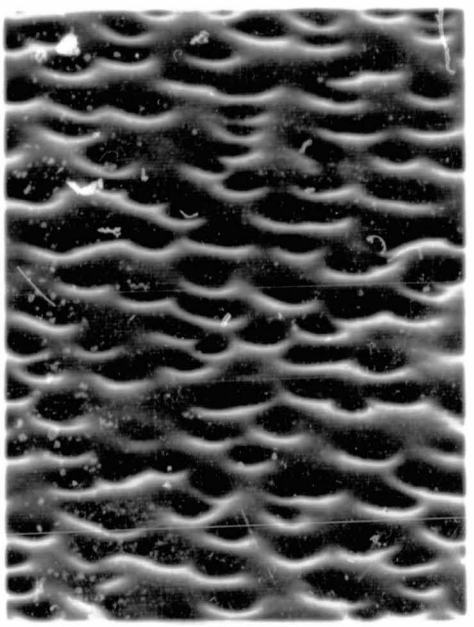

0.5 μm 2000x

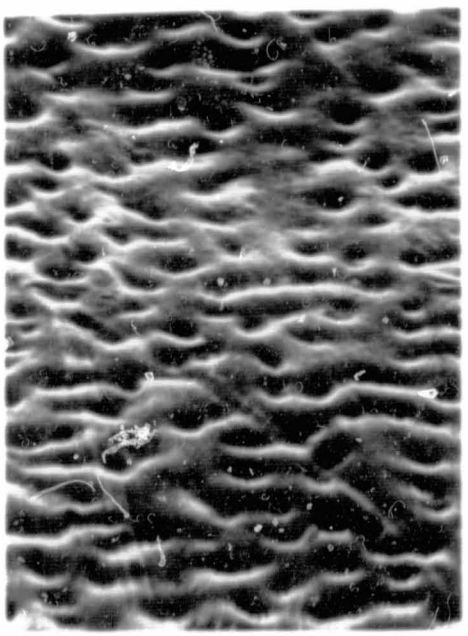

0.9 μm 2000x

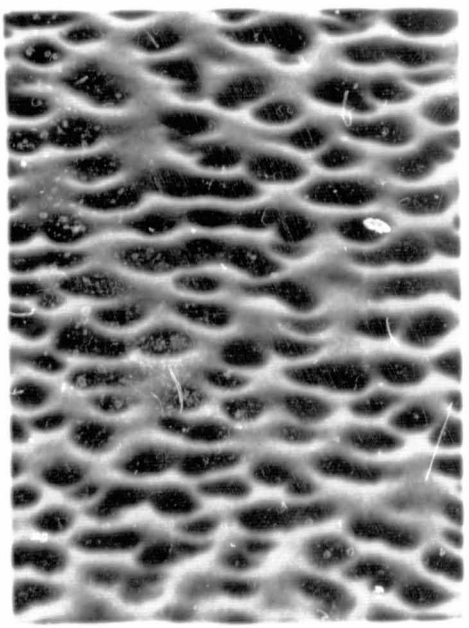

1.3 μm 2000x

Figure 28: SEM photomicrographs of teflon coated substrates

4.2 SURFACE TENSION

Surface tensions determined for the aqueous ethanol solutions are shown in Table 5. A comparison with the values reported by Dann (54) shows that the Wilhelmy balance is a more suitable method than the capillary rise method for measuring the surface tensions of solutions. A comparison of the Wilhelmy balance and capillary rise results can be made by plotting the values of surface tension versus the percentage of alcohol by volume. The results are shown in Figure 29. It can be seen from the graph that the values obtained by the Wilhelmy method are in good agreement with the values reported by Dann (54). On the other hand, the general shape of the curve for the capillary rise method is the same as that for the other two. However, the capillary rise curve plateaus off at a higher value. This behavior may be due to some hydrogen bonding occurring between the solution and the glass. Water may preferentially adsorb at the glass surface, thus introducing a significant error in the measurements of the surface tension of the homogeneous solution. Preferential adsorption thus makes the capillary rise method unsuitable for solutions (127).

The Wilhelmy balance was also used to measure the surface tensions of the Zisman series liquids. The results are shown in Table 6.

TABLE 5

Surface Tensions of Aqueous Ethanol Solutions

Solution (EtOH/H_2O by volume)	γ^{*}_{wb} (dynes/cm)	γ^{**}_{lit} (dynes/cm)	γ^{+}_{cr} (dynes/cm)
Water	72.0 ± 0.8	72.2	71.8
10/90	50.5 ± 0.7	51.3	55.4 ± 0.2
30/70	36.5 ± 0.2	36.1	53.3 ± 0.1
50/50	31.2 ± 0.08	30.0	45.0 ± 0.02
60/40	29.5 ± 0.07	28.0	42.8 ± 0.08
70/30	28.1 ± 0.04	27.2	42.9 ± 0.07
80/20	26.7 ± 0.03	25.6	39.9 ± 0.07
90/10	25.2 ± 0.03	24.0	38.0 ± 0.07
EtOH	-	22.5[++]	-

* Surface tension measured with the Wilhelmy plate method

** Surface tension values used by Dann (reference 54)

\+ Surface tension measured by the capillary rise method

++ From reference 128

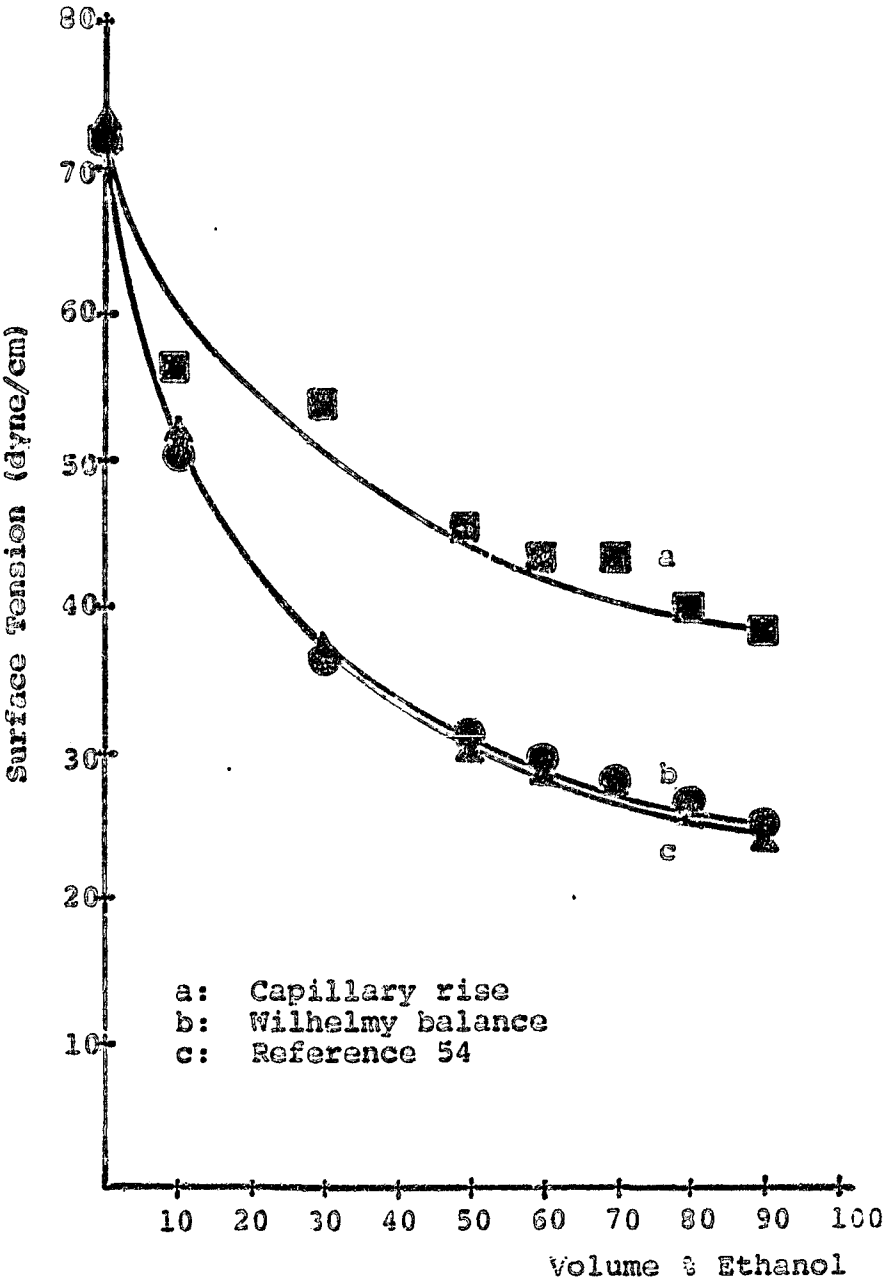

Figure 29: Comparison of surface tension values by capillary rise and Wilhelmy plate method.

TABLE 6

Surface Tensions of the Zisman Series

Liquid	γ^{*}_{wb} (dynes/cm)	γ^{**}_{lit} (dynes/cm)
Water	72.0 ± 0.8	72.2
Glycerol	63.4 ± 0.2	63.4
Formamide	59.2 ± 0.3	58.2
Methylene Iodide	50.6 ± 0.5	50.6
1-Bromonaphthalene	44.1 ± 0.4	44.6
Hexadecane	27.6 ± 0.06	26.5
Decane	23.8 ± 0.03	23.8
Octane	21.6 ± 0.06	21.6
Hexane	18.3 ± 0.06	18.3

* Surface tension measured by the Wilhelmy plate method

** Surface tension values used by Dann (reference 54)

The results show excellent agreement with literature values as well as high precision. This implies that the Wilhelmy plate method is more versatile than the capillary rise method in the measurement of surface tensions of both pure liquids and solutions.

4.2.1 Polar and Dispersion Components of Liquids

The contact angles obtained for the ethanol solutions and the Zisman series on paraffin are shown in Tables 7 and 8 respectively. There is a good agreement between the experimental and the literature values. The contact angles of the liquids on paraffin show a discrepancy with the reported values of about 2^{o}. However, this difference is within experimental error for measurements between labs.

Assuming that γ_s^d for paraffin is 25.5 dynes per cm, γ_1^d is given by

$$\gamma_1^d = (\cos\theta + 1)\gamma_1 / 2\sqrt{\gamma_s^d} \qquad [4\text{-}1]$$

If the dispersion and polar components are additive and are the only types of forces contributing to the liquid surface tension, then

$$\gamma_1 = \gamma_1^d + \gamma_1^p \qquad [4\text{-}2]$$

The calculated liquid surface tension components are shown in Tables 9 and 10. Comparison is also made with literature values. Generally good agreement was obtained. Although

TABLE 7

Contact Angles of Aqueous Ethanol Solutions on Paraffin

Liquid ($EtOH/H_2O$)	Advancing Angle	Advancing Angle (ref 54)	Mole% Alcohol
Water	110.4	110	0
10/90	99.2	97	5.6
30/70	78.0	80	18.6
50/50	61.8	61	34.7
60/40	56.3	55	44.5
70/30	51.9	50	55.3
80/20	47.0	45	68.1
90/10	41.0	39	82.7

TABLE 8

Contact Angles of Zisman Series on Paraffin

Liquid	Advancing Angle	Advancing Angle(ref 54)
Water	110.4	110
Glycerol	95.2	96
Formamide	91.9	91
Methylene Iodide	65.0	61
1-Bromonaphthalene	38.4	38

TABLE 9

Polar and Dispersion Components of Aqueous Ethanol Solutions

Liquid	γ_l^d (dynes/cm)	γ_l^p (dynes/cm)	γ_{lit}^d*(dynes/cm)	γ_{lit}^p*(dynes/cm)
Water	21.5	50.5	22.0	50.2
10/90	17.6	32.9	19.9	31.3
30/70	19.1	17.4	17.3	17.6
50/50	20.7	10.5	19.2	12.3
60/40	20.6	8.9	18.9	10.4
70/30	20.2	7.9	19.4	9.7
80/20	19.8	6.9	18.6	8.3
90/10	19.2	6.0	17.8	6.8

*reference 54

TABLE 10

Polar and Dispersion Components of the Zisman Series

Liquid	γ_l^d (dynes/cm)	γ_l^p (dynes/cm)	γ_{lit}^d* (dynes/cm)	γ_{lit}^p* (dynes/cm)
Water	21.5	50.5	21.8 ± 0.7	51
Glycerol	32.6	30.8	37.0 ± 4	26.4
Formamide	32.1	27.1	39.5 ± 7	18.7
Methylene Iodide	50.8	-0.2	48.5 ± 9	2.3
1-Bromonaphthalene	60.7	-16.6	47.0 ± 7	-2.4

*reference 54

the discrepancy between contact angle values were as small as 2°, the difference in the dispersion component could be as much as 7 dynes per cm, as in the case of formamide. This is due to the sensitivity of $\cos\theta$ to changes in contact angle. Since $(\cos\theta + 1)$ has to be squared in equation [4-1] to obtain the dispersion component, the 2° error in contact angle is compounded and reflected in the calculated dispersion component.

The polar components obtained for methylene iodide and 1-bromonaphthalene are negative. This is because the calculated dispersion components by this method were larger than the total surface tension. The error arises from the fact that these two liquids attacked the paraffin surface thus resulting in a lower contact angle and an invalid calculated value of γ_1^d.

Shown in Figures 30 and 31 are the graphs of the surface tension components versus the total surface tension of the aqueous ethanol solutions and the Zisman series respectively. In both cases the polar component increases with increasing surface tension. For the ethanol solutions, the dispersion component stays about constant, so that the increase in the total surface tensions is mostly due to the increase in the polar component. In the Zisman series, the total surface tensions of the series from hexadecane to

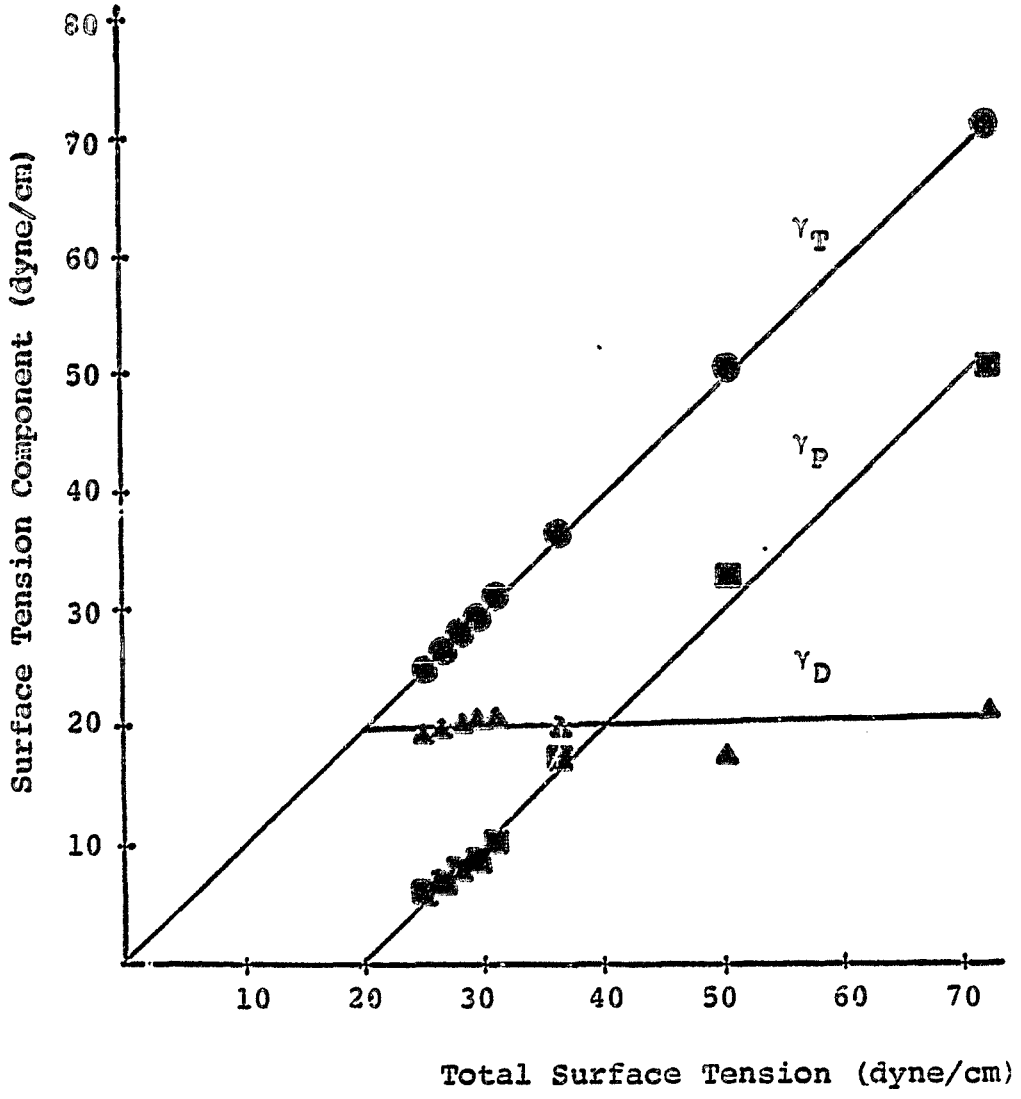

Figure 30: Polar and dispersion components of aqueous ethanol solutions surface tensions.

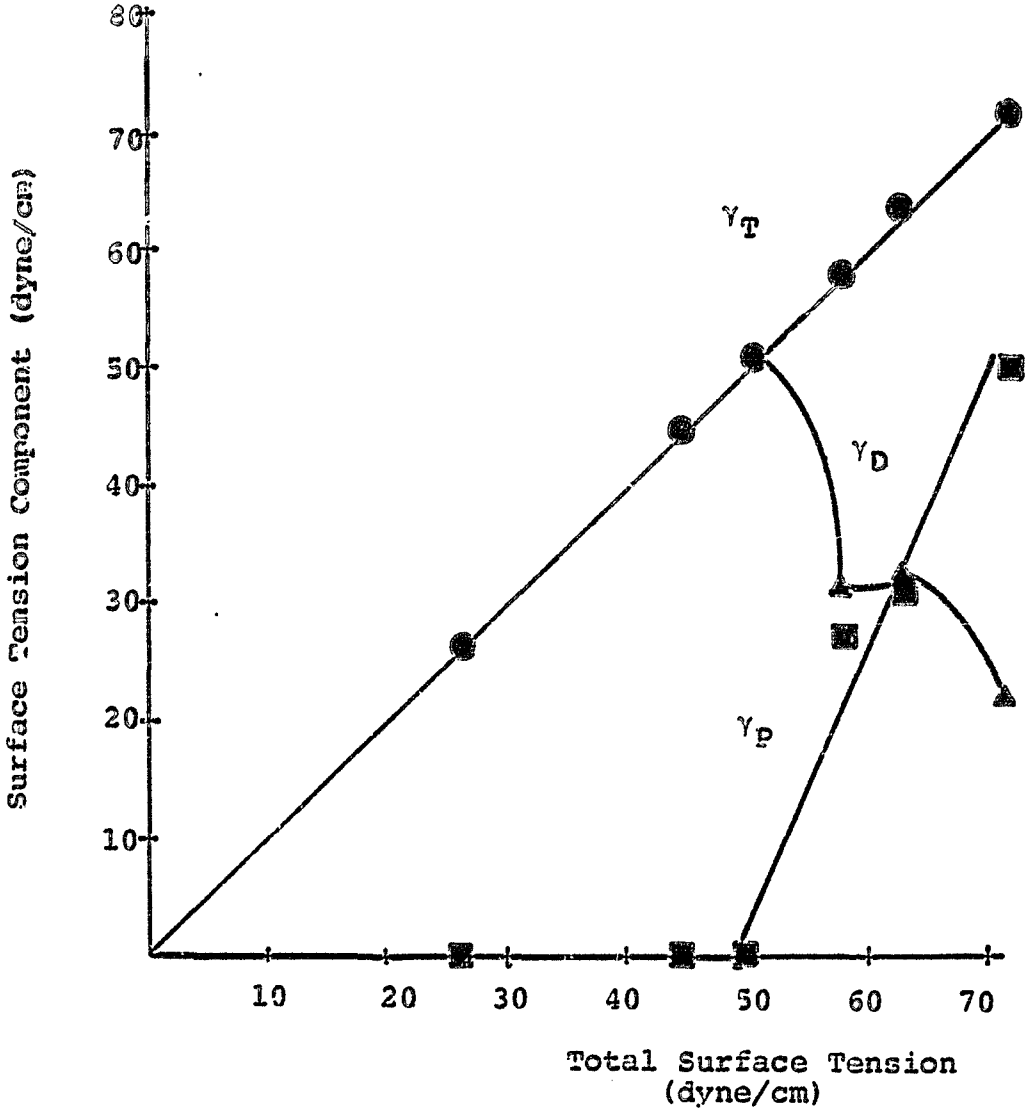

Figure 31: Polar and dispersion components of Zisman series surface tensions.

methylene iodide were due to the dispersion component alone. However, for formamide and glycerol, there is an almost even distribution of the two forces. Finally, the polar component dominates the surface tension of water.

It was reported by Legin (37) that aqueous alcohol solutions show preferential adsorption of alcohols on paraffin. As evidence for preferential adsorption, a plot of the contact angle of the solution versus the concentration of alcohol was made. The graph for ethanol is shown in Figure 32. The curve has a point of inflection in the region where the alcohol made up 30% of the solution. The effect was ascribed to the stratification of the solution at the liquid/paraffin interface.

This same plot was made for the results obtained in this study and is shown in Figure 33. Contrary to what Legin claimed, the curve was a smooth one. Indeed, if a point of inflection is the evidence for preferential adsorption, then it is not present in the system used here.

Figure 34 is a plot that shows the dependence of γ_1^p on the concentration of ethanol. There is a sharp decrease in the polar component when alcohol concentrations goes from zero to about 35 mole percent. This is expected since water, which is very polar, makes up the majority of the solution. However, from 35% to 83%, the polar contribution

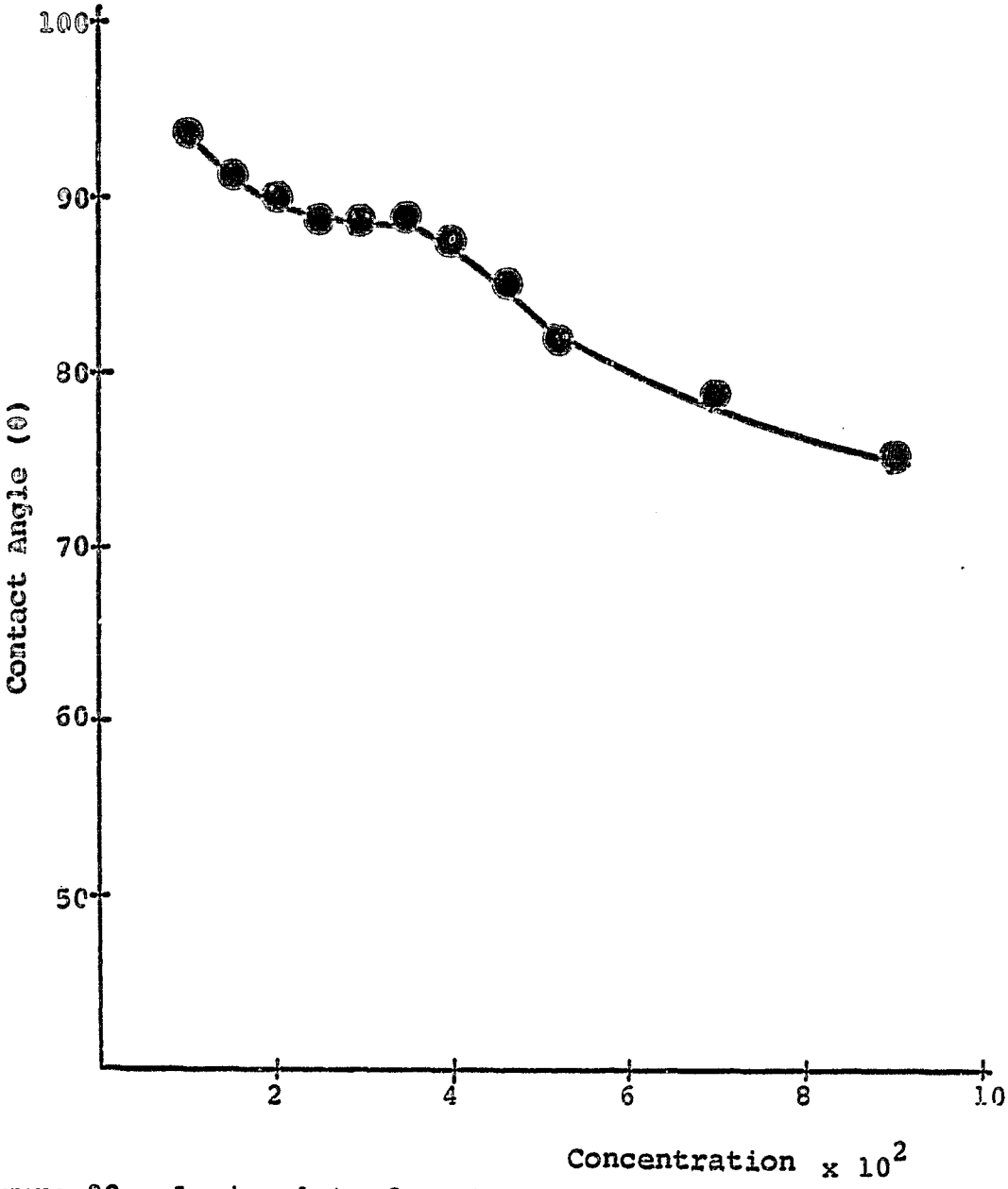

Figure 32: Legin plot of contact angle of aqueous ethanol solutions on paraffin.

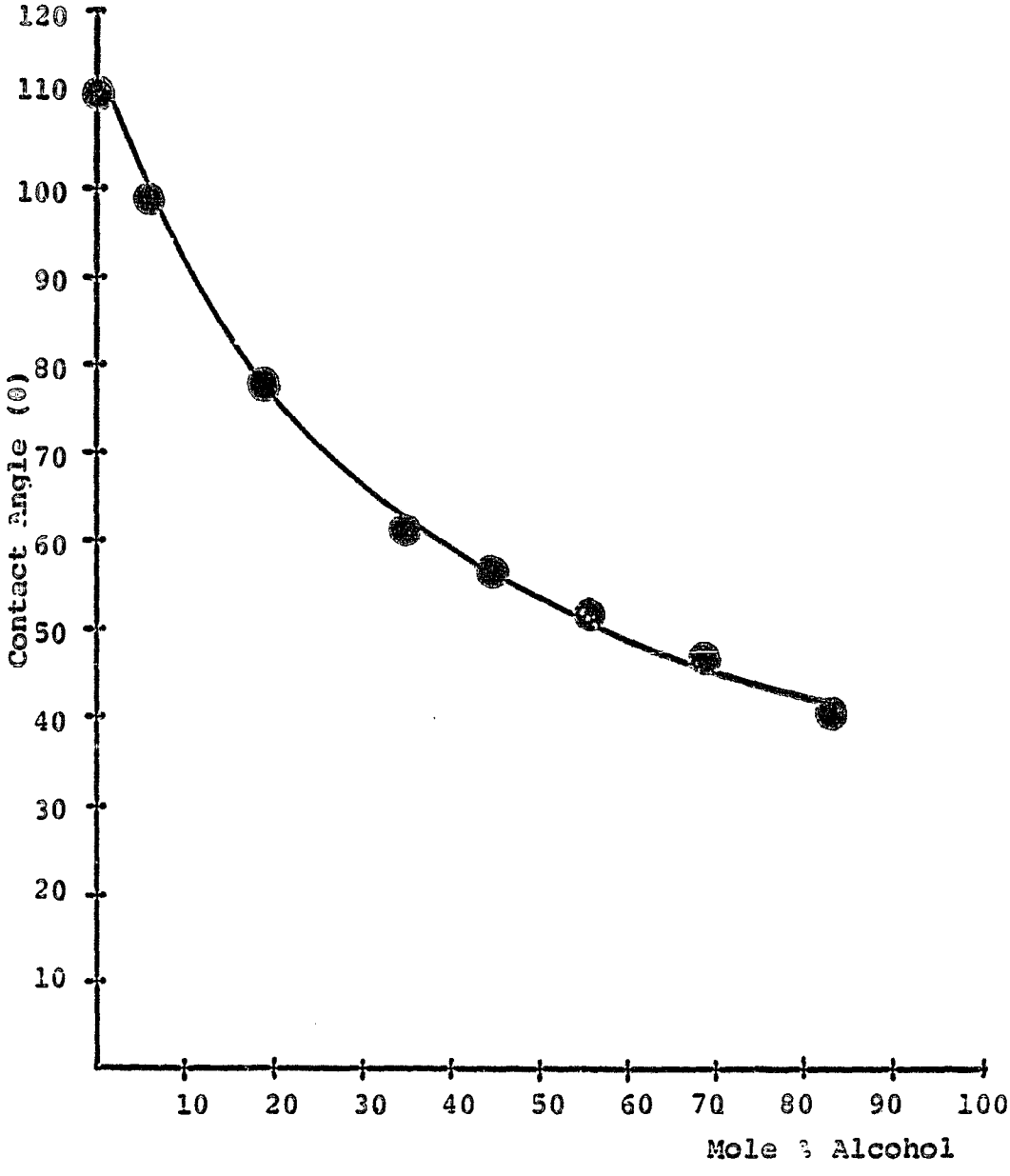

Figure 33: Plot of contact angles of aqueous ethanol solutions on paraffin for this study.

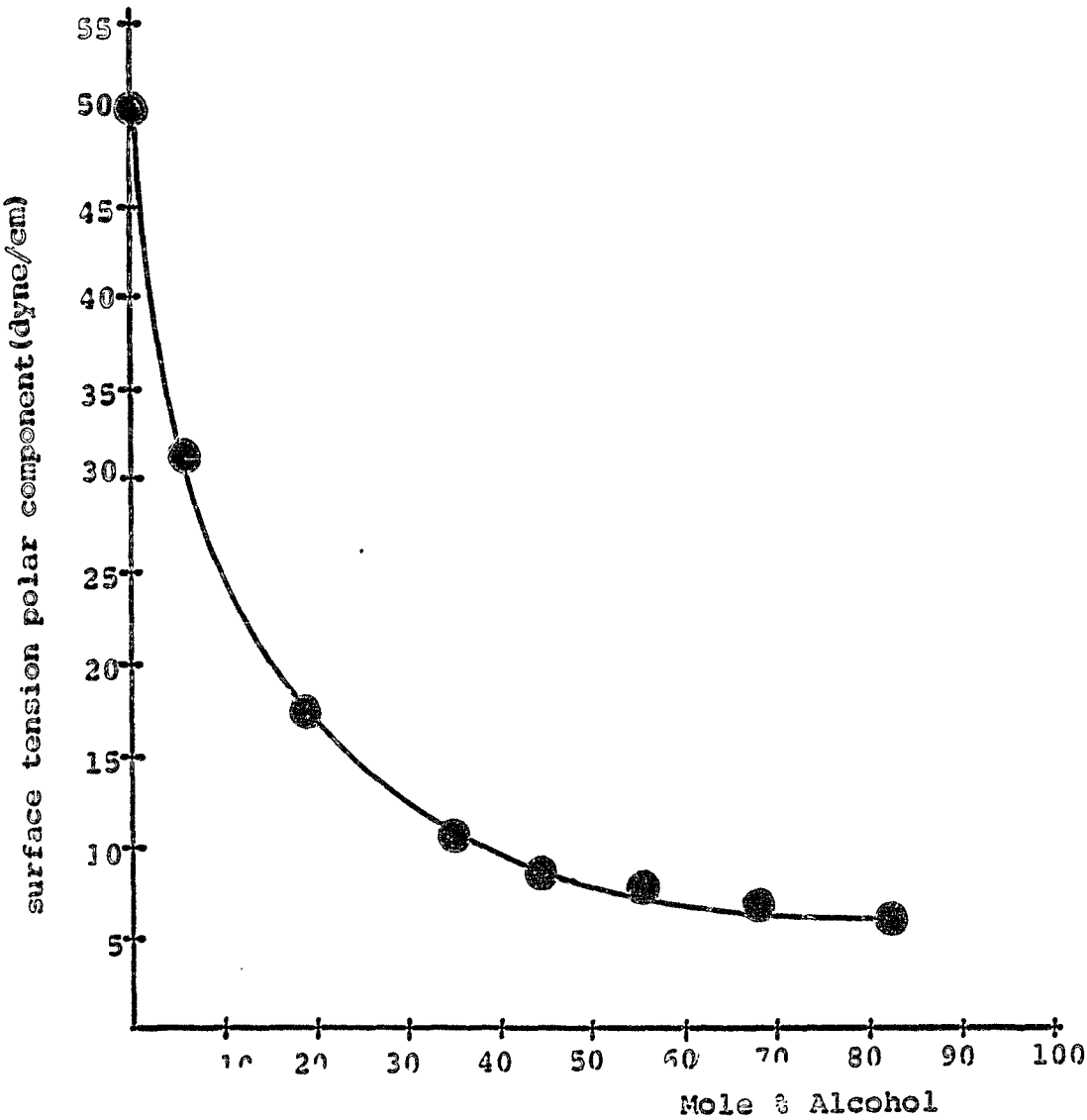

Figure 34: Plot of surface tension polar component versus alcohol concentration.

remains relatively constant. This behavior may be due to the alcohol molecules tying the water molecules up in hydrogen bonding, thus allowing the hydrophobic part of the alcohol to enhance the surface of the solution (48). If hydrogen bonding is present, it would reduce the actual polarity of the solvent and is stronger evidence for preferential adsorption as opposed to that proposed by Legin (37).

4.3 SOLID SURFACE ENERGY DETERMINATION

The critical surface tensions of the polymers used were determined by the empirical method first reported by Zisman. The contact angles for polymers obtained with the aqueous ethanol solutions and the Zisman series are shown in Tables 11 and 12 respectively. The Zisman plots ($\cos\theta$ versus γ_l) are shown in Figures 35 and 36. The plots show greater curvature for the more polar liquids than for the non-polar liquids, as was observed by Zisman (32). The γ_c values obtained upon extrapolation of the Zisman plot are shown in Table 13. There is fairly good agreement between experimental values and those reported in the literature. A comparison of the numbers obtained for γ_c shows that for very low energy surfaces such as Nyebar and teflon, the liquid series used does not affect γ_c significantly. For

TABLE 11

Advancing Contact Angles of Aqueous Ethanol Solutions on Polymers

Liquid	γ_l (dynes/cm)	Nyebar	Teflon	Polysulfone	Polymethylmethacrylate
Water	72.0	122.4	119.7	86.6	75.3
10/90	50.5	112.3	104.9	81.2	64.2
30/70	36.5	96.4	90.8	68.6	55.8
50/50	31.2	87.3	74.2	53.1	28.5
60/40	29.5	82.6	68.9	49.7	spreads
70/30	28.1	80.2	65.6	17.6	spreads
80/20	26.7	77.4	60.9	17.0	spreads
90/10	25.2	73.5	58.0	spreads	spreads
99.6/0	22.4	66.3	43.3	spreads	spreads

TABLE 12

Advancing Contact Angles of Zisman Series on Polymers

Liquid	γ_l (dynes/cm)	Nyebar	Teflon	PSF	PMMA	Control
Water	72.0	122.4	119.7	86.6	75.3	78.5
Glycerol	63.4	113.0	103.0	74.2	66.5	77.5
Formamide	58.2	108.5	100.6	67.4	57.1	70.8
Methylene Iodide	50.6	99.9	92.9	30.3	37.8	66.4
1-Bromonaphthalene	44.6	92.4	76.3	28.2	12.6	38.9
Hexadecane	26.5	74.9	45.0	spreads	spreads	4.8
Decane	23.8	69.0	35.8	--	--	spreads
Octane	21.6	62.0	27.6	--	--	--
Hexane	18.3	52.1	12.1	--	--	--

ORIGINAL PAGE IS
OF POOR QUALITY

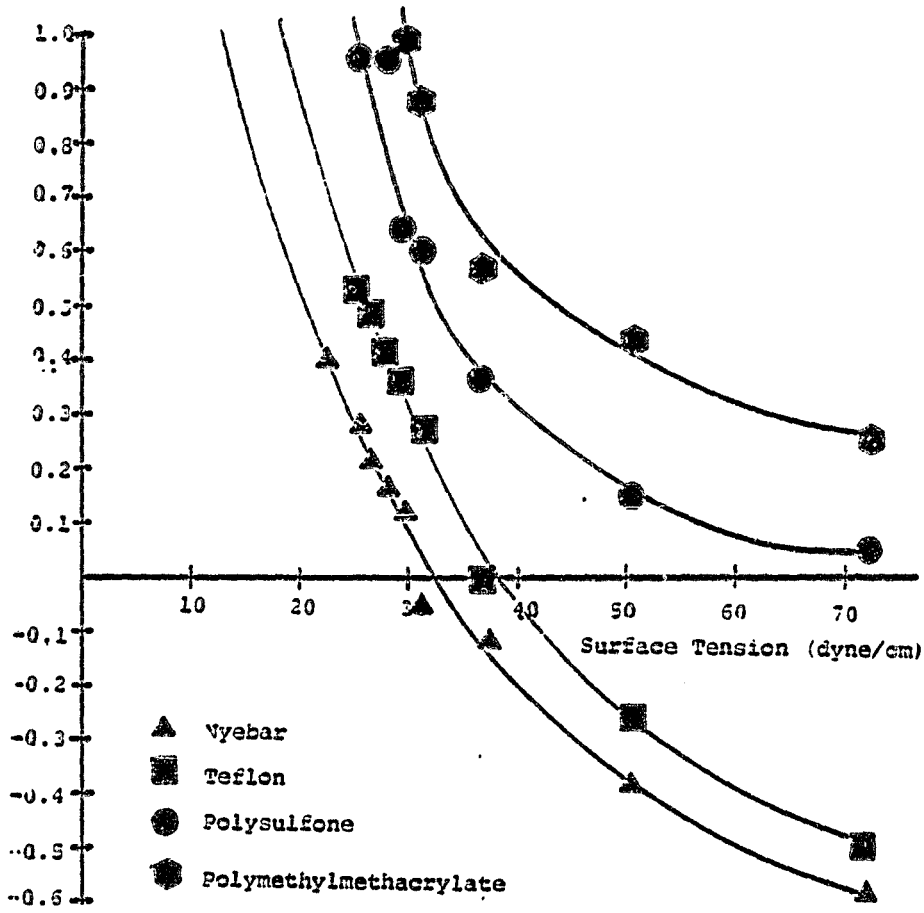

Figure 35: Zisman plot of aqueous ethanol solutions.

ORIGINAL PAGE IS
OF POOR QUALITY

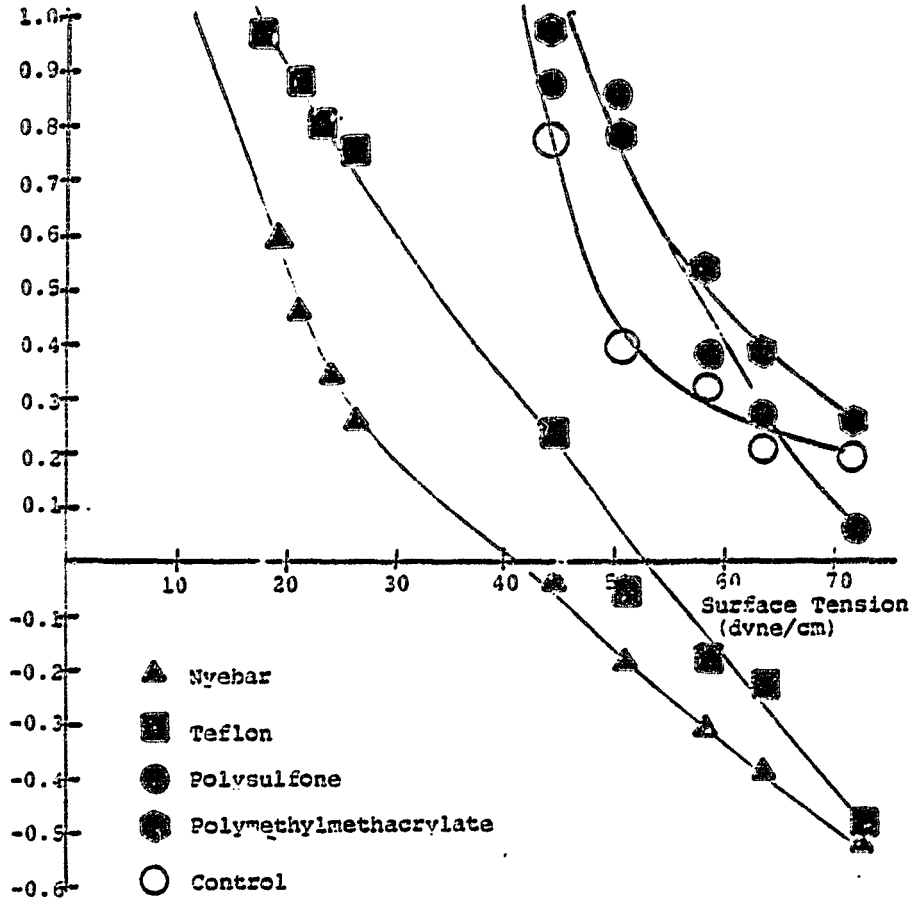

Figure 36: Zisman plot of Zisman series.

TABLE 13

Critical Surface Tensions

Polymers	γ_c* (dynes/cm)	γ_c** (dynes/cm)	γ_c+ (dynes/cm)	γ_c++ (dynes/cm)
Nyebar	12.5	11†	11.5	--
Teflon	18.5	19	18.0	18.5
PSF	25.5	--	45.0	41††
PMMA	31.5	26.5	46.0	39
Control	--	--	41.5	--

* Determined with the ethanol solutions

** Reference 54

\+ Determined with the Zisman series

++ Reference 19

† Reference 129

†† Reference 130

the higher energy polymer surfaces however, the values of γ_c obtained were dependent on the liquid used, with the aqueous ethanol solutions yielding lower numbers than those of the Zisman series. The critical surface tension of clean aluminum is much higher than that of polymer surfaces. This being so, all liquids should wet it. The fact that a finite contact angle was observed suggests hydrocarbon contamination is present on the metal surface.

The structures of Nyebar and PMMA (see Figure 14) are similar. The two have the same backbone, however, the difference is that the ester R group for Nyebar is a long fluorocarbon chain, while that for PMMA is a methyl group. If Zisman's wettability spectrum (see Figure 4) is valid, the critical surface tension obtained for Nyebar would indicate a surface with a mixture of CF_3 and CF_2 groups. This would mean that the fluorocarbon chain lies on the surface, but none of the polar backbone makes a contribution to the surface energy. For PMMA, the γ_c obtained is much higher than what it would be if only methyl groups were present on the surface. This would indicate that there is some polar contribution from the ester group on the surface. The difference in the structures of the two polymers can be seen more clearly in Figure 37, which represent possible surface conformations.

ORIGINAL PAGE
COLOR PHOTOGRAPH

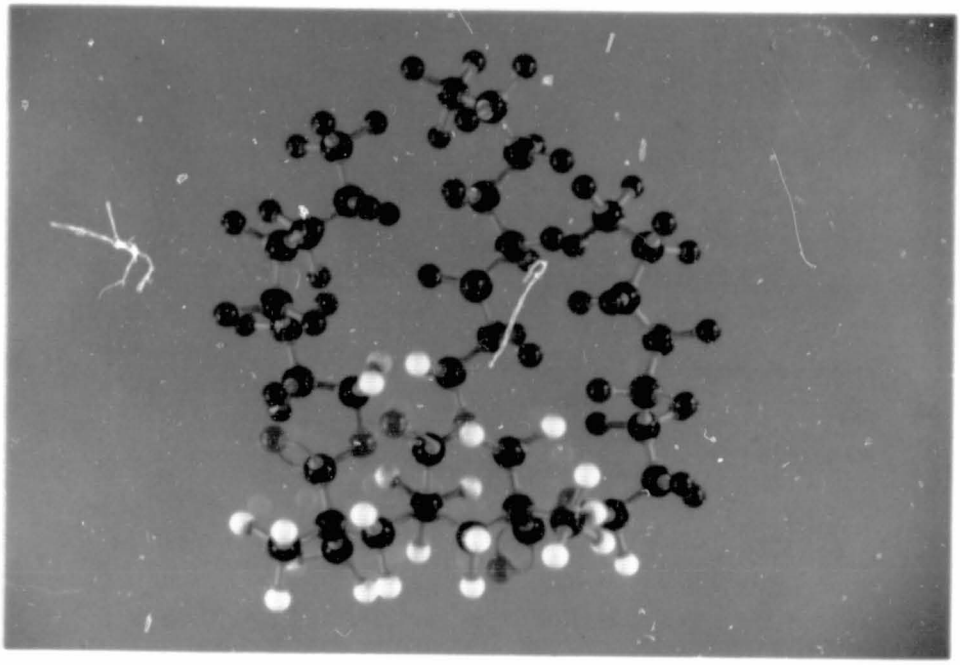

(a)

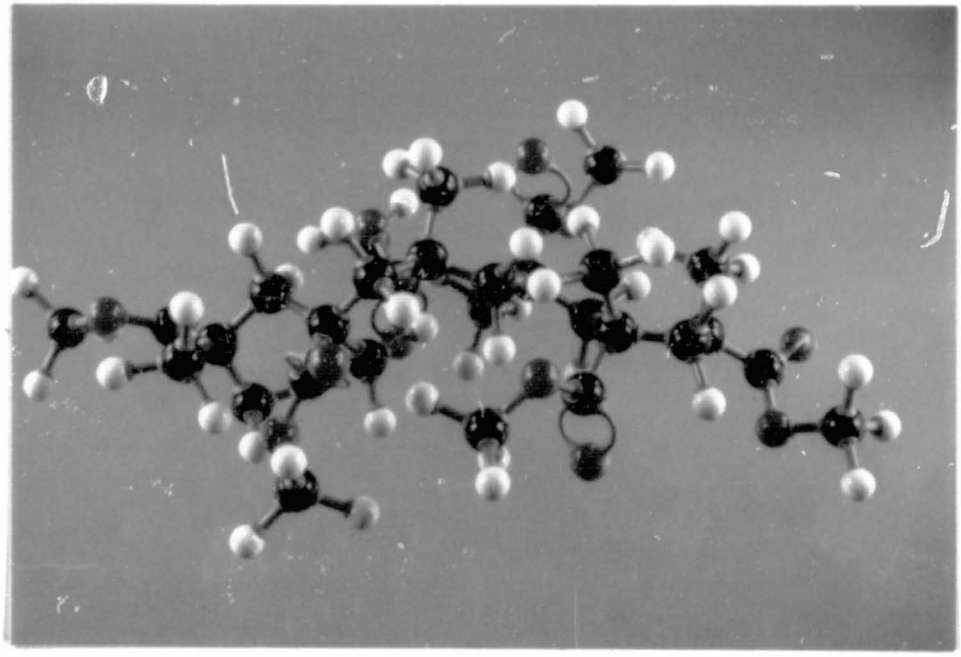

(b)

Figure 37: (a) Nyebar and (b) PMMA molecular models.

A model of Nyebar is seen in Figure 37 a, where the green balls represent fluorine in the fluorocarbon chain. CF_2 and CF_3 groups are seen to dominate the surface. For PMMA (Figure 37 b), there is a mixture of white balls (hydrogens from the methyl groups) and red balls (oxygens from the ester group). The value of γ_c calculated for teflon (18 dynes per cm), is close to that reported for CF_2 groups on the surface. The value of γ_c for PSF is slightly higher than would be indicated if only phenyl rings appear on the surface. This indicates a slight contribution from the ether oxygen which would impart a polar character to the surface, thus raising the γ_c.

4.3.1 ESCA Take-off Angle Study

ESCA take-off angle studies were conducted to support the surface composition predictions made from critical surface tension results. The premise here is that the electron take-off angle can be varied to make the technique more surface sensitive. The smaller the take-off angle, the fewer total electrons are collected. However, these electrons come from the top few angstroms of the solid surface. Results of the study are shown in Table 14. The fluorine to carbon ratio for Nyebar would have been expected to increase as the take-off angle was decreased from 90° to

TABLE 14

ESCA Take-off Angle Dependence Study Elemental Ratios

Sample	Angle (°)	Elemental Ratios		
		O/C	F/C	S/C
Nyebar	10	0.21	0.53	--
	30	0.14	0.71	--
	90	0.15	0.83	--
Teflon	10	0.050	1.1	--
	30	0.040	1.2	--
	90	0.035	1.2	--
Polysulfone	10	0.20	--	0.018
	30	0.15	--	0.029
	90	0.15	--	0.034
Polymethylmethacrylate	10	0.30	--	--
	30	0.28	--	--
	90	0.31	--	--

10^{o}. However, the reverse is seen, with 90^{o} having the highest ratio. Furthermore, if the surface consists predominantly of CF_2 and CF_3 groups, this should yield an F/C ratio of 2.0 at 10^{o}. The observed ratio is 75% lower than the expected value.

For teflon, the F/C ratio remained constant since CF_2 is the only group present in the molecule. Again, the stoichiometric ratio of 2.0 for F/C was greater than the calculated ratio of 1.1.

For polysulfone, the S/C ratio increased as the take-off angle was increased, indicating that the sulfone group was not predominant on the surface. The high energy of the surface is then due to the presence of ether oxygen on the polysulfone surface.

4.3.2 Surface Heterogeneity

All γ_c results were obtained using the advancing contact angle (θ_a). Receding contact angles (θ_r) have been used to give an indication of surface homogeneity. If $\theta_a = \theta_r$, then the surface is assumed to be homogeneous. For the surfaces studied, the films were not of uniform thickness as evidenced by the interference patterns. Indeed this was confirmed when receding angles were measured because whereas the advancing angles were quite reproducible, the receding

angles were not. This disparity would indicate that the surface is generally low energy with high energy patches (128). As the liquid drop recedes from the surface, it is in effect going over areas of varying thicknesses which are the high energy patches.

4.3.3 The Meaning of Critical Surface Tension

By using the Good-Girifalco-Fowkes-Young (GGFY) equation given by :

$$\sqrt{\gamma_s^d} = [\gamma_l(1 + \cos\theta)]/2\sqrt{\gamma_l^d} \qquad [4\text{-}3]$$

the contact angle from one liquid may be used to determine the dispersion component of the solid surface energy. These results are given in Tables 15 and 16 for the ethanol solutions and the Zisman series respectively. Comparing the γ_s^d values with those of γ_c in Table 13 shows that for the low energy surfaces γ_c is actually γ_s^d. This is confirmed by looking at the values of γ_s^d obtained with the alkanes, where $\gamma_c = \gamma_s^d$.

Use of polar liquids may give anomalous results as seen by the lower γ_s^d obtained with water. Liquids that may attack the surface, such as methylene iodide and formamide give anomalous results as well. For the high energy surfaces, values obtained for the more polar liquids such as water, glycerol, formamide and 10/90 ethanol/water give values of γ_s^d that are higher than those determined by the

TABLE 15

Values of γ_s^d for Aqueous Ethanol Solutions

Calculated Using GGFY Equation

Ethanol Series	γ_s^d Nyebar	γ_s^d Teflon	γ_s^d PSF	γ_s^d PMMA
Water	13.0	15.4	67.6	94.8
10/90	14.0	20.0	48.2	74.6
30/70	13.8	17.0	32.5	42.5
50/50	12.9	19.0	30.1	41.5
60/40	13.5	19.5	28.6	--
70/30	13.4	19.5	37.3	--
80/20	13.4	19.9	34.4	--
90/10	13.6	19.4	--	--

TABLE 16

Values of γ_s^d for Zisman Series Calculated Using GGFY Equation

Liquid	γ_s^d Nyebar	γ_s^d Teflon	γ_s^d PSP	γ_s^d PMMA
Water	13.0	15.4	67.6	94.8
Glycerol	11.4	18.5	49.9	60.3
Formamide	12.7	18.2	52.3	65.0
Methylene Iodide	8.7	11.4	43.9	40.5
1-Bromonaphthalene	10.1	16.7	39.0	43.0
Hexadecane	11.0	21.5	--	--
Decane	11.0	19.5	--	--
Octane	11.6	19.2	--	--
Hexane	11.9	17.9	--	--

purely non-polar hydrocarbons. This is a result of the polar component of the liquid interacting with that of the solid. Since the GGFY equation does not provide for this possibility, the interaction was lumped together with that of the non-polar contribution so that the dispersion component calculated turns out to be much larger than it should be. This shows that the GGFY equation is not suitable for use with polar liquids on polar solids, although Dann found it to be valid in the limit that the polar component of the liquid is less than nine dynes per cm (54).

To determine the polar components of the solids being studied, the values of γ_s^d previously calculated for the two liquid series, except for the ones with large polar contributions (water, glycerol, formamide, 10/90 ethanol/water), were averaged and used in the Tamai, Makuuchi, Suzuki (TMS) equation

$$I_{sl}^p = (\cos\theta + 1)\gamma_l - 2\sqrt{\gamma_l^d \gamma_s^d} \qquad [4\text{-}4]$$

The average values of γ_s^d calculated for the ethanol solutions and the Zisman series are shown in Tables 17 and 18 respectively. The results for I_{sl}^p are shown in Tables 19 and 20 for the ethanol solutions and the Zisman series respectively.

TABLE 17

Average Values of γ_s^d for Polymers from Aqueous Ethanol Solutions

Sample	γ_s^d (dynes/cm)
Nyebar	13.4
Teflon	19.0
Polysulfone	32.6
Polymethylmethacrylate	42.6

TABLE 18

Average Values of γ_s^d for Polymers from Zisman Series

Sample	γ_s^d (dynes/cm)
Nyebar	10.7
Teflon	17.7
Polysulfone	41.4
Polymethylmethacrylate	41.8

TABLE 19

Average Values of I^p_{sl} for Polymers from Aqueous Ethanol Solutions

Solutions	I^p_{sl} Nyebar	I^p_{sl} Teflon	I^p_{sl} PSF	I^p_{sl} PMMA
Water	-0.54	-4.1	23.3	30.2
10/90	0.65	0.95	10.3	18.1
30/70	0.45	-2.1	-0.083	0.37
50/50	-0.64	0.023	-2.1	-0.35
60/40	0.077	0.55	-3.2	--
70/30	-0.028	0.52	3.6	--
80/20	-0.057	0.88	1.4	--
90/10	0.28	0.36	--	--

I^p_{sl} in dynes/cm

TABLE 20

Average Values of I^p_{sl} for Polymers from Zisman Series

Liquid	I^p_{sl} Nyebar	I^p_{sl} Teflon	I^p_{sl} PSF	I^p_{sl} PMMA
Water	3.1	-2.7	16.6	30.3
Glycerol	1.3	1.1	7.2	14.9
Formamide	2.7	-0.18	7.6	16.5
Methylene Iodide	-4.6	-11.8	2.7	-1.4
1-Bromonaphthalene	-0.96	-1.0	-3.0	2.3
Hexadecane	-0.26	3.5	--	--
Decane	0.43	2.1	--	--
Octane	1.3	1.6	--	--
Hexane	1.5	0.11	--	--

I^p_{sl} in dynes/cm

As can be seen in Table 19, Nyebar and teflon have negligible polar contribution at the surface, as evidenced by the fact that if the following equation holds

$$\gamma_s = \gamma_s^d + \gamma_s^p \qquad [4\text{-}5]$$

a polar component that makes up <5% of the total surface energy is considered negligible (123). For the higher energy surfaces, the polar liquids water and 10/90 ethanol/water show significant polar contribution, i.e., the polar component was at least 20% of the total surface energy. This shows that the more polar the liquid, the more likely it is to interact with the polar component in the solid surface. Compared to these two liquids, the rest of the liquids showed no significant polar contributions.

A comparison with the results that Dann obtained (55) shows that for teflon, the results are different. Dann obtained $I_{sl}^p = 3.8$ dynes per cm for water on teflon. The result obtained in this study is negligible. This may be due to the different type of teflon used. Since no method of preparation was indicated in his paper, Dann presumably used teflon sheets, which could differ considerably in characteristics from the film used in this study (55).

The results in Table 20 show that the polar liquids have larger values of I_{sl}^p than those obtained for the ethanol

solutions. This may however be an artifact of the test liquids' attacking the polymer surface, at least in the case of glycerol and formamide on Nyebar. Except for hexadecane, calculated values of I^p_{sl} for teflon are generally negligible. Dann suggested that the negative I^p_{sl} values may be due to a significant spreading pressure, although this was not confirmed in the work (55). For PSF, the general trend is decreasing I^p_{sl} with decreasing liquid polarity. For PMMA, the same trend is observed. Dann obtained an I^p_{sl} of 32.3 dynes per cm for PMMA which agrees reasonably well with the corresponding value of 30.3 dynes per cm in this study. A comparison cannot be made with the results of Tamai et al. (50) because water saturated hydrocarbons were used in their studies. The pure hydrocarbons simply spread on surfaces such as PSF and PMMA.

A popular theory that also incorporates a polar contribution is that of Owens and Wendt (51) which states that

$$\cos\theta + 1 = 2\sqrt{\gamma^d_s \gamma^d_l}/\gamma_{lv} + 2\sqrt{\gamma^h_s \gamma^h_l}/\gamma_{lv} \qquad [4\text{-}6]$$

Simultaneous equations have to be solved for contact angles of two liquids. Water and methylene iodide were chosen by the authors, therefore, these liquids were used here so that

a comparison can be made with literature values. The results are shown in Table 21.

The value of γ_s for Nyebar is approximately the same as that of the γ_c. This should be expected since interaction with Nyebar is mostly through dispersion forces and γ_c was shown to be equal to γ_s^d. The γ_s obtained for teflon is much lower than γ_c, which should not be the case. This may be due to a difference in the type of teflon used or to attack of the surface by methylene iodide. The value of γ_s and γ_c for the two higher energy surfaces appear reasonable, with the values of γ_c very close to the values of γ_s^d.

The results above show that the critical surface tension obtained with the use of non-polar hydrocarbons is equal to the dispersion component of the solid surface energy. Two methods, the Tamai, Makuuchi, Suzuki and the Owens and Wendt methods were used to determine the non-dispersion component of the solid surface energy. The results do not match and demonstrates the need for continuing study in this area to bring the the level of understanding of the role of non-dispersion interactions across solid/liquid interfaces to the same level as that which now exists for dispersion interactions.

TABLE 21

Values of γ_s^d and γ_s^h from Owens and Wendt Method

Sample	γ_s^d	γ_s^h	γ_s	γ_c
Nyebar	8.6	0.66	9.3	11*
Teflon	11.4	0.12	11.5	18.5**
Polysulfone	43.4	3.8	47.2	41+
Polymethylmethacrylate	38.3	2.9	41.2	39**

γ in dynes/cm

* Reference 129

** Reference 19

\+ Reference 130

4.3.4 Surface Roughness

To examine the effect of surface roughness on contact angles, water contact angles were measured on aluminum at the four roughness levels and on the polymer coated roughened samples. The results are shown in Table 22. In most cases, the advancing angle came to a constant value, showing the insensitivity of this parameter to high energy irregularities on the surface. The advancing angles also tended to have less scatter, except for the case of bare aluminum. This may be a response to the heterogeneous chemical composition on the aluminum surface where neither the oxide layer nor the extent and kind of hydrocarbon contamination is identified. For some polymer samples, the receding angle would stay constant for two or three readings. In these cases, these values were listed as θ_r. Generally however, the values would constantly change. In these cases, an average value of the closest consecutive numbers were used.

A measure of roughness commonly used is hysteresis as defined in the equation

$$H = \theta_a - \theta_r \qquad [4\text{-}7]$$

The larger the value of H, the rougher or more heterogeneous the surface is supposed to be. Therefore, in the surfaces studied, the value of H should increase as the roughness

TABLE 22

Water Contact Angles on Rough Samples

Sample	Roughness	θ_a (°)	θ_r (°)	H (°)
Nyebar	0.2	121.7 ± 0.6	68.7 ± 4.2	53
	0.5	124.5 ± 0.6	89.0 ± 3.5	35.5
	0.9	118.0 ± 0	75.9 ± 1.6	42.1
	1.3	122.7 ± 0.6	83.6 ± 5.5	39.1
Teflon	0.2	130.0 ± 1.6	95.7 ± 2.8	34.3
	0.5	130.0 ± 2.6	109.0 ± 16.6	21.0
	0.9	128.5 ± 1.5	96.6 ± 3.9	31.9
	1.3	130.7 ± 1.2	97.5 ± 2.2	33.2
PSF	0.2	87.7 ± 0.9	63.4 ± 0.6	24.3
	0.5	79.6 ± 0.7	53.5 ± 1.3	26.1
	0.9	86.1 ± 1.1	57.0 ± 4.3	29.1
	1.3	77.7 ± 1.0	49.8 ± 0.7	27.9
PMMA	0.2	72.4 ± 0.7	60.6 ± 1.4	11.8
	0.5	70.2 ± 1.2	57.6 ± 0.1	12.6
	0.9	72.8 ± 0.6	56.8 ± 1.6	16.0
	1.3	71.0 ± 0.2	50.5 ± 1.2	20.5
Control	0.2	73.6 ± 3.6	53.2 ± 4.6	20.4
	0.5	69.4 ± 3.3	50.0 ± 3.7	19.4
	0.9	72.4 ± 5.2	55.8 ± 3.3	16.6
	1.3	82.1 ± 0.8	58.3 ± 1.5	23.8

Roughness in μm R_a

goes from 0.2μm R_a to 1.3μm R_a. This is not the case however. PMMA seems to have the only set of data where there is clearly an increase in H as the roughness increased. The results may be the effect of the nature of the surface, where roughness is actually an average measure of the number of craters per unit area. As seen in Figures 25 and 26, the surfaces were not uniformly rough.

4.4 SURFACE CHARACTERIZATION BEFORE AND AFTER INSECT IMPACT EXPERIMENTS

4.4.1 Contact Angle Measurements

Water contact angles were measured on the samples after exposure to the insect impacts. These angles were compared to those of the unexposed samples to determine if the surface energies of the samples were severely altered by contamination during the road exposure.

4.4.1.1 Phase I

Contact angle measurements for samples before and after exposure and shown in Table 23. The results for both Nyebar and polysulfone show no significant change in surface energy before and after exposure, since the changes which were observed were within experimental error.

TABLE 23

Phase I Water Contact Angles Before and After Insect Impact Experiments

Sample	θ_a Before	θ_a After
Nyebar	122.4	119.4
Polysulfone	86.6	85.0

4.4.1.2 Phase II

The contact angle measurement results are shown in Table 24. The results indicate that for Nyebar, PSF and PMMA, exposure on the road did not significantly affect the water contact angle. This is surprising considering the sensitivity of contact angles to the presence of contamination.

The contact angles on teflon increased after road exposure. One possible cause for this is physical. As seen in Figure 28, the teflon films have uncontrolled roughnesses after sintering. Since the samples were sintered at different times, it is possible that the films exposed to the road were rougher. Rougher surfaces do give higher contact angles. Another reason for the discrepancy may be chemical in nature. It is probable that the unexposed samples have residual surfactant. Exposure to the road allowed evaporation of the excess surfactant on the top few angstroms of the film surface, thus yielding higher contact angles (129). The control shows no trend in the unexposed plates. In the road tested samples however, similar contact angles were observed except for the 0.9μm R_a sample. The reproducibility of the numbers strongly suggest that there is a layer of hydrocarbon contamination present on the oxide surface. If this hydrocarbon contamination is the same for

TABLE 24

Phase II Water Contact Angles Before and After Insect Impact Experiments

Sample	Roughness	θ_a Before	θ_a After
Nyebar	0.2	121.7 ± 0.5	121.1 ± 0.4
	0.5	124.5 ± 0.6	119.0 ± 0.4
	0.9	118.0 ± 0	121.1 ± 0.8
	1.3	122.7 ± 0.6	119.3 ± 1.3
Teflon	0.2	130.0 ± 1.6	141.2 ± 4.9
	0.5	130.0 ± 2.6	137.7 ± 0.46
	0.9	128.5 ± 1.5	139.6 ± 1.5
	1.3	130.7 ± 1.2	138.7 ± 1.2
PSF	0.2	87.7 ± 0.9	87.4 ± 0.2
	0.5	79.6 ± 0.7	87.1 ± 0.3
	0.9	86.1 ± 1.1	88.1 ± 0.8
	1.3	77.7 ± 1.0	87.0 ± 0.7
PMMA	0.2	72.4 ± 0.7	74.4 ± 0.2
	0.5	70.2 ± 1.2	73.3 ± 0.8
	0.9	72.8 ± 0.6	72.5 ± 0.3
	1.3	71.0 ± 0.2	74.7 ± 1.3
Control	0.2	73.6 ± 3.6	61.5 ± 1.3
	0.5	69.4 ± 3.3	61.0 ± 1.8
	0.9	72.4 ± 5.2	81.0 ± 1.3
	1.3	82.1 ± 0.8	63.4 ± 2.5

all the plates, then the contact angles should reflect this, as the results do, since the numbers are all approximately the same value.

The results obtained above are interesting for two reasons. First, there has been no report in the literature of contact angle measurements done on samples exposed to road contamination. Second, the results show that water contact angles are only sensitive enough to pick up a lowering of surface energy due to contamination on extremely high energy surfaces such as aluminum, but not on low energy polymer surfaces.

4.4.2 ESCA

4.4.2.1 Phase I

Elemental ratios calculated from ESCA results before and after insect collection are shown in Table 25. The C/F ratio of Nyebar does not increase significantly which is consistent with the fact that since Nyebar is such a low energy surface, extensive hydrocarbon contamination is not very likely. However, the C/S ratio for PSF increased by 2.5 times, which indicates that PSF, being a higher energy surface, was more prone to hydrocarbon contamination. The water contact angle measurements were not sensitive enough to pick up this change.

TABLE 25

Phase I ESCA Elemental Ratios Before and After Insect Impact Experiments

Sample	C/O	C/F	C/S
Nyebar Before	5.8	1.7	-
Nyebar After	5.3	2.1	-
PSF Before	6.2	-	38.0
PSF After	7.3	-	101.4

The ESCA binding energies before and after road exposure for Phase I are shown in Table 26. There was no significant shift evident in the binding energies to indicate a change in the surface chemical composition. It can therefore be concluded that the road exposure did not severely alter the polymer surfaces.

4.4.2.2 Phase II

Elemental ratios from ESCA results are shown in Table 27. Nyebar and teflon both show no significant change in the C/F ratios. This is presumably due to a low surface energy which results in minimal hydrocarbon contamination. The result for teflon supports the conclusion made in the previous section that the change in contact angle was not due to a chemical composition change at the surface. Again, PSF shows a change in C/S ratio after exposure. This time however, the change is much smaller than the results obtained in Phase I. This may be due to the shorter time of exposure for this experiment. The control shows the biggest change. The C/Al ratio increased almost a hundred percent after road exposure, reflecting the high surface energy of aluminum and its high tendency to adsorb organic contamination.

TABLE 26

Phase I ESCA Binding Energies Before and After Insect Impact Experiments

Sample	C1s (eV)	O1s (eV)	F1s (eV)	S2p (eV)
Nyebar Before	284.5	533.2	689.8	-
Nyebar After	284.5	532.1	689.5	-
PSF Before	284.5	532.3	-	167.2
PSF After	284.5	532.0	-	167.6

TABLE 27

Phase II ESCA Elemental Ratios Before and After Insect Impact Experiments

Sample	C/O	C/F	C/S	C/Al
Nyebar Before	6.8	1.2	-	-
Nyebar After	7.1	1.4	-	-
Teflon Before	13.7	1.0	-	-
Teflon After	13.3	1.0	-	-
PSF Before	6.3	-	27.0	-
PSF After	6.0	-	34.0	-
PMMA Before	3.5	-	-	-
PMMA After	3.5	-	-	-
Control Before	1.2	-	-	2.6
Control After	1.2	-	-	4.3

Table 28 lists the binding energies of the photoelectron peaks before and after exposure. C1s is normalized because it is used as a reference. The O1s photopeak does not shift significantly, averaging about 532 eV, which is consistent for organically bound oxygen. F1s, S2p and Al2p all show no significant shift, indicating no change in the bonding structure of the surface atoms.

4.4.3 Specular Reflectance FT-IR

4.4.3.1 Phase I

The FT-IR spectra of Nyebar are shown in Figure 38. Peak assignments are given in Table 29. The spectrum after exposure is identical to that before exposure. Again, there is no apparent contamination of Nyebar due to an extremely low surface energy.

Figure 39 is the IR spectra of PSF before and after road exposure. Peak assignments are given in Table 30. The two spectra only differ by the presence of an extra hydrocarbon band for the exposed sample. This is due to contamination picked up during the insect impact run and confirms the ESCA results.

4.4.3.2 Phase II

TABLE 28

Phase II ESCA Binding Energies Before and After Insect Impact Experiments

Sample	C1s (eV)	O1s (eV)	F1s (eV)	S2p (eV)	Al2p (eV)
Nyebar Before	284.5	533.4	689.6	-	-
Nyebar After	284.5	535.1	690.8	-	-
Teflon Before	284.5	532.3	690.0	-	-
Teflon After	284.5	532.7	690.7	-	-
PSF Before	284.5	532.6	-	167.3	-
PSF After	284.5	531.9	-	167.5	-
PMMA Before	284.5	532.5	-	-	-
PMMA After	284.5	532.5	-	-	-
Control Before	284.5	531.3	-	-	73.9
Control After	284.5	531.7	-	-	74.1

ORIGINAL PAGE IS
OF POOR QUALITY

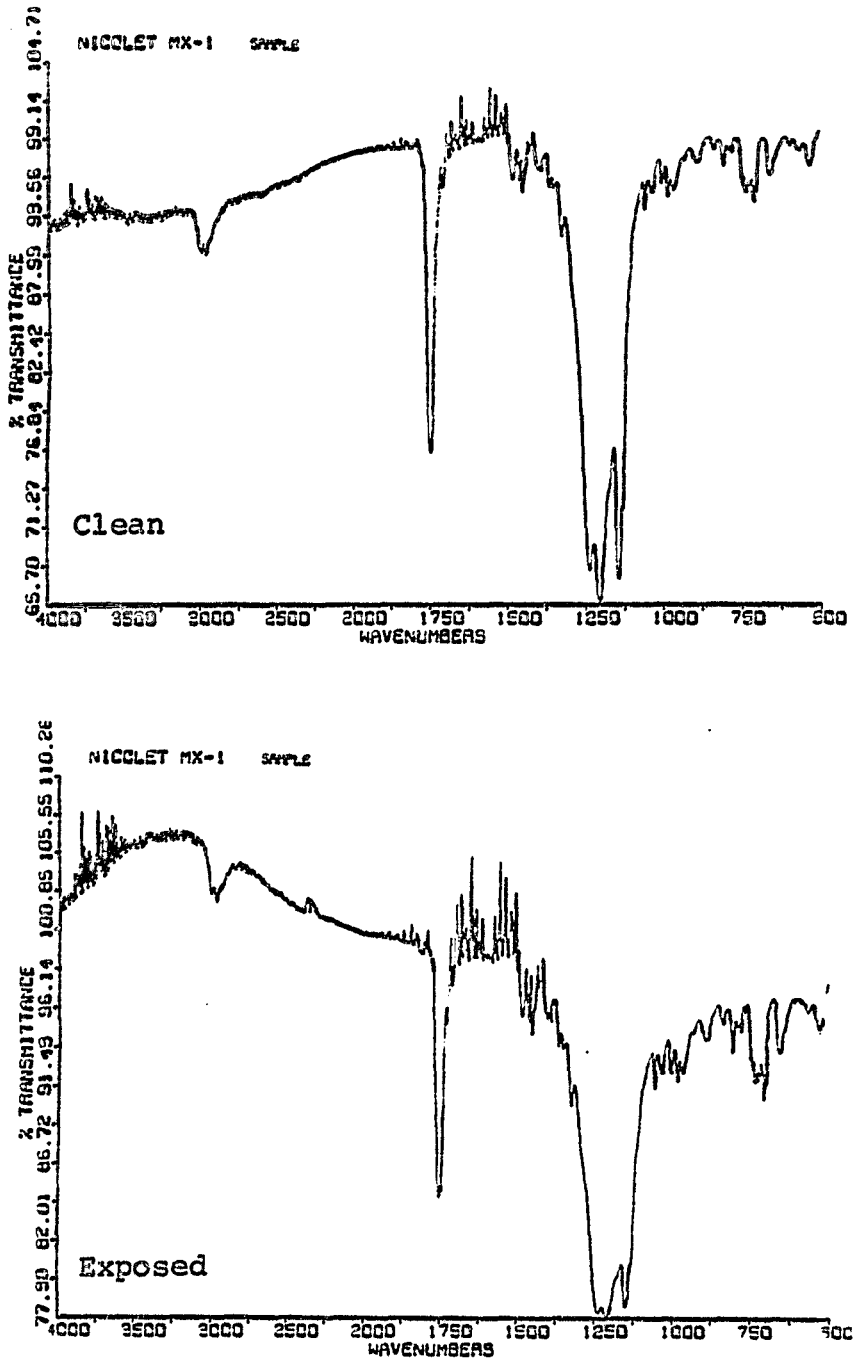

Figure 38: Phase I Nyebar FT-IR spectra before and after road exposure.

TABLE 29

Phase I Nyebar FT-IR Spectra Peak Assignment*

Wavenumbers (cm^{-1})	Peak Assignment
3000, 2998	Aliphatic C-H stretching vibration
1750	Saturated aliphatic ester stretching vibration
1238	CF_3-CF_2 stretching vibration
1206	C-F stretching vibration
1149	C-O stretching vibration

* Reference 135

ORIGINAL PAGE IS
OF POOR QUALITY

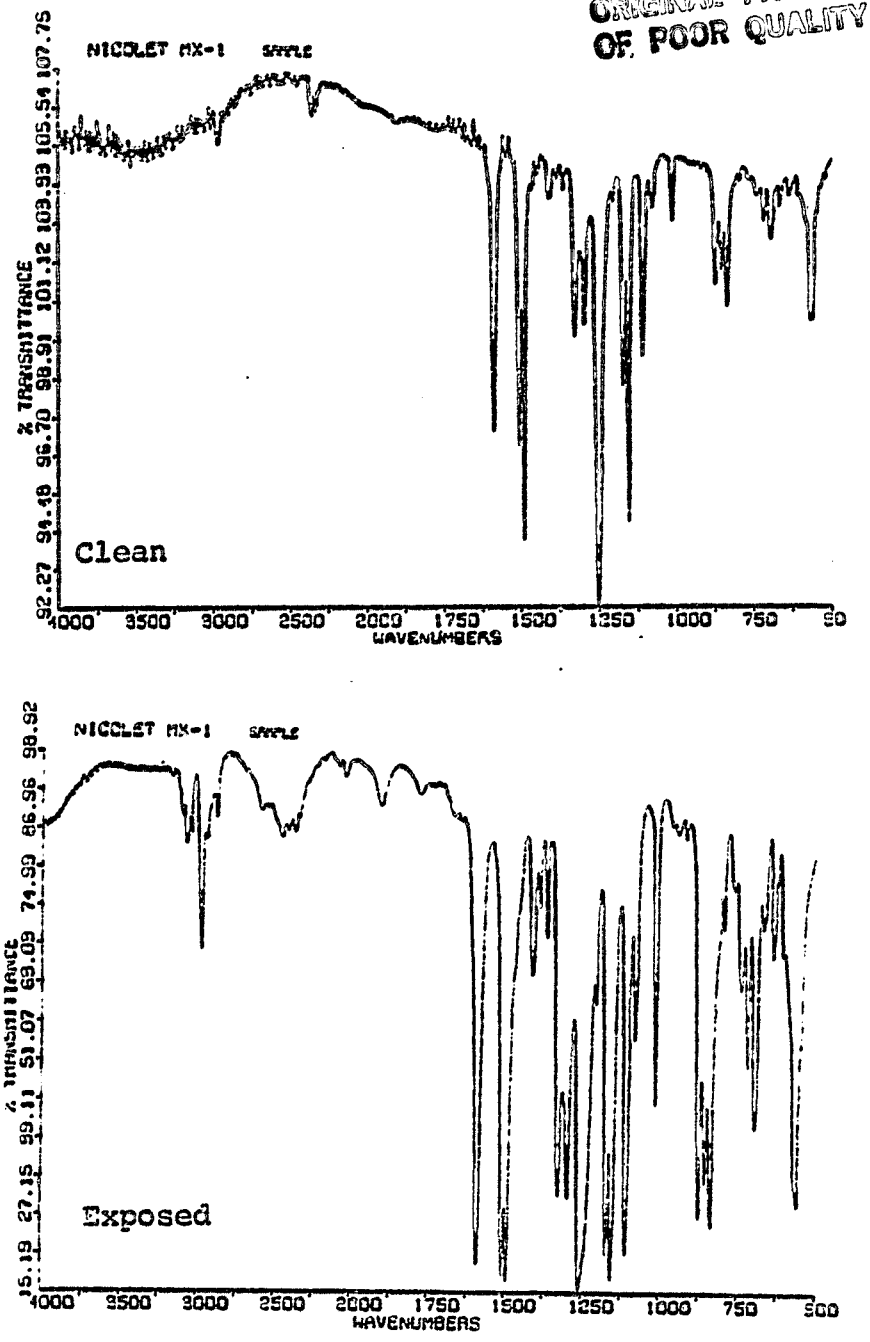

Figure 39: Phase I polysulfone FT-IR spectra before and after road exposure.

TABLE 30

Phase I Polysulfone FT-IR Spectra Peak Assignment*

Wavenumbers (cm^{-1})	Peak Assignment
3300	C-H stretching vibration
3000	Aromatic C-H stretching vibration
1590, 1510, 1490	Aromatic C=C stretching vibration
1410	Asymmetric C-H bending deformation of CH_3
1330	Asymmetric O=S=O stretching vibration
1300	Asymmetric O-S-O stretching vibration
1250	Asymmetric C-O-C stretching of aryl ether
1180	Asymmetric O=S=O stretching vibration
1150	Symmetric O=S=O stretching vibration
1080	Aromatic ring vibrations
1020	Symmetric O=S=O stretching vibration
700 - 560	C-S stretching vibrations

*Reference 136

Clean and exposed Nyebar spectra are shown in Figure 40. Peak assignments are given in Table 31. The sample examined had bug residue on it and the difference in the two spectra is due to residual amino acids left on the surface by the insect debris (130,131).

Polysulfone FT-IR spectra are shown in Figure 41. Peak assignment is identical to Table 30. There is no difference in the two samples, which supports the ESCA, as well as the contact angle results.

The FT-IR spectra for teflon and PMMA are shown in Figures 42 and 43 respectively. Corresponding peak assignments are given in Tables 32 and 33. Again, there is no significant difference in the samples before and after road exposure.

The results of specular reflectance FT-IR back up the results obtained by ESCA since both techniques showed that there was no significant change in surface composition even after exposure to the insect impact experiments. This is surprising since reflectance IR is not supposed to be a surface sensitive technique. The findings here show the promise of specular reflectance infrared spectroscopy as a surface sensitive tool, at least for very thin films.

ORIGINAL PAGE IS
OF POOR QUALITY

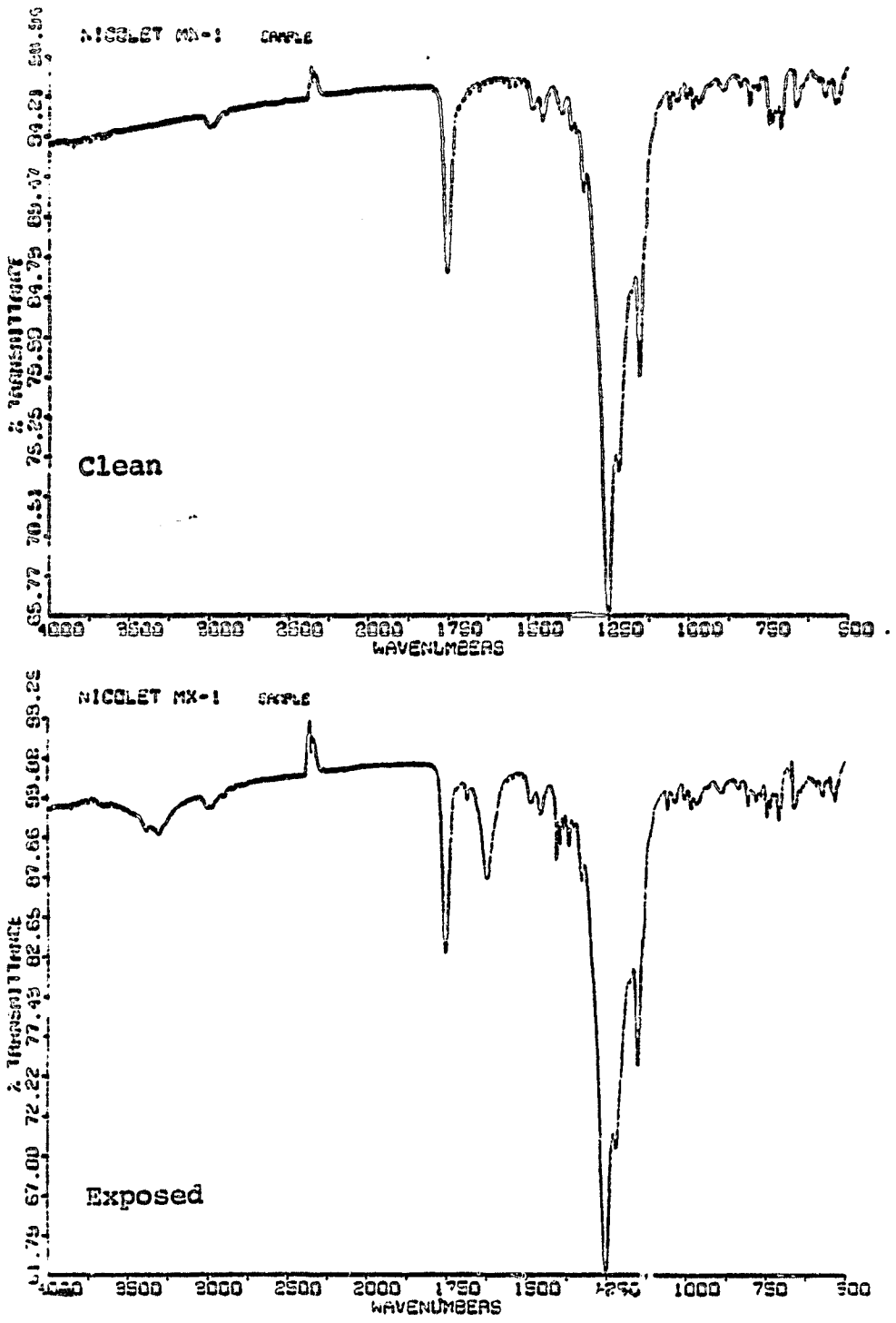

Figure 40: Phase II Nyebar FT-IR spectra before and after road exposure.

TABLE 31

Phase II Nyebar FT-IR Spectra Peak Assignment

Wavenumber (cm^{-1})	Peak Assignment
3302	Asymmetric and symmetric vibrations of $-NH_2$ from amino acid salt
1752	Saturated aliphatic ester stretching vibration
1623	Asymmetric NH_3^+ deformation
1396	Symmetric CO_2^- stretching vibration
1252	CF_3-CF_2 stretching vibration
1219	C-F stretching vibration
1154	C-O stretching vibration

* Reference 135

ORIGINAL PAGE IS
OF POOR QUALITY

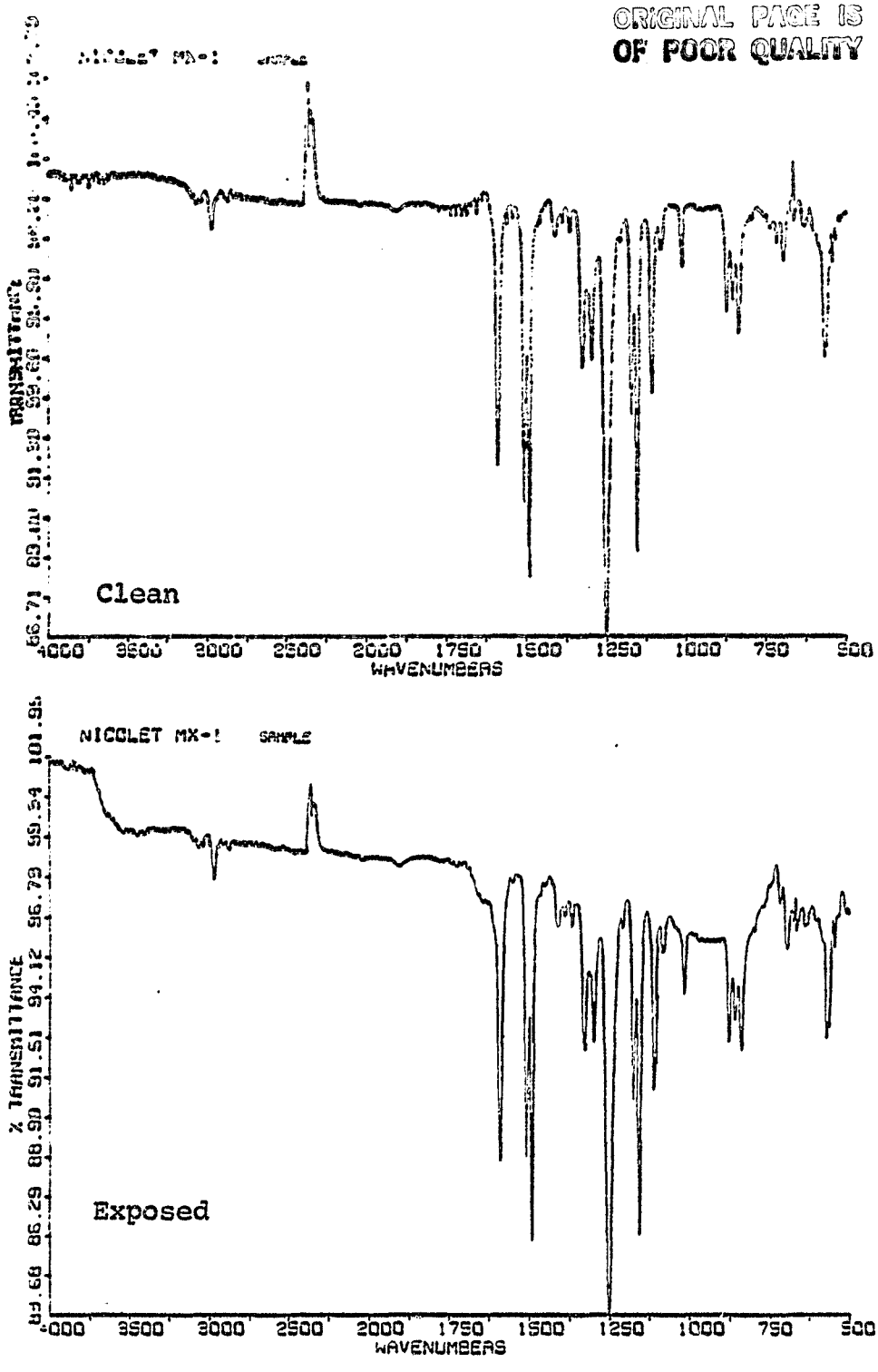

Figure 41: Phase II polysulfone FT-IR spectra before and after road exposure.

ORIGINAL PAGE IS
OF POOR QUALITY

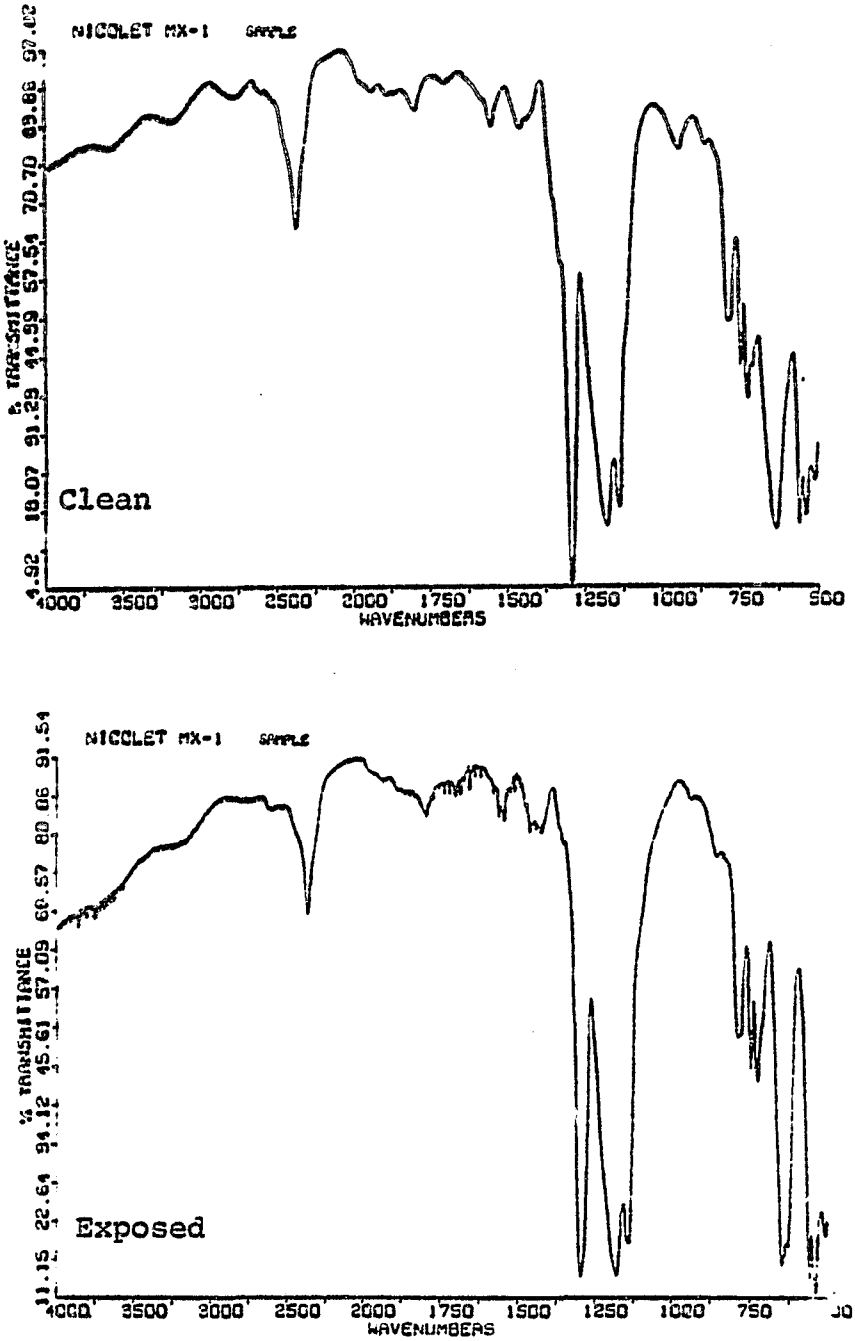

Figure 42: Phase II Teflon FT-IR spectra before and after road exposure.

ORIGINAL PAGE IS
OF POOR QUALITY

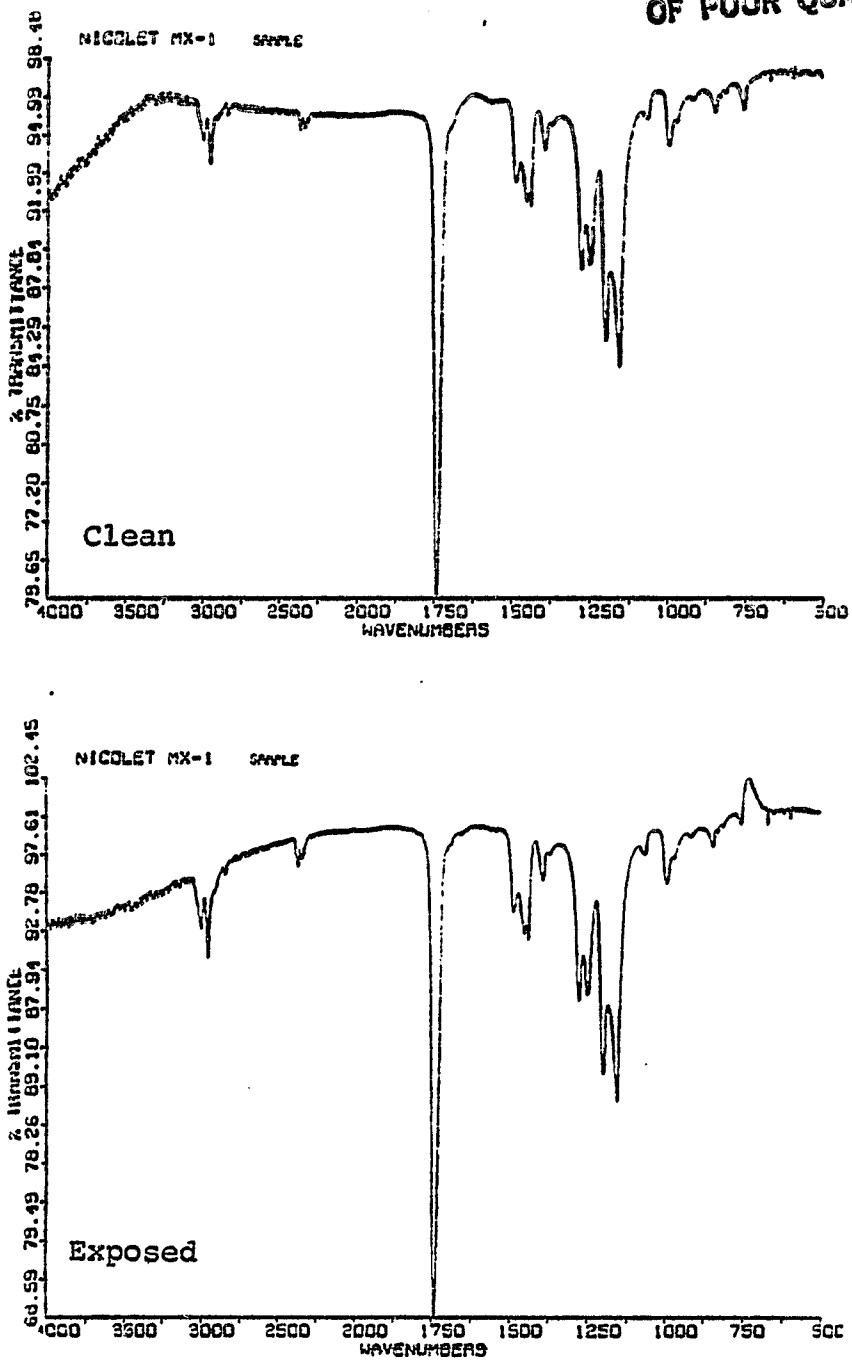

Figure 43: Phase II PMMA FT-IR spectra before and after road exposure.

TABLE 32

Teflon FT-IR Spectra Peak Assignment

Wavenumber (cm^{-1})	Peak Assignment
2970	-OH stretch from water
1290	C-F stretching vibration
1179	C-F asymmetric stretching vibration
1138	C-F symmetric stretching vibration

TABLE 33

PMMA FT-IR Spectra Peak Assignment

Wavenumber (cm^{-1})	Peak Assignment
3000	Aliphatic C-H stretching vibration
2980	Asymmetric CH_3 stretching vibration
1740	Saturated aliphatic ester stretching vibration
1450	Asymmetric CH_3 deformation
1271, 1243, 1196	Saturated aliphatic ester C-O-C asymmetric stretch
1154	C-O stretching vibration

* Reference 135

4.4.4 Scanning Electron Microscopy

SEM photomicrographs were taken to study the topography of insect residues on the test surfaces. Figure 44 is a comparison of bug excrescence on the low energy Nyebar and the high energy PSF surface. The liquid beads up on the low energy surface and spreads out on PSF. The fluid thus acts as the adhesive for the bug carcass as can be seen in Figure 45. Where the fluid forms a lens on the surface, it occupies a smaller area than spread fluid, thus reducing the possibility of residue adhesion. Further studies are required to better understand this sticking phenomenon.

Insect residues on rough surfaces are shown in Figure 46. The fluids tend to fill the craters. Since beading occurs on low energy surfaces, additional roughness is created on the surface. Spreading of fluids on rough, high energy surfaces tends to fill up the craters and smoothen the surface. The scale of the bug residue roughness is much larger than that of the substrate roughness.

4.5 CORRELATION OF SURFACE ENERGY AND SURFACE ROUGHNESS TO INSECT CONTAMINATION

4.5.1 Bug Counts

4.5.1.1 Phase I

To relate surface energy to surface fouling, bug counts were taken. These results are shown in Table 34. Densities

ORIGINAL PAGE IS
OF POOR QUALITY

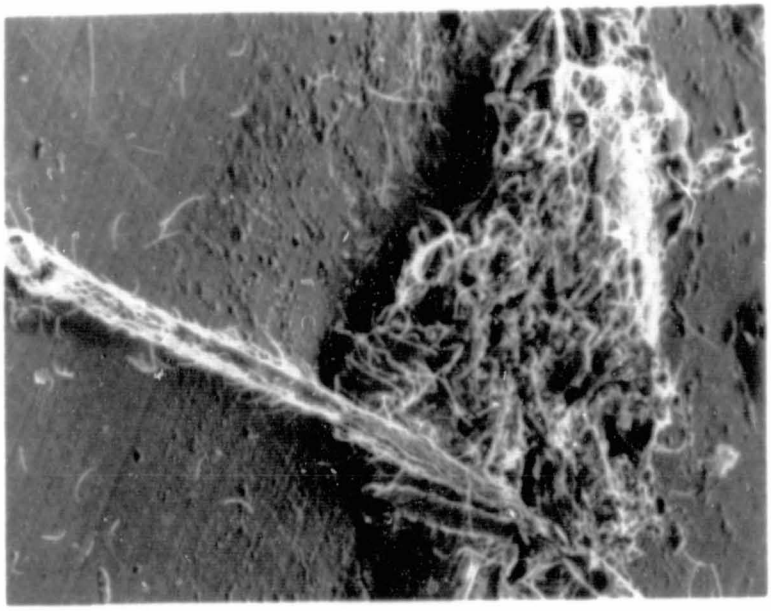

Nyebar 120x

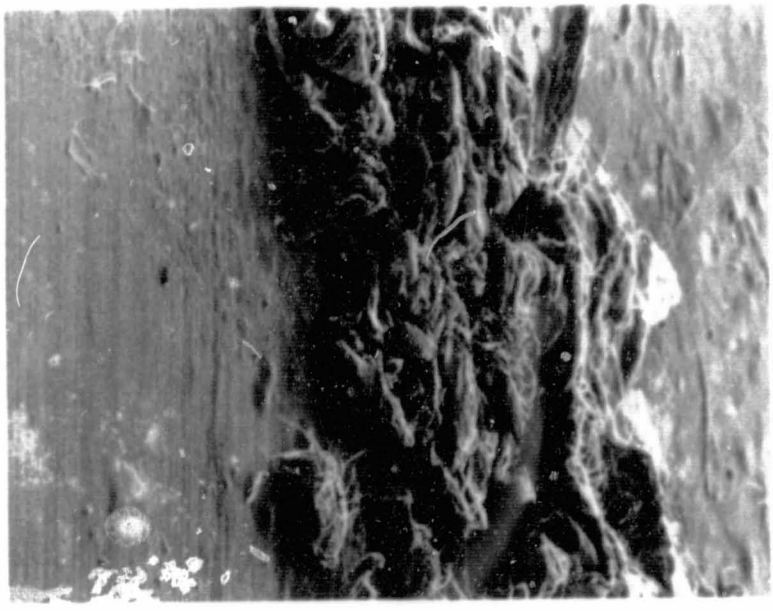

Polysulfone 120x

Figure 44: SEM photomicrographs of bug excrescence on Nyebar and Polysulfone

ORIGINAL PAGE IS
OF POOR QUALITY

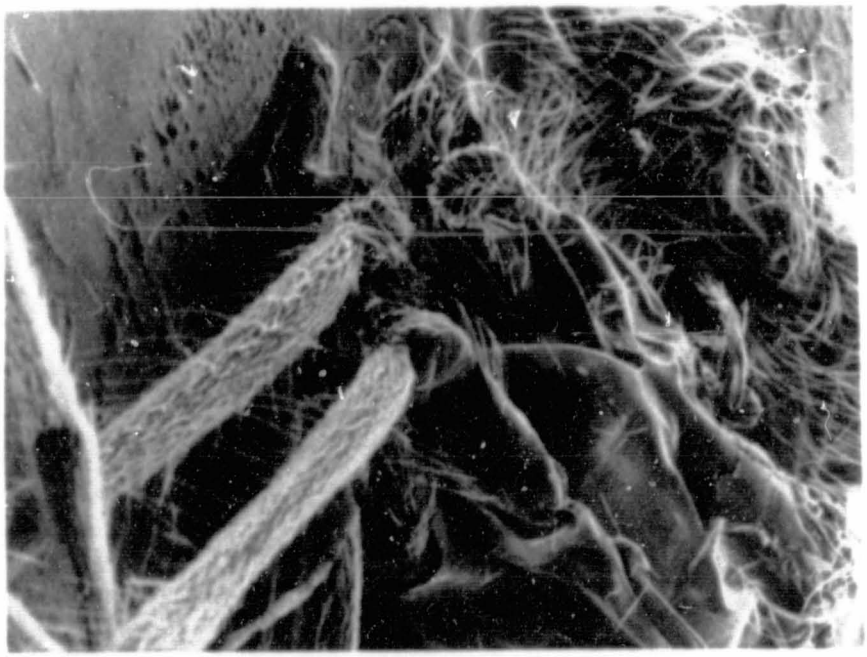

100x

Figure 45: SEM photomicrograph of bug fluid adhesive

ORIGINAL PAGE IS
OF POOR QUALITY

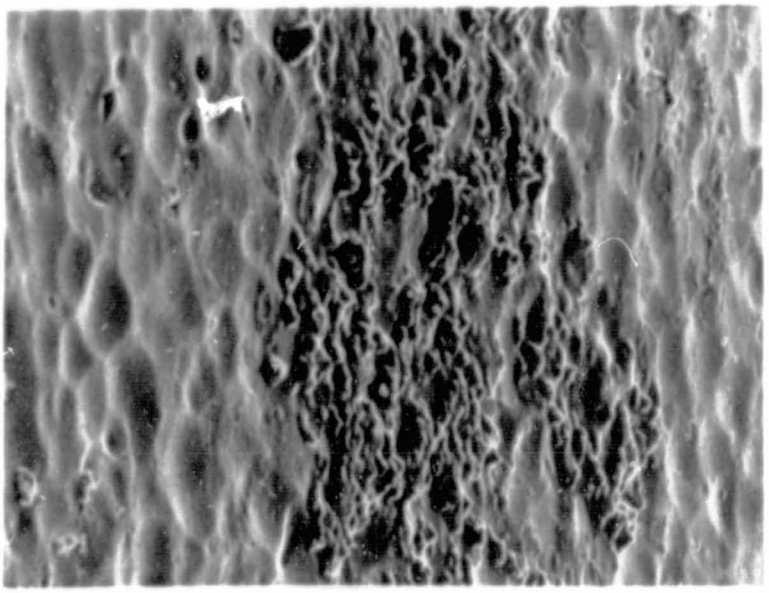

Nyebar 200x

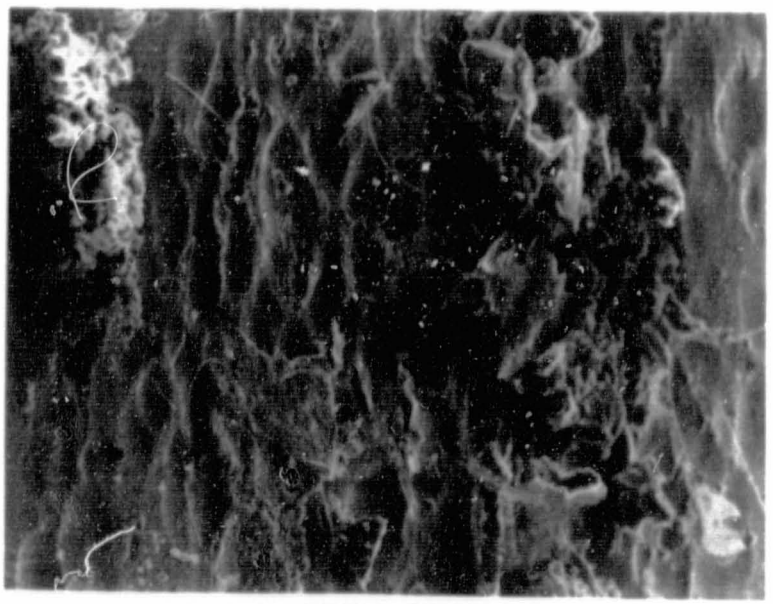

PMMA 200x

Figure 46: SEM photomicrographs of insect residues on rough surfaces

TABLE 34

Phase I Bug Counts

Sample	Bug Parts	Bug Splats	Total
Nyebar	30	21	51
Nyebar Control	78	18	96
PSF	91	22	113
PSF Control	73	81	154

were also calculated and the results are shown in Table 35. Comparing total densities, it can be noted that PSF has 67% the density of its control. On the other hand, Nyebar has only about 50% of the density of its control. This shows that Nyebar with its low surface energy is more effective in minimizing insect sticking.

4.5.1.2 Phase II

Bug counts are shown in Table 36. The results are plotted versus surface energy and surface roughness in Figures 47 and 48 respectively. A slight upward trend is noted in Figure 47 with increasing surface energy. It can be noted in Figure 48 that Nyebar and teflon appear to have lower bug counts than the high energy surfaces. However, the trend is erased by the large error bars.

4.5.2 Area Moment Results

An example of a display of area moments is shown in Figure 49. The graph shows a plot of the number of bugs of a certain size that were located at a certain distance away from the stagnation line. The bigger a bug is and the farther it is from the stagnation line (upper right hand corner of plot), the more likely it is to disrupt laminar flow on the aircraft wing.

TABLE 35

Phase I Bug Densities

Sample	Bug Parts	Bug Splats	Total
Nyebar	0.18	0.12	0.30
Nyebar Control	0.46	0.11	0.57
PSF	0.54	0.13	0.69
PSF Control	0.43	0.48	0.91

Densities in number/cm^2

TABLE 36

Phase II Bug Counts

Sample	Bug Counts
Nyebar - 0.2	11.3 ± 4.8
Nyebar - 0.5	10.7 ± 4.5
Nyebar - 0.9	14.0 ± 5.9
Nyebar - 1.3	10.4 ± 6.0
Teflon - 0.2	12.9 ± 6.3
Teflon - 0.5	12.2 ± 7.6
Teflon - 0.9	10.5 ± 4.8
Teflon - 1.3	9.2 ± 6.5
PSF - 0.2	15.2 ± 5.8
PSF - 0.5	13.7 ± 5.8
PSF - 0.9	16.2 ± 7.9
PSF - 1.3	14.1 ± 7.4
PMMA - 0.2	17.0 ± 7.3
PMMA - 0.5	17.9 ± 8.7
PMMA - 0.9	15.5 ± 7.5
PMMA - 1.3	15.3 ± 6.0
Control - 0.2	15.2 ± 10.0
Control - 0.5	15.8 ± 6.8
Control - 0.9	16.2 ± 7.2
Control - 1.3	18.4 ± 12.7

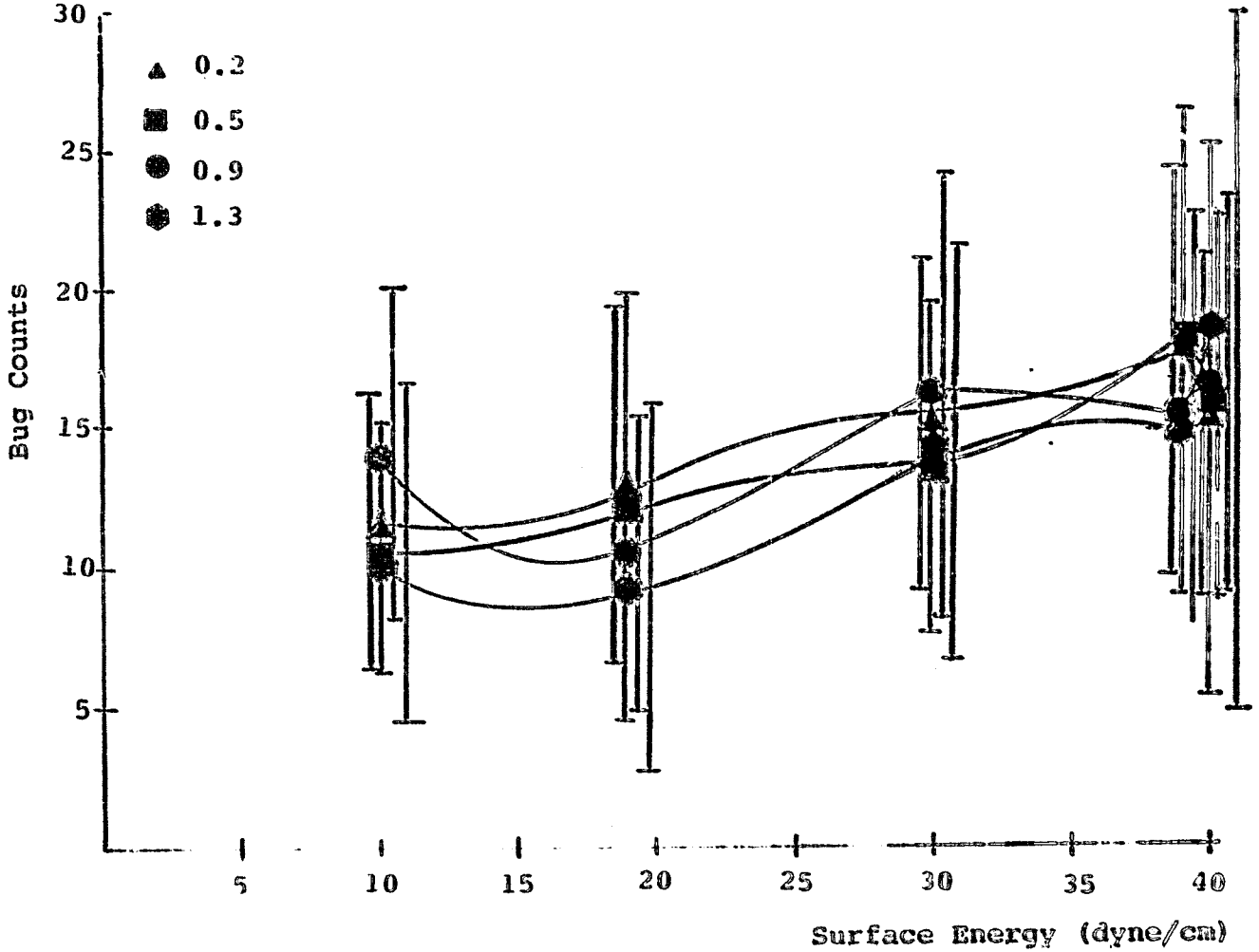

Figure 47: Phase II bug count versus surface energy.

ORIGINAL PAGE IS
OF POOR QUALITY

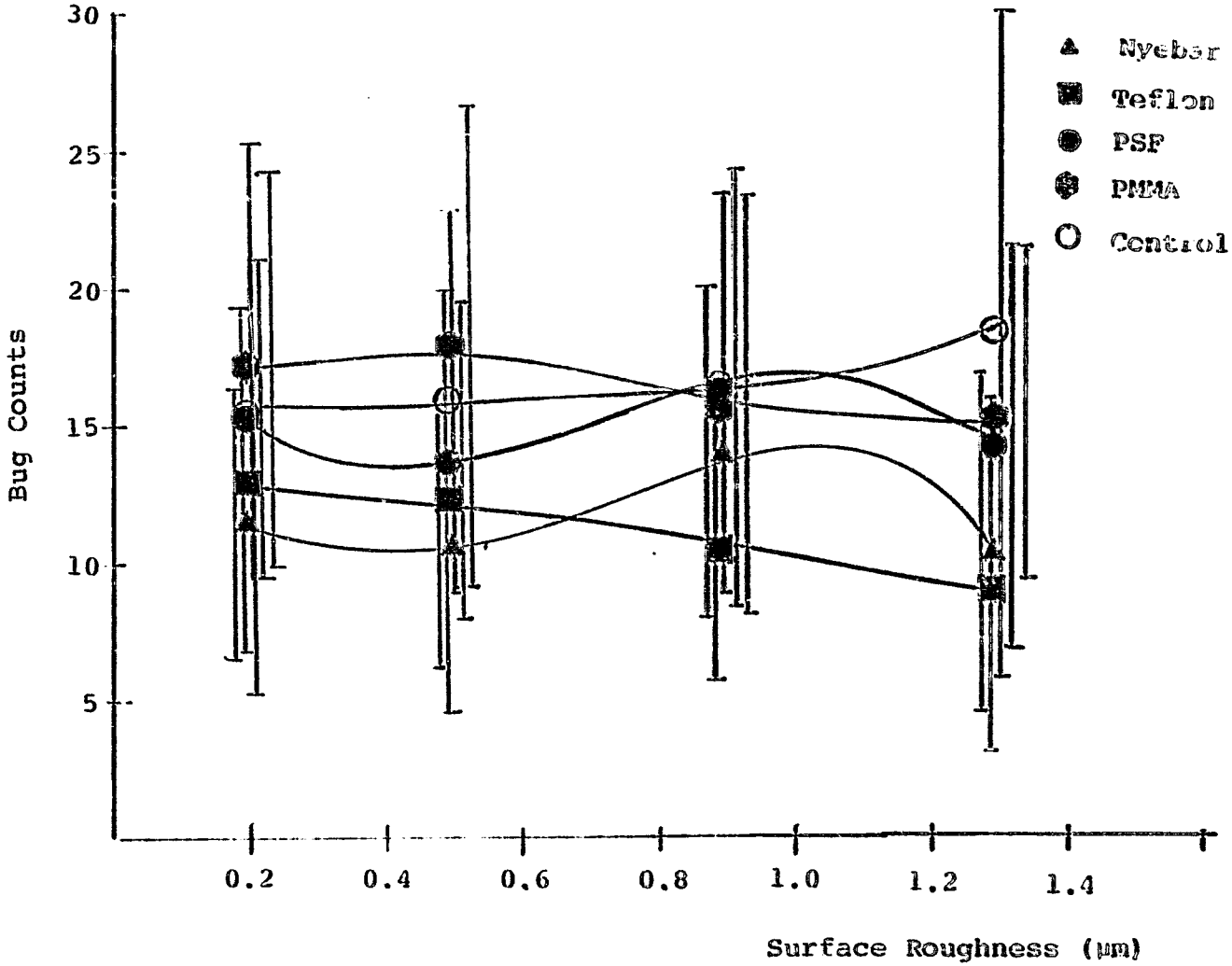

Figure 48: Phase II bug count versus surface roughness.

ORIGINAL PAGE IS
OF POOR QUALITY

Figure 49: Area moment display.

ORIGINAL PAGE IS
OF POOR QUALITY

Area moments are plotted versus surface energy in Figure 50. The smoothest samples tend to have the highest moment and the roughest samples have the lowest moments. This is contrary to what was expected. One would assume that on a smooth surface the residues would slide off, thus resulting in a lower moment. The rougher surface may cause the formation of air pockets upon impact with the bug, which does not allow total adhesion and results in easier removal. Except for the 0.2μm R_a roughness, Nyebar and teflon have lower moments.

Area moments are plotted against surface roughness in Figure 51. It can be noted that for the intermediate roughnesses, teflon has the lowest area moment. However, this may be due to elasticity of the thicker film rather than the surface energy. The moments for 0.5μm to 1.3 μm R_a are almost identical, reflecting the similarity in roughnesses shown in results previously given in Table 4. Again, the same trends in this plot are also erased by the large error bars.

4.5.3 Height Moments Results

Height moments are plotted against surface energy in Figure 52. The same trends are seen here as those seen in the area moment plot (see Figure 50). However, since

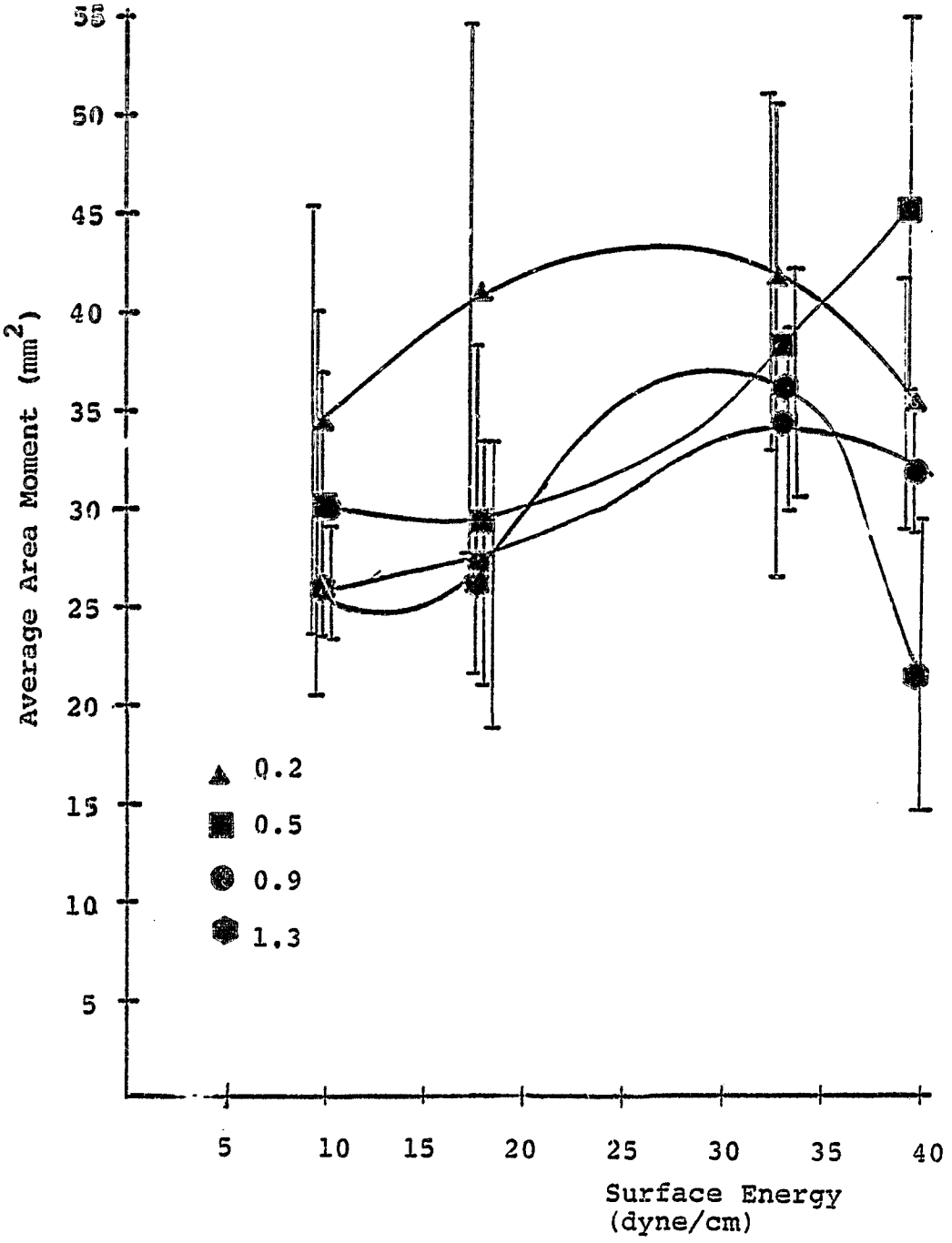

Figure 50: Area moments versus surface energy.

ORIGINAL PAGE IS
OF POOR QUALITY

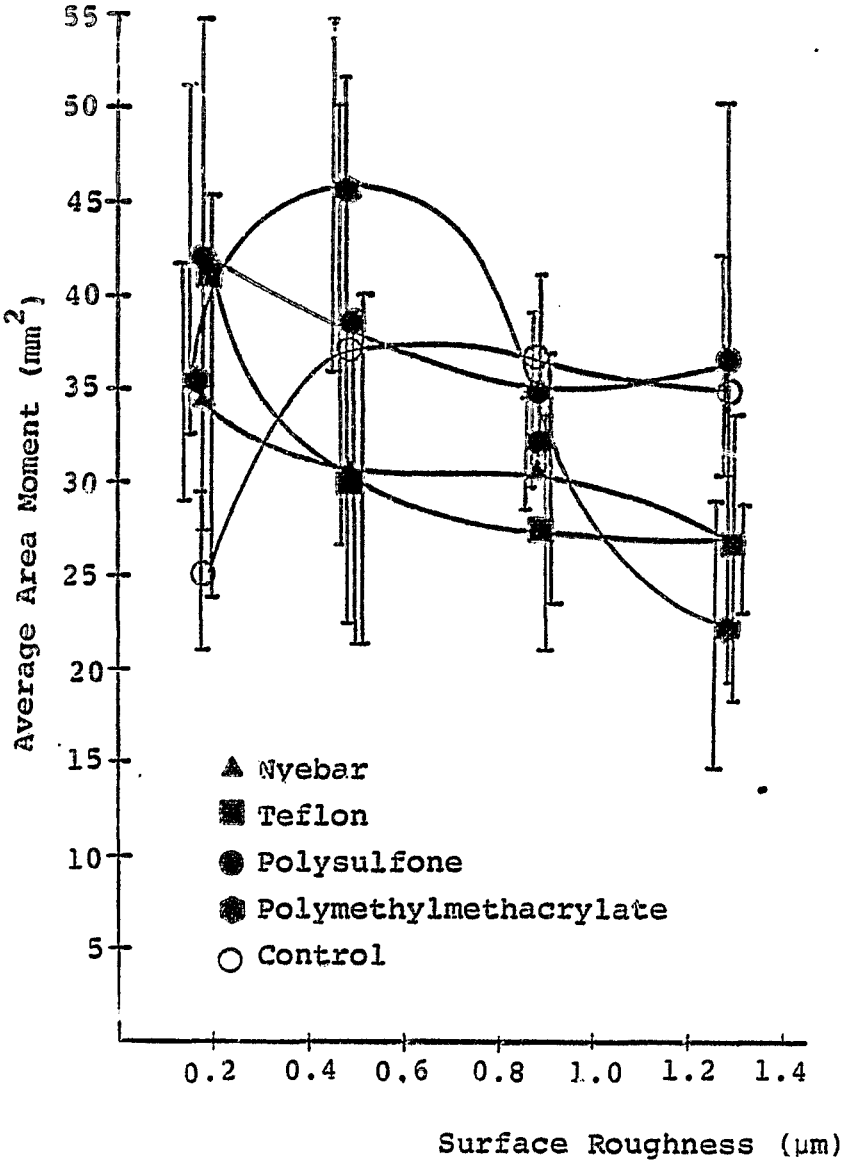

Figure 51: Area moments versus surface roughness.

ORIGINAL PAGE IS
OF POOR QUALITY

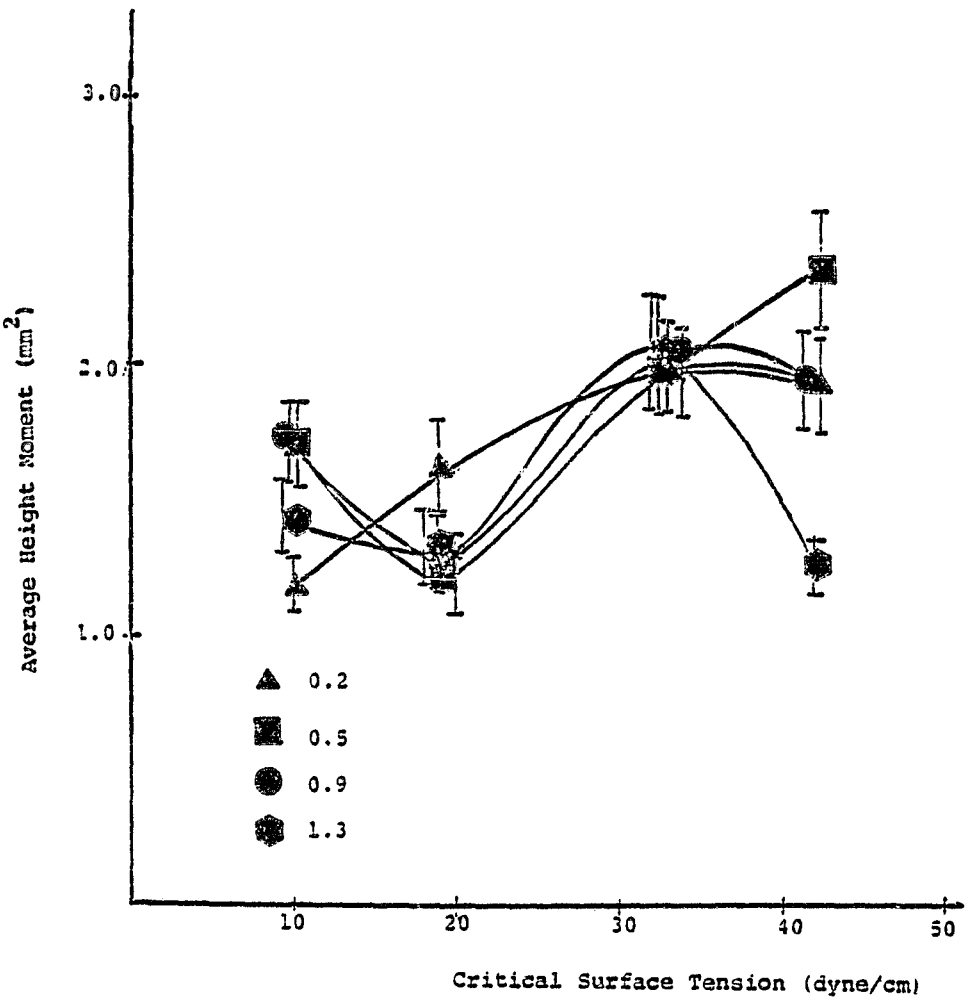

Figure 52: Height moment versus surface energy.

measurements were done with a microscope, twice the number of counts was obtained, giving better results statistically.

The height moments are plotted against surface roughness in Figure 53. The trends seen here are the same as those in the corresponding area moment plot (see Figure 51). It is interesting to note that results of control and Nyebar track each other in spite of the big difference in surface energy.

The results were pulled together by plotting height moments versus contact angle in Figure 54. It is shown that except for the anomalous behavior of aluminum, there is an upward trend of height moments with the increase of surface energy, as indicated by the decrease in water contact angles.

The randomization of sample mounting gave no bias in bug counts as a function of mount position. This is shown in Figure 55.

4.5.4 Bug Identity

Finally, bug identification results for Phases I and II are given in Tables 37 and 38 respectively. 95% of the residues identified belonged to the order Diptera -- the order of flies. Examples of these insects are given in Figure 56. These results agree with the findings of Freeman (13) in his study of insect abundance at low altitudes.

ORIGINAL PAGE IS
OF POOR QUALITY

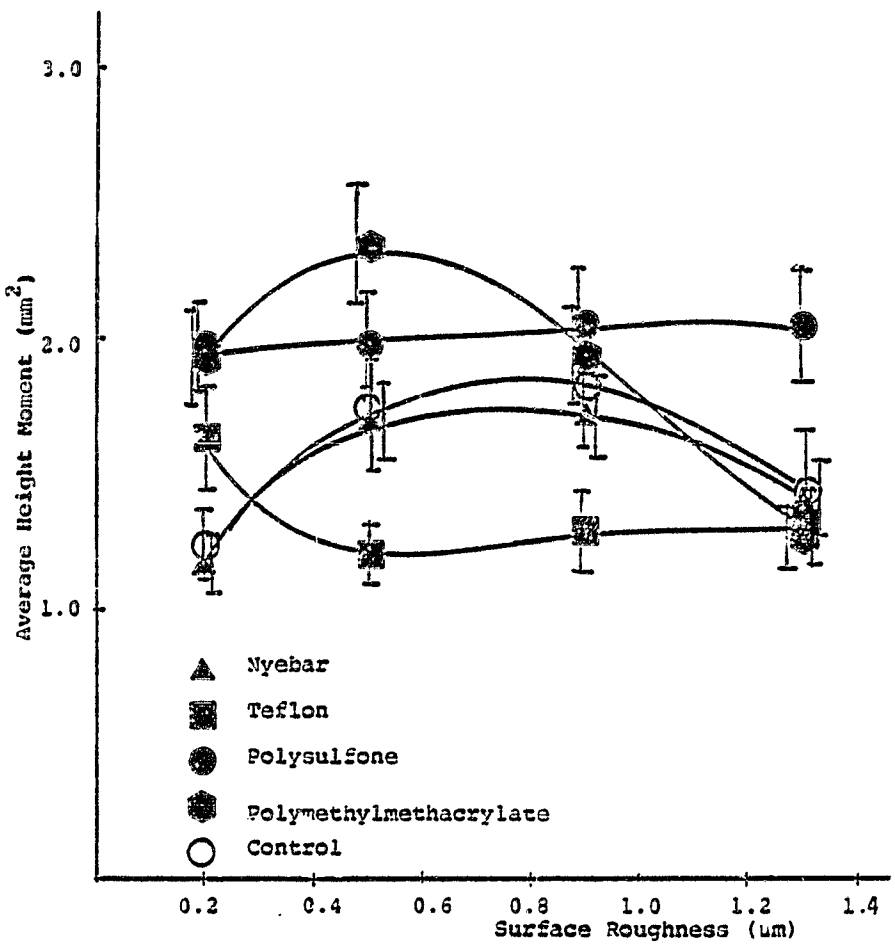

Figure 53: Height moment versus surface roughness.

ORIGINAL PAGE IS
OF POOR QUALITY

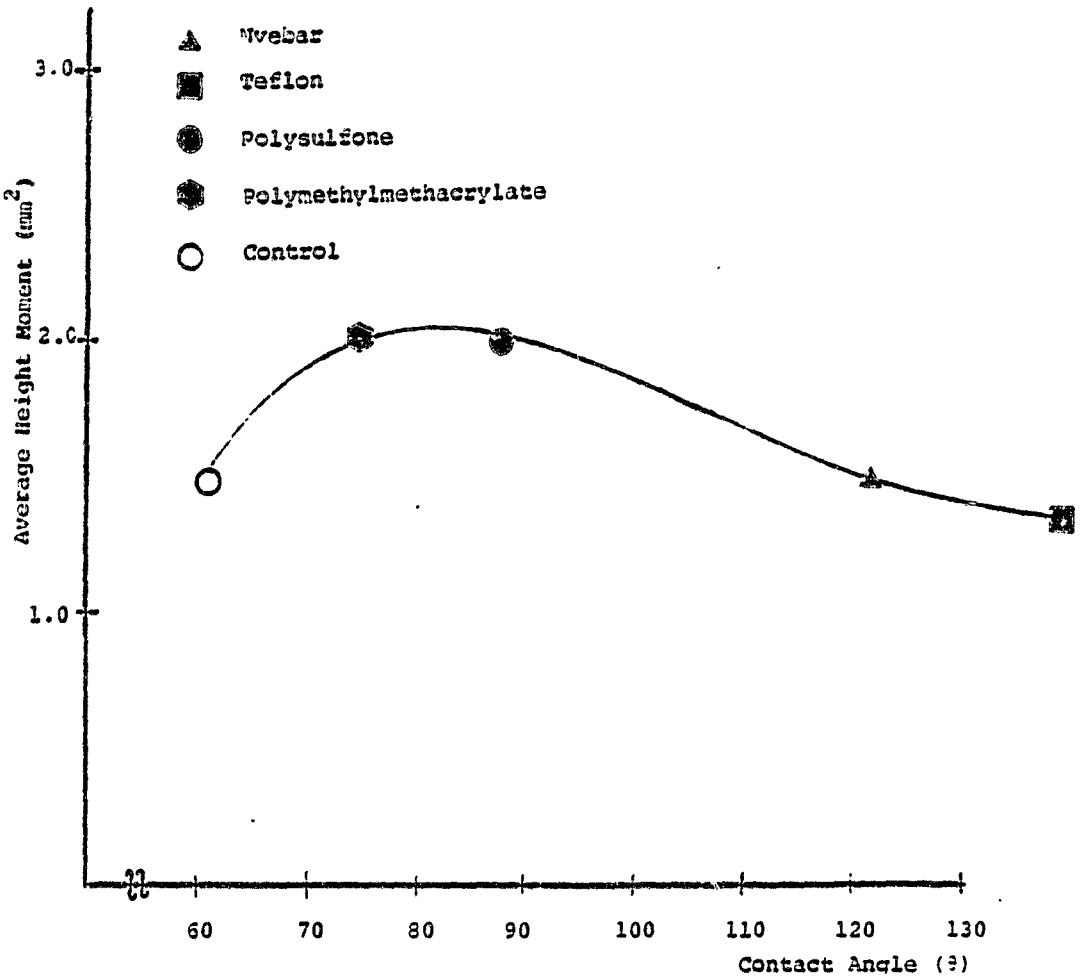

Figure 54: Height moment versus contact angle.

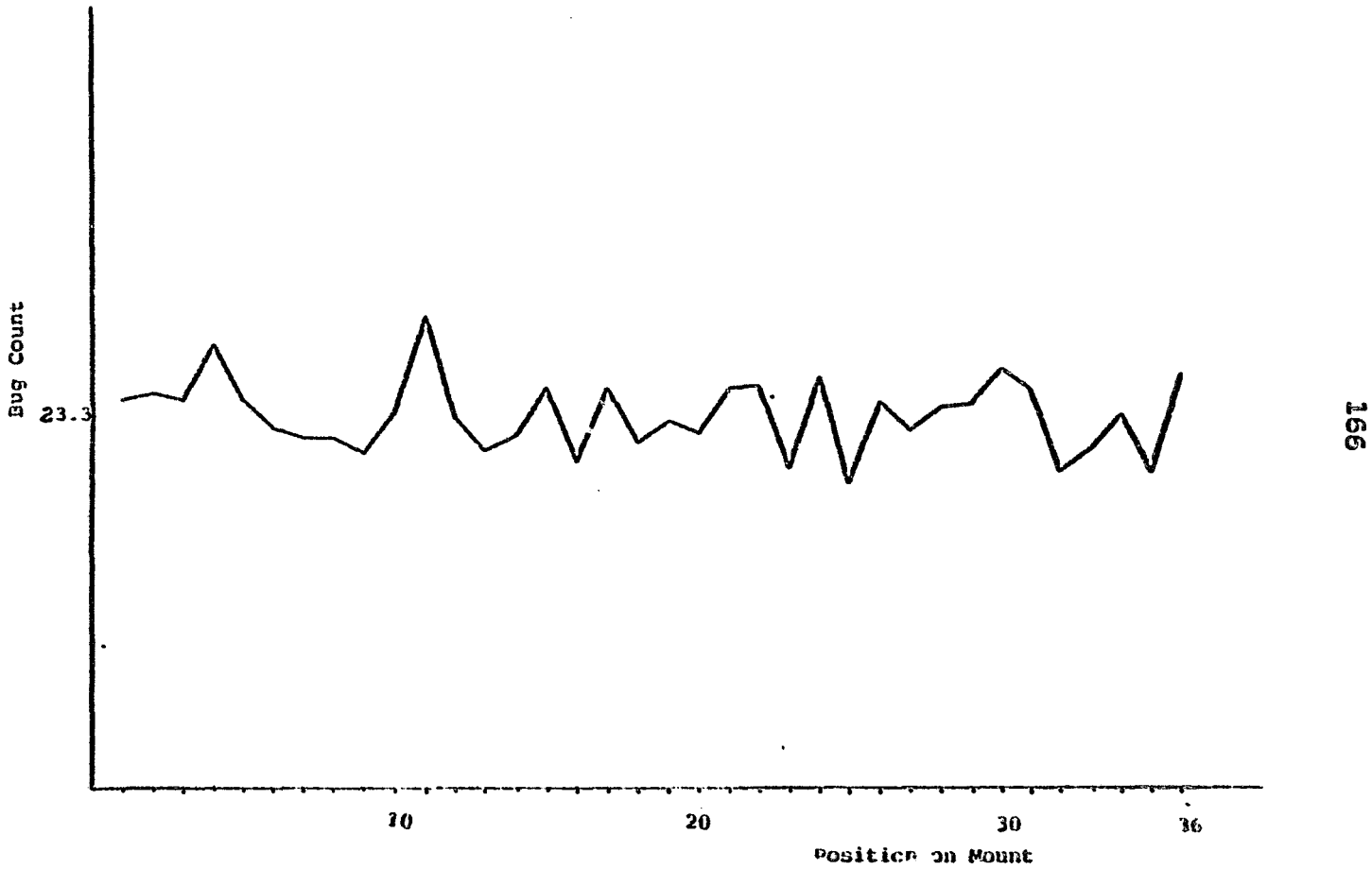

Figure 55: Bug count versus mount position.

TABLE 37

Phase I Bug Identity

Class Insecta

Order	Homoptera	Trichoptera	Diptera	Ephemeroptera
Sample				
Nyebar	Aphidae		Cecidomiidae	
			Culicoides	
			Chironomidae	
Nyebar Control			Cecidomiidae	
			Culicoides	
			Psychodidae	
			Mycetophilidae	
			Chironomidae	
PSF	Aleroidae		Cecidomiidae	
	Aphidae		Chironomidae	
			Culicoides	
			Chloropidae	

TABLE 37 CONTINUATION

	Order	Homoptera	Trichoptera	Diptera	Ephemeroptera
PSF	Control	Aphidae	Hydroptilidae	Maseidae	Heptageniidae
		Cicadellidae		Chironomidae	
				Cecidomiidae	
				Culicidae	
				Tipulidae	
				Chloropidae	

TABLE 38

Phase II Bug Identity

Class Insecta

Order Diptera

Sample	Family
Nyebar - 4B - 0.9	Chironomidae
Teflon - 5A - 0.9	Chironomidae
Teflon - 2B - 0.5	Chironomidae
	Culicidae
Teflon - 5A - 1.3	Chironomidae
	Psychodidae
PSF - 4B - 0.2	Chironomidae
PSF - 5B - 0.2	Chironomidae
	Culicidae
PSF - 5B - 0.9	Chironomidae
	Culicidae
PSF - 4A - 1.3	Chironomidae
PMMA - 5A - 0.5	Chironomidae
	Chilisidae
PMMA - 5B - 0.2	Chironomidae
PMMA - 5B - 0.5	Chironomidae
	Culicidae
PMMA - 4B - 0.9	Chironomidae
	Simuliidae

TABLE 38 CONTINUATION

Sample	Family
PMMA - 5B - 0.9	Chironomidae
	Tipulidae
Control - 4 - 0.5	Chironomidae
	Ctitidae

ORIGINAL PAGE IS
OF POOR QUALITY

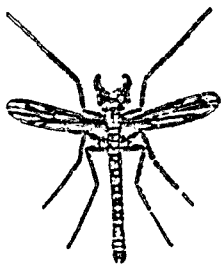

Chironomidae
(A midge)

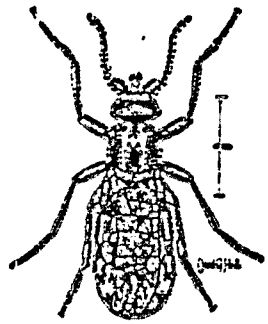

Culicoides
(The little gray punkie)

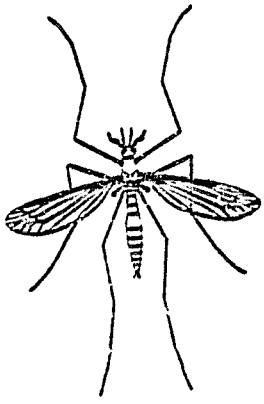

Tipulidae
(A crane fly)

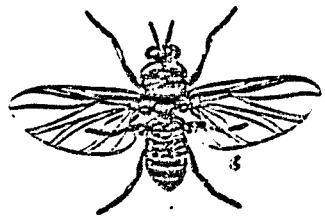

Simuliidae
(A black fly)

Figure 56: Examples of insects collected in insect impact experiments.

Chapter V

SUMMARY

This research was conducted to study the role of surface energy and surface roughness on the adhesion of insect residues to aircraft wings. The investigation was divided into two parts. First, an in-depth study on surface energy was conducted. Second, an attempt was made to correlate surface energy and surface roughness to insect fouling.

The critical surface tensions of four polymers were determined with two sets of liquids , specifically, aqueous ethanol solutions and the Zisman series. The Wilhelmy plate method was found to be suitable for surface tension measurements of both solutions and pure liquids, while the capillary rise method only gave accurate results for pure liquids. The critical surface tensions of the polymers Nyebar, teflon, polysulfone and polymethylmethacrylate were measured. For the low energy surfaces, Nyebar and teflon, the values of critical surface tension were independent of the liquid series used. However, the values of critical surface tension for the higher energy polymer films, polysulfone and polymethylmethacrylate, were shown to depend on the liquid series used. It was established that the critical surface tension corresponds to the dispersion

component of the solid surface energy. The non-dispersion component of the solid surface energy was determined by the Tamai, Makuuchi, Suzuki and the Owens and Wendt methods. The results do not match and demonstrates the need for further study to firmly establish the role of non-dispersion forces across the solid/liquid interface. The presence of high energy patches on the substrate surface was reflected by inconsistent receding contact angles.

The effect of surface energy and surface roughness on insect fouling was studied by collecting insect residues. Contact angle measurements, ESCA and specular reflectance FT-IR established that surface characteristics of the polymer films were not severely altered by exposure during the insect impact experiments. SEM photomicrographs were taken to investigate the topography of insect residues on the substrates. There was less spreading of insect excrescence on the low energy Nyebar surface than on the high energy polysulfone and polymethylmethacrylate surfaces. Through bug counts and moment calculation results, it was shown that surface energy affects insect adhesion while surface roughness had a minimal effect. For the sintered teflon films, results show that elasticity may play as important a role on the phenomenon of insect fouling as surface energy does.

REFERENCES

1. R. Cotta, Aviation, January, 12 (1980).

2. L. B. Gratzer and D. George-Falvy, D., CTOL Transport Technol., 409 (1978).

3. R. L. James and D. V. Maddalon, Aerospace America, 22, 54 (1984).

4. R. D. Wagner and M. C. Teschin, Aerospace America, 22, 72 (1984).

5. J. Tucker, High Technology, 4, 72 (1984).

6. B. H. Carmichael, NASA CR-152276, May 1979.

7. W. E. Gray and H. Davis, Aeronautical Research Council, London, 1952, paper 2485.

8. J. L. Maresh and M. B. Bragg, AIAA Second Appl. Aerodyn. Conf., Seattle, Washington, 1984.

9. W. S. Coleman, J. Aerospace Science, 26, 264 (1959).

10. D. J. Marsden, Canadian Aeronautics and Space Journal, 24, 83 (1978).

11. R. F. Sturgeon, NASA CR-159254, September, 1980.

12. J. B. Peterson and D. F. Fisher, NASA CP 2036, 1978.

13. J. A. Freeman, J. Am. Ecol., 14, 128 (1945).

14. W. S. Coleman, Aeronautical Quarterly, 11, 177 (1960).

15. D. J. Shaw, "Introduction to Colloid and Surface Chemistry," 3rd ed., Butterworths and Co., Ltd., Boston, 1980, 127.

16. F. J. Holly, in "Physicochemical Aspects of Polymer Surfaces," vol. 1, K. L. Mittal, Ed., Plenum Press, N.Y., 1983, 141.

17. A. W. Adamson, "Physical Chemistry of Surfaces," 4th ed., John Wiley and Sons, Inc., N.Y., 1982.

18. B. O. Bateup, Int. J. Adhesion and Adhesives, July, 233 (1981).

19. W. A. Zisman, in "Adv. Chem. Ser. 43," ACS, Washington, D. C., 1964, 1.

20. R. E. Johnson and R. H. Dettre, Surface and Colloid Sci., vol. 2, E. Matijevic, Ed.,John Wiley and Sons, Inc., N.Y., 1969.

21. B. J. S. Pirie and D. W. Gregory, J. Chem. Ed., 50, 682 (1973).

22. T. Young, Phil. Trans. Roy. Soc. (London), 95, 65 (1805).

23. W. D. Harkins, "The Physical Chemistry of Films," Reinhold Publishing Corp., N.Y., 1952.

24. A. W. Neumann, Adv. in Coll. and Interface Science, 4, 105 (1974).

25. A. W. Adamson and I. Ling, in "Adv. Chem. Ser. 43," ACS, Washington, D.C., 1964, 57.

26. N. K. Adam, in "Adv. Chem. Ser. 43," ACS, Washington, D.C., 1964, 32.

27. J. R. Huntsberger, in "Treatise on Adhesion and Adhesives," vol. 5, R. L. Patrick, Ed., Marcel Dekker, Inc., N.Y., 1981, 1.

28. J. C. Melrose, in "Adv. Chem. Ser. 43," ACS, Washington, D.C., 1964, 158.

29. P. Hu and A. W. Adamson, J. Coll. Interface Sci., 59, 605 (1977).

30. R. J. Good, J. Coll. Interface Sci., 52, 308 (1975).

31. E. G. Shafrin and W. A. Zisman, in "Adv. Chem. Ser. 43," ACS, Washington, D.C., 1964, 145.

32. E. G. Shafrin and W. A. Zisman, J. Phys. Chem., 64, 519 (1960).

33. B. W. Cherry, Polymer Surfaces, Cambridge Univ. Press, U.K., 1981.

34. R. J. Good, in "Adv. Chem. Ser. 43," ACS, Washington, D. C., 1964, 74.

35. W. J. Murphy, M. W. Roberts and J. R. H. Ross, J. Chem. Soc., Fara. Trans. I, 68, 1190 (1972).

36. K. M. Byrne, J. R. H. Ross and M. W. Roberts, Adhesion 1, 19 (1977).

37. E. K. Legin, Koll. Zhur., 36, 370 (1974).

38. D. Hoernsmeyer, J. Phys. Chem., 70, 2628 (1966).

39. L. A. Girifalco and R. J. Good, J. Phys. Chem., 61, 904 (1957).

40. L. A. Girifalco and R. J. Good, J. Phys. Chem., 64, 561 (1960).

41. R. J. Good, Surf. Coll. Sci., 11, 1 (1979).

42. F. M. Fowkes, in "Adv. Chem. Ser. 43," ACS, Washington, DC, 1964, 99.

43. F. M. Fowkes, in "Surfaces and Interfaces I," J. J. Burke, N. L. Reed and V. Weiss, Eds., Syracuse Univ. Press, NY, 1967, 197.

44. F. M. Fowkes, in "Chem. Phys. of Interfaces," ACS, Washington DC, 1971, 154.

45. F. M. Fowkes, J. Adh., 4, 155 (1972).

46. F. M. Fowkes, in "Polym. Sci. Technol.," 12A, 43 (1980).

47. F. M. Fowkes, in "Chem. Phys. of Interfaces," ACS, Washington, DC, 1964, 1.

48. W. R. Good, J. Coll. Interface Sci., 44, 63 (1973).

49. S. K. Rhee, Mat. Sci. Eng., 11, 311 (1973).

50. Y. Tamai, K. Makuuchi and M. Suzuki, J. Phys. Chem., 71, 4176 (1967).

51. D. K. Owens and R. C. Wendt, J. Appl. Polym. Sci., 13, 1741 (1969).

52. S. Wu, in "Polym. Sci. Technol," 12A, 53 (1980).

53. S. Wu, J. Macromol. Sci., Revs. Macromol. Chem., C10, 174 (1974).

54. J. R. Dann, J. Coll. Interface Sci., 32, 302 (1970).

55. J. R. Dann, J. Coll. Interface Sci., 32, 321 (1970).

56. R. H. Dettre and R. E. Johnson, in "Adv. Chem. Ser. 43," ACS, Washington, DC, 1964, 136.

57. R. H. Dettre and R. E. Johnson, in "Adv. Chem. Ser. 43," ACS, Washington, DC, 1964, 112.

58. R. G. Cox, J. Fluid Mech., 131, 1 (1983).

59. A. Marmur, Adv. in Coll. Interface Sci., 19, 75 (1983).

60. M. H. Lee, Org. Coat. Appl., Polym. Sci. Proc., 48, 12 (1983).

61. D. M. Hercules and S. H. Hercules, J. Chem. Ed., 61, 402 (1984).

62. A. F. Orchard, in "Handbook of X-ray and Ultraviolet Photoelectron Spectroscopy," D. Briggs, Ed., Heyden and Son Ltd, London, 1977, 1.

63. C. S. Fadley, in "Electron Spectroscopy: Theory, Technique and Applications," vol. 1, C. R. Brundle and A. D. Baker, Eds., Academic Press, NY, 1978, 1.

64. M. W. Roberts, Chem. Br., 77, 510 (1981).

65. D. T. Clark, in "Polym. Sci. Technol.," vol. 5A, L. H. Lee, Ed., Plenum Press, NY, 1974, 241.

66. A. Barrie, in "Handbook of X-ray and Ultraviolet Photoelectron Spectroscopy," D. Briggs, Ed., Heyden and Son Ltd, London, 1977, 79.

67. J. C. Riviere, in "Practical Surface Analysis," D. Briggs and M. P. Seah, Eds., Wiley, 1983, 17.

68. D. T. Clark, in "Characterization of Metal and Polymer Surfaces," L. H. Lee, Ed., Academic Press, NY, 1977, 5.

69. D. T. Clark, in "Handbook of X-ray and Ultraviolet Photoelectron Spectroscopy," D. Briggs, Ed., Heyden and Son Ltd., London, 1977, 211.

70. D. Briggs, in "Practical Surface Analysis," D. Briggs and M. P. Seah, Eds., Wiley, 1983, 359.

71. A. Dilks, in "ACS Symposium Ser. 162," 1981, 293.

72. M. J. Higatsberger, in "Adv. in Electron. and Electron Physics," 56, 291 (1981).

73. D. Briggs, in "Handbook of X-ray and Ultraviolet Photoelectron Spectroscopy," D. Briggs, Ed., Heyden and Sons, Ltd., London, 1977, 153.

74. M. Vulli, SIA, 3, 67 (1981).

75. M. P. Seah, SIA, 2, 222 (1980).

76. M. P. Seah, in "Practical Surface Analysis," D. Briggs and M. P. Seah, Eds., Wiley, 1983, 181.

77. C. D. Wagner, J. Elec. Spec. Rela. Pheno., 32, 99 (1983).

78. K. Yabe and T. Yamashina, Applic. Surf. Sci., 8, 387 (1981).

79. I. Adler, L. I. Yin, T. Tsang and G. Coyle, J. Chem. Ed., 61, 757 (1984).

80. M. M. Bhasin, Chem. Eng. Prog., 3, 60 (1981).

81. I. D. Ward and M. Strathman, Ind. Res. Dev., 25, 154 (1983).

82. M. M. Millard, in "ACS Symposium Ser. 199," L. A. Casper and C. J. Powell, Eds., 1982, 143.

83. H. F. Webster, unpublished results.

84. C. B. Duke, J. Vac. Sci. Techn. A, 2, 139 (1984).

85. J. Cazaux, Applic. Surf. Sci., 10, 124 (1982).

86. J. T. Grant, J. Vac. Sci. Techn. A, 2, 1135 (1984).

87. D. Briggs, Applic. Surf. Sci., 6, 188 (1980).

88. S. P. Clough, J. Met., 33, 12 (1981).

89. A. Dilks, Anal. Chem., 53, 802A (1981).

90. D. T. Clark, Pure Appl. Chem., 54, 415 (1982).

91. D. R. Lloyd, L. E. Gerlowski, C. D. Sunderland, J. P. Wightman, J. E. McGrath, M. Igbal and Y. Kang, in "ACS Symposium Ser. 153," A. F. Turbak, Ed., 1981, 327.

92. D. W. Dwight, J. E. McGrath and J. P. Wightman, J. Appl. Polym. Sci: Appl. Polym. Symp. 34," Wiley, 1978, 35.

93. N. H. Turner and R. J. Colton, Anal. Chem., 54, 415 (1982).

94. J. L. Koenig, Adv. Polym. Sci., 54, 87 (1984).

95. A. T. Bell, in "ACS Symposium Ser. 137," M. L. Hair and A. T. Bell, Eds., 1980, chap. 2.

96. B. M. Fanconi, J. Test Eval., 12, 33 (1984).

97. P. Connes, Infrared Phys., 24, 69 (1984).

98. P. Jacquinot, Infrared Phys., 24, 99 (1984).

99. J. Strong, Infrared Phys., 24, 103 (1984).

100. H. A. Gebbie, Infrared Phys., 24, 105 (1984).

101. H. W. Siesler, J. Mol. Struct., 59, 15 (1980).

102. A. Ishitani, Polym. Prepr., 25, 186 (1984).

103. L. H. Lee, in "Characterization of Metal and Polymer Surfaces," vol. 2, L. H. Lee, Ed., Academic Press, NY, 1977, 147.

104. D. L. Allara, in "ACS Symp. Ser. 199," L. A. Casper and C. J. Powell, Eds., 1982, 33.

105. S. K. Husain, J. B. Hasted, D. Rosen, E. Nicol and J. R. Birch, Infrared Phys., 24, 201 (1984).

106. A. Ishitani, H. Ishida, F. Soeda and Y. Nagasawa, Anal. Chem., 54, 682 (1982).

107. N. J. Harrick, "Internal Reflection Spectroscopy," Wiley, 1967.

108. D. L. Allara, in "Characterization of Metal and Polymer Surfaces," vol 2, L. H. Lee, Ed., Academic Press, NY, 1977, 193.

109. E. P. Lavin, "Specular Reflectance, Mono. on Applied Optics no. 2," Adam Hilger Ltd., London, 1971.

110. N. J. Harrick, in "Characterization of Metal and Polymer Surfaces," vol 2, L. H. Lee, Ed., Academic Press, NY, 1977, 153.

111. R. T. Graf, J. L. Koenig and H. Ishida, Polym. Prepr., 25, 188 (1984).

112. F. J. Boerio, C. A. Gosselin, R. G. Dillingham and H. W. Liu, J. Adh., 13, 159 (1982).

113. W. G. Golden, Polym. Prepr., 25, 158 (1984).

114. R. T. Graf, J. L. Koenig and H. Ishida, Polym. Prepr., 25, 159 (1984).

115. F. J. Boerio and S. L. Chen, Applied Spectroscopy, 33, 121 (1979).

116. D. L. Allara, in "ACS Symp. Ser. 137," M. L. Hair and A. T. Bell, Eds., 1980, chap. 3.

117. M. Ito and W. Suitaka, Surf. Sci., 62, 308 (1977).

118. J. Gun, R. Isconici and J. Sagiv, J. Coll. Interface Sci., 101, 201 (1984).

119. C. Depecker, B. Sombert, P. Legrand, G. Turell and P. Quintard, Infrared Phys., 24, 115 (1984).

120. F. Daniels, J. H. Matthews and J. W. Williams, "Experimental Physical Chemistry," McGraw-Hill, Inc., NY, 1941.

121. W. D. Harkins and T. F. Anderson, J. Am. Chem. Soc., 59, 2189 (1937).

122. E. J. Slowinski and W. L. Masterton, J. Phys. Chem., 65, 1067 (1961).

123. A. W. Neumann and R. J. Good, Surf. Coll. Sci., 11, 31 (1979).

124. R. J. Good and M. N. Koo, J. Coll. Interface Sci., 71, 283 (1979).

125. L. Penn and B. Miller, J. Coll. Interface Sci., 77, 574 (1980).

126. M. R. Spiegel, "Probability and Statistics," McGraw-Hill, 1975, 352.

127. M. J. Jaycock and G. D. Parfitt, "Chemistry of Interfaces," Ellis Horwood, Ltd., England, 1981.

128. J. J. Jasper, "The Surface Tension of Pure Liquids, J. Phys. Chem. Ref. Data," vol. 1, 1972, 841.

129. Nye Co. Manufacturer's literature, 1981.

130. J. Brandup and H. Immergut, Eds., "Polymer Handbook," 2nd ed., Wiley, NY, 1975.

131. J. R. Huntsberger, personal communication.

132. D. W. Dwight, in "Characterization of Metal and Polymer Surfaces," vol. 2, L. H. Lee, Ed., Academic Press, NY, 1977, 313.

133. R. E. Baier, J. Biomech. Eng., 104, 257 (1982).

134. R. E. Baier and A. E. Meyer, in "Physicochemical Aspects of Polymer Surfaces," vol. 2, K. L. Mittal, Ed., Plenum Publishing Corp., 1983, 895.

135. G. Socrates, "Infrared Characteristic Group Frequencies," Wiley, 1980.

136. Y. Kang, MS Thesis, Virginia Polytechnic Institute and State University, 1981.